Elismar Lösch

Hydra Supercluster of Galaxies: Photometric Investigation and Galaxy-Cluster Memberships

São Paulo
2024

ELISMAR LÖSCH

Hydra Supercluster of Galaxies: Photometric Investigation and Galaxy-Cluster Memberships

Versão original

Dissertação apresentada ao Instituto de Astronomia, Geofísica e Ciências Atmosféricas da Universidade de São Paulo como requisito parcial para a obtenção do título de Mestre em Ciências.

Área de concentração: Astronomia extragalática.

Orientador: Prof. Dr. Laerte Sodré Junior

São Paulo
2024

The world does not need more "successfull" people. The Planet desperately needs more peacemakers, healers, restorers, storytellers & lovers of all kinds

Agradecimentos

Ter em mãos minha dissertação de mestrado é bastante satisfatório, e marca para mim mais uma importante conquista na minha formação como cientista. O Elismar de 14 anos, que se interessou por astronomia e física lendo os livros do Carl Sagan e Marcelo Gleiser emprestados pela professora de Filosofia no ensino médio (muito obrigado professora Angela!), e que morava com os pais no interior de uma cidadezinha no oeste de Santa Catarina chamada Maravilha, com certeza ficaria muito orgulhoso em saber que agora, cerca de 10 anos depois, ele está em vias de receber o título de Mestre em Astronomia pela maior universidade da América Latina. Não só esse Elismar de 10 anos atrás estaria orgulhoso, como o Elismar de hoje também está.

É um dever meu começar agradecendo aos meus pais, Valdir e Salete, que mesmo sem entender muito o que seria essa tal de Astronomia ou essa tal de Física, me deram muito apoio desde o ensino médio, quando eu dizia que queria seguir essa carreira e que teria que morar em outra cidade para ter acesso à uma Universidade que ofertasse o curso de Física. Eles também me apoiaram ao longo de todo o curso na UFSC, quando eu morei sozinho em Florianópolis entre 2017 e o começo da pandemia, em 2020. Além do apoio financeiro, também fizeram o papel de pais quando em nenhum momento me desanimaram, nunca falaram para abandonar o curso, ou para fazer alguma coisa diferente. Ao invés disso, contavam com orgulho para os parentes e outras pessoas que o filho deles estudava na federal, e que estudava "os planetas e as estrelas".

Também agradeço minhas irmãs, Silmara e Clecimara, por todos os "puxões de orelha" e conselhos desde o início da graduação. Mesmo à distância, elas foram presentes de diferentes formas em vários momentos. E aproveitando, vai um abracinho do tio Elismar para as fofurinhas dos meus sobrinhos Heloá e Theo.

O período da graduação, embora bastante duro em vários aspectos, foi também de muito crescimento em termos acadêmicos e pessoais de forma que é impossível expressar em um parágrafo. Gostaria de agradecer a todos que me apoiaram de alguma forma durante minha formação como físico. Começo pelos meus parceiros do Observatório da UFSC: Vitor, Gustavo, Daniel, Rodrigo, André e Juliana. Também sou grato aos professores do Grupo de Astrofísica da UFSC, em especial meu orientador de IC, o Daniel Ruschel Dutra, que me ensinou muito Python, astronomia e sobre a vida acadêmica. Vai um obrigado também aos meus roomates em Floripa pelos bons momentos no apê: Moisés, Julio, Matheus, Arthur, Yonier, Daniel, Germano, Lorena e Gabriel. Aos colegas, professores e outras pessoas que deixaram uma marca positiva na minha vida naqueles três anos e meio em Floripa, obrigado!

O início do mestrado e a minha vinda para São Paulo marcaram o início de uma renovação na minha vida, especialmente por terem acontecido após dois anos de pandemia que forçaram todo mundo a se distanciar fisicamente. Eu sou muito grato a todos amigos que fiz na pós nesses últimos dois anos e pelo que passamos juntos: Erik, Pedro (carioca), Pablito, Gê, Doug, Thayse, Bel, Lia, Lory, Pedro (mineiro), Limba, André, Vitor, Marcelo, Fê, Mirian, Raquel, Cata, Laís, Henrique, Giovani, Stelinha, Lili, Giulya, Leo, Ingrid, Giovani, Natalia, Lua, Gabriela, Anne. Além dos já citados, vai um abraço também pro pessoal do grupo do Laerte (Lucas, Carlos, Laura e Pierre), do Atendimento Astronômico (Rosely, Reinaldo e aos demais colegas), ao time

do basquete, meus atuais roommates, e todos que contribuíram para esses dois anos incríveis aqui em São Paulo (e lá vem mais quatro pela frente!!).

Um grande obrigado vai também à pessoa que com certeza mais contribuiu de forma direta para o meu mestrado, o Laerte. Agradeço por ser um excelente orientador, que está quase sempre disponível para conversar, responder e-mails e dar ideias pro andamento do trabalho. Aproveito também para deixar os agradecimentos para todos meus colaboradores, professores, e colegas de trabalho, que de alguma forma contribuíram para essa pesquisa e minha formação durante o mestrado: colaboração do S-PLUS (Cláudia, Erik, Lili, Vitor, Gustavo, Felipe, Fabio, Liana, Natanael, Gabriele, Angela, entre tantos outros), colaboração do CHANCES (Yara, Chris, Círia, Hugo, Gabriel Teixeira, Analia, Rodrigo Haack, Juan Pablo, Amrutha, Antonela, Ulrike, etc. etc.), professores das disciplinas (Beatriz Barbuy, Jorge Melendez, Walter Maciel e Gastão Lima Neto), e ao meu relator e muito possivelmente membro da minha banca, Eduardo Cypriano. Obrigado também aos feras da informática do IAG, que me salvaram algumas vezes (Marco e Luis), ao pessoal da secretaria da astronomia, ao pessoal da sessão da pós, e com certeza às moças do café, porque sem elas essa pesquisa não teria existido.

Acknowledgements

Having my master's thesis in hand is quite satisfying, and marks for me another important achievement in my training as a scientist. 14-year-old Elismar, who became interested in astronomy and physics by reading books by Carl Sagan and Marcelo Gleiser lent by his Philosophy teacher in high school (thank you very much, teacher Angela!), and who lived with his parents in the interior of a small town in west of Santa Catarina called Maravilha, I would certainly be very proud to know that now, about 10 years later, he is on the way to receiving the title of Master in Astronomy from the largest university in Latin America. Not only would this Elismar from 10 years ago be proud, but today's Elismar is too.

It is my duty to start by thanking my parents, Valdir and Salete, who, even though they didn't really understand what this Astronomy or Physics thing would be, gave me a lot of support since high school, when I said I wanted to pursue this career and that I would have to live in another city to have access to a University that offered the Physics course. They also supported me throughout my course at UFSC, when I lived alone in Florianópolis between 2017 and the beginning of the pandemic, in 2020. In addition to financial support, they also played the role of parents when they never discouraged me, never told me abandon the course, or to do something different. Instead, they proudly told relatives and other people that their son studied at a federal university, and that he studied "the planets and the stars".

I also thank my sisters, Silmara and Clecimara, for all the "ear tugging" and advice since the beginning of my undergrad. Even from a distance, they were present in different ways in several moments. I send also a little hug to my cute nephews Heloá and Theo.

The undergraduate period, although quite difficult in many aspects, was also full of growth in academic and personal terms that is impossible to express in a paragraph. I would like to thank everyone who supported me in any way during my training as a physicist. I start with my partners at the UFSC Observatory: Vitor, Gustavo, Daniel, Rodrigo, André and Juliana. I am also grateful to the professors of the Astrophysics Group at UFSC, especially my undergrad research advisor, Daniel Ruschel Dutra, who taught me a lot about Python, astronomy and academic life. Thank you also to my roomates in Floripa for the good times in the apartment: Moisés, Julio, Matheus, Arthur, Yonier, Daniel, Germano, Lorena and Gabriel. To my colleagues, teachers and other people who left a positive mark on my life during those three and a half years in Floripa, thank you!

The beginning of my master's degree and my coming to São Paulo marked the beginning of a renewal in my life, especially since it happened after two years of pandemic that forced everyone to physically distance themselves. I am very grateful to all the friends I made during the masters these last two years and for what we went through together: Erik, Pedro (from Rio de Janeiro), Pablito, Gê, Doug, Thayse, Bel, Lia, Lory, Pedro (from Minas Gerais), Limba, André , Vitor, Marcelo, Fê, Mirian, Raquel, Cata, Laís, Henrique, Giovani, Stelinha, Lili, Giulya, Leo, Ingrid, Giovani, Natalia, Lua, Gabriela, Anne. In addition to those already mentioned, a big hug goes to the people from Laerte's group (Lucas, Carlos, Laura and Pierre), Atendimento Astronômico (Rosely, Reinaldo and other colleagues), the basketball team, my current roommates, and every-

one who contributed to these two incredible years here in São Paulo (and there are four more to come!!).

A big thank you also goes to the person who certainly contributed most directly to my master's degree, Laerte. Thank you for being an excellent advisor, who is almost always available to talk, answer emails and give ideas for the progress of the work. I would also like to take this opportunity to thank all my collaborators, teachers, and co-workers, who in some way contributed to this research and my training during my master's degree: S-PLUS Collaboration (Cláudia, Erik, Lili, Vitor, Gustavo, Felipe , Fabio, Liana, Natanael, Gabriele, Angela, among many others), CHANCES Collaboration (Yara, Chris, Círia, Hugo, Gabriel Teixeira, Analia, Rodrigo Haack, Juan Pablo, Amrutha, Antonela, Ulrike, etc. etc.), teachers (Beatriz Barbuy, Jorge Melendez, Walter Maciel and Gastão Lima Neto), and my rapporteur and very possibly member of my panel, Eduardo Cypriano. Thank you also to the IT experts at IAG, who saved me a few times (Marco and Luis), to the people at the astronomy secretariat, to the postgraduate session staff, and certainly to the coffee staff, because without them this research would not have existed.

Resumo

Em escalas de dezenas de Megaparsecs (Mpcs), a distribuição de matéria bariônica e matéria escura no Universo forma a chamada teia-cósmica. Aglomerados de galáxias servem como os nós dessa intrincada estrutura, e são conectados por cadeias filamentares de galáxias e grupos que coletivamente formam superaglomerados. Neste trabalho, realizamos uma investigação fotométrica do Superaglomerado de galáxias de Hydra, uma grande aglomeração de galáxias no Universo local ($z \sim 0.012$), composta primariamente pelo Aglomerado de Hydra (Abell 1060) e seus vizinhos, como o Aglomerado de Antlia (Abell S0636). Para isso, empregamos principalmente dados do quarto Data Release do Southern Photometric Local Universe Survey (S-PLUS DR4), caracterizado por um sistema fotométrico de 12 filtros que permite a determinação de redshifts fotométricos (photo-zs) de alta precisão.

Nosso objetivo primário é a determinação do pertencimento galáxia-aglomerado, que nos permite investigar as propriedades e evolução de galáxias nessas estruturas. Adicionalmente, essa informação auxilia na seleção de alvos para futuros surveys espectroscópicos como o CHANCES (CHilean Cluster galaxy Evolution Survey). Tipicamente, a determinação do pertencimento de galáxias em aglomerados e outras estruturas depende de redshifts espectroscópicos. No entanto, os custos de observações espectroscópicas extensivas e a inexistência de um survey compreensivo no hemisfério sul, comparável ao Sloan Digital Sky Survey (SDSS), restringiu essas observações apenas às galáxias mais brilhantes. Para lidar com essa limitação, nós utilizamos redshifts fotométricos para refinar a atribuição de membros em tais estruturas do hemisfério sul.

Nosso trabalho incorpora o desenvolvimento e implementação de dois métodos distintos de pertencimento galáxia-aglomerado. O primeiro método emprega uma técnica de sigma-clipping, tomando em consideração a incerteza típica nos photo-zs como função da magnitude das galáxias para identificar membros dos aglomerados. Este método está sendo aplicado para selecionar alvos para observação pelo survey CHANCES. O segundo método emprega uma técnica Bayesiana robusta para atribuir probabilidades de pertencimento para galáxias em aglomerados. Esta abordagem considera toda a função de densidade de probabilidade (PDF, na sigla em inglês) dos photo-zs das galáxias como entrada. Nós testamos este método com sucesso em mocks de aglomerados e o aplicamos em aglomerados na região do Superaglomerado de Hydra, produzindo valores típicos de pureza e completeza de aproximadamente 80%. Para o Aglomerado de Hydra, atingimos valores estimados de pureza e completeza de, respectivamente, 92% e 68% com um corte de 35% na probabilidade de pertencimento usando o segundo método.

Uma vez que estamos interessados em toda a região do Superaglomerado de Hydra, um resultado adicional do nosso trabalho inclui uma compilação de 121 grupos e aglomerados de galáxias coletados da literatura no volume do Superaglomerado, assim como uma busca por por fontes de raios-X do Primeiro Data Release do SRG/eROSITA All Sky Survey (eRASS1), que resultou em contrapartes na localização do Aglomerado de Hydra e Aglomerado de Antlia, e uma terceira fonte associada com a NGC 3091, uma galáxia elíptica na parte norte do Superaglomerado.

Palavras-chave: galáxias: aglomerados: individual (Abell 1060, Abell S0636), técnicas: fotometria, cosmologia: estrutura em larga escala do Universo

Abstract

At scales of dozens of Megaparsecs (Mpc), the distribution of baryonic and dark matter in the Universe forms the so-called cosmic web. Galaxy clusters serve as the nodes of this intricate structure, and are connected by filamentary chains of galaxies and groups that collectively form galaxy superclusters. In this work, we carried a photometric investigation of the Hydra Supercluster of galaxies, a large agglomeration of galaxies in the local Universe ($z \sim 0.012$) composed primarily by the Hydra Cluster (Abell 1060) and its neighbors, such as the Antlia Cluster (Abell S0636). For this, we employ mainly data from the Fourth Data Release of the Southern Photometric Local Universe Survey (S-PLUS DR4), characterized by a 12-filter photometric system that allows for the determination of high-precision photometric redshifts (photo-zs).

Our primary objective is to determine galaxy-cluster memberships, enabling us to investigate the properties and evolution of galaxies within these structures. Additionally, this information aids in the selection of targets for upcoming spectroscopic redshift surveys like CHANCES (CHileAN Cluster galaxy Evolution Survey). Typically, the determination of galaxy memberships in clusters and other structures relies on spectroscopic redshifts. However, the cost of extensive spectroscopic observations and the absence of a comprehensive survey in the southern hemisphere, comparable to the Sloan Digital Sky Survey (SDSS), has restricted these observations to only the brightest galaxies. To address this limitation, we utilize photometric redshifts to refine membership assignments in the southern hemisphere structures.

Our work incorporates the development and implementation of two distinct galaxy-cluster membership methods. The first method employs a sigma-clipping technique, taking into account the typical photo-z uncertainty as a function of galaxy magnitude to identify cluster members. This method has been applied to select targets for observation within the CHANCES Survey. The second method employs a robust Bayesian approach to assign membership probabilities to galaxies in clusters. This approach considers the complete probability density function (PDF) of galaxy photo-z as input. We have successfully tested this method on cluster mocks and applied it to clusters within the Hydra Supercluster region, yielding typical values of purity and completeness of approximately 80%. For the Hydra Cluster, we achieved estimated completeness and purity values of, respectively, 92% and 68% with a 35% membership probability threshold using the second method.

Since we are interested in the whole region of Hydra Supercluster, an additional result of our work includes a compilation of 121 groups and clusters of galaxies collected from the literature in the volume of the Supercluster, as well as a search for X-rays sources from the First Data Release of SRG/eROSITA All Sky Survey (eRASS1), that resulted in counterparts at the location of Hydra and Antlia clusters, and a third source associated with NGC 3091, an elliptical galaxy at the northern part of the Supercluster.

Keywords: galaxies: clusters: individual (Abell 1060, Abell S0636), techniques: photometric, cosmology: large-scale structure of universe

Contents

List of Figures

List of Tables

1 Introduction

It is known today that the distribution of baryonic and dark matter at scales of dozens to hundreds of Mpcs in the Universe forms the so called cosmic web. Galaxy clusters occupy its nodes and are connected to other nodes by vast filamentary chains of galaxies and groups of galaxies. Theses filaments are often located at the intersections of planar structures called walls, which surround the voids, i.e., extend regions almost devoid of galaxies. Such pattern has been shown both by dark matter only or hydrodynamic simulations (e.g. Springel et al., 2005; Vogelsberger et al., 2014b), and observations (e.g. Peacock et al., 2002; Cautun et al., 2014).

In this intricate cosmic web, the largest structures we can find in the Universe are galaxy superclusters. Superclusters have typical sizes in the range $\sim 30-100$ Mpc and typical masses of order $\sim 10^{15} M_{\odot}$ (Sankhyayan et al., 2023b). They are home to a few to dozens of galaxy clusters, and can impact the evolution of these clusters and of their galaxies in different manners. An interesting example of supercluster is the one where our Local Group of galaxies, and therefore we, are located in: the Laniakea Supercluster (Tully et al., 2014).

In this project we present a dedicated study of the Hydra Supercluster of galaxies, located in the region defined by $150^{\mathrm{o}} <$ R.A. $< 180^{\mathrm{o}}$ and $-48^{\mathrm{o}} <$ Dec. $< -15^{\mathrm{o}}$, and with redshifts in the interval $0.002 < z < 0.018$ (see chapter 5, specially section 5.1).

In this Introduction, we will go through the literature relevant to our work, putting it in context. We start with some topics on the theory of structure formation in the Universe (section 1.1), then moving on to observational astronomy in section 1.2, when we discuss astronomical surveys and the large scale distribution of galaxies. In section 1.3 we review the literature on galaxy superclusters, elaborating on their definition, characteristics, and how they are studied in astronomy and cosmology. In section 1.4 we then present our object of study, Hydra Supercluster, and its known member clusters and groups. Finally, in section 1.5 we describe the goals of our work.

1.1 | Structure Formation in the Universe

Before proceeding to a more direct description of superclusters and clusters as we know them today, it is interesting to explore briefly the theory behind the formation of large scale structures (LSS) in the Universe. In this way, we can guide further discussions about the nature of these objects. The discussion of this section is mostly based on Schneider (2006), Lima Neto (2022) and Mo et al. (2010).

The matter and energy content in the primordial Universe was extremely uniform. Modern theory suggests that very subtle perturbations in this primordial density field arose due to quantum effects, and were amplified by the rapid expansion of the Universe immediately after the Big Bang due to the so-called inflation. One of the best evidences we have of such scenario is the Cosmic Microwave Background (CMB), which presents an anisotropy of $\Delta T/T \sim 10^{-5}$, pointing to very small variations in the early Universe's temperature and density fields (Planck Collaboration et al., 2020a). Despite of that, today the Universe if filled with large scale structures such as clusters of galaxies, with the richer ones containing more than 200 times more mass than the critical density of the Universe (defined as $\rho_c = 3H(t)^2/8\pi G$, where H is the Hubble parameter) inside a radius of $\sim 1.5h^{-1}$ Mpc ($H_0 = 100h$ km s^{-1} Mpc^{-1}). Faced with these observations, it is natural to ask how such an evolution in the density perturbations of the Universe occurred.

Let us start with the expression of the density contrast

$$\delta(\vec{r}, t) \equiv \frac{\rho(\vec{r}, t) - \bar{\rho}(t)}{\bar{\rho}(t)} \tag{1.1}$$

where $\bar{\rho}(t)$ denotes the mean cosmic matter density in the Universe at time t. In regions with density fluctuations $\Delta\rho(\vec{r}, t) = \rho(\vec{r}, t) - \bar{\rho}(t) > 0$, so that $\delta > 0$, the gravitational field will be stronger than the cosmic average, resulting that overdense regions will expand more slowly than the average Hubble expansion. Due to the expansion, the density in these regions will decrease, but at a slower pace than the mean cosmic density $\bar{\rho}(t)$, making the density contrast δ higher. At a certain point, these regions will contract and virialize, a process that is responsible for the formation of structure like clusters of galaxies. In summary, it is all about relative densities. As the density contrast in already overdense regions becomes higher, an even stronger gravitational field will be produced, and so on. The same situation happens the other way around, with underdense ($\delta < 0$) regions having a weaker gravitational field than the cosmic average, making them expand faster than the Hubble expansion, so that they will become emptier, more underdense, forming the cosmic voids.

1.1.1 | Linear perturbation theory

For weak gravitational fields, specially considering density perturbations much smaller than the Hubble radius, we can neglect the effects of General Relativity and apply a Newtonian approach to describe the growth of density perturbations. Furthermore, we can treat matter in the Universe as being a pressure-free fluid (called "dust"), with density $\rho(\vec{r}, t)$ and velocity field $\vec{v}(\vec{r}, t)$. The behaviour of this fluid is described by the continuity equation

$$\frac{\partial \rho}{\partial t} + \nabla \cdot (\rho \vec{v}) = 0, \tag{1.2}$$

which expresses the conservation of matter. The Euler equation also applies:

$$\frac{\partial \vec{v}}{\partial t} + (\vec{v} \cdot \nabla)\vec{v} = -\frac{\nabla P}{\rho} - \nabla\Phi \tag{1.3}$$

which describes the conservation of momentum and the behaviour of the fluid under the influence of forces. The equation implies that the time derivative of velocity measured along the flow lines is affected by the pressure (P) gradient and the gravitational field Φ. For a pressure-free fluid as we considering here, however, $P \equiv 0$. Φ satisfies the Poisson equation:

$$\nabla^2\Phi = 4\pi G\rho \tag{1.4}$$

In general it is not possible to solve these three equations analytically (and they do not need to be, once there is the possibility of solving them via numerical methods). However, to expand the discussion a little more, let us consider the case of a homogeneous expanding cosmos, for which we can reach an analytical solution. In this case, within the framework of the so-called Newtonian Cosmology, we can write

$$\vec{v}(\vec{r}, t) = H(t)\vec{r} \tag{1.5}$$

This problem is more conveniently treated in comoving coordinates, so that we write the spatial position $\vec{r}$ and velocity field $\vec{v}$ as

$$\begin{aligned} \vec{r} &= a(t)\vec{x} \\ \vec{v}(r, t) &= \frac{\dot{a}}{a}\vec{r} + \vec{u}(\frac{\vec{r}}{a}, t) \end{aligned} \tag{1.6}$$

where $\vec{x}$ represents the comoving position of matter particles, and it is constant in a homogeneous cosmos. $a(t)$ is the scale factor, and $\vec{u}(\vec{x}, t)$ is a function of the comoving coordinate $\vec{x}$ and is called *peculiar velocity*.

After these transformations, the continuity equation 1.2, the Euler equation 1.3, and the Poisson equation 1.4, become, respectively:

$$\begin{aligned} &\frac{\partial \rho}{\partial t} + \frac{1}{a}\nabla \cdot [(1+\delta)\vec{u}] = 0 \\ &\frac{\partial \vec{u}}{\partial t} + \frac{\vec{u} \cdot \nabla}{a}\vec{u} + \frac{\dot{a}}{a}\vec{u} = -\frac{1}{\bar{\rho} a}\nabla P - \frac{1}{a}\nabla\phi \\ &\nabla^2\phi(\vec{x}, t) = 4\pi G a^2(t)\bar{\rho}(t)\delta(\vec{x}, t) = \frac{3H_0^2\Omega_m}{2a(t)}\delta(\vec{x}, t) \end{aligned} \tag{1.7}$$

where we used $\bar{\rho} = \rho_0 a^{-3}$ and the definition of the density parameter Ω_m (i.e., $\Omega_m = (8\pi G/3H_0^2)\rho_0$, ρ_0 being the mass density of the Universe today ($t = t_0$)) to rewrite the Poisson equation. Furthermore, the gravitational potential rewrites to

$$\Phi(\vec{r}, t) = \frac{2\pi}{3}G\bar{\rho}(t)|\vec{r}|^2 + \phi(\vec{x}, t); \tag{1.8}$$

where ϕ satisfies the "new" Poisson equation in comoving coordinates.

Without going too far in the details, the idea here is to look for approximate solutions of the above equations which describe small deviations from a homogeneous case (i.e., when $\delta \equiv 0$, $\vec{u} \equiv 0$, $\phi \equiv 0$, $\rho = \bar{\rho}$). In the linear case, as we are here, we disregard all terms containing $\vec{u}\delta$ or quadratic terms in $\vec{u}$. From the equations above it is also possible to eliminate the dependence in $\vec{u}$ and ϕ, and all we will be left with is the second order equations for the density contrast:

$$\frac{\partial^2 \delta}{\partial t^2} + \frac{2\dot{a}}{a}\frac{\partial \delta}{\partial t} = 4\pi G\bar{\rho}\delta \tag{1.9}$$

This equation has solutions of the form

$$\delta(\vec{x}, t) = D(t)\tilde{\delta}(\vec{x}), \tag{1.10}$$

meaning that the spatial and temporal components factorize: $\tilde{\delta}(\vec{x})$ is an arbitrary function of the spatial coordinate, while $D(t)$ is a function of time that obeys the equation

$$\ddot{D} + \frac{2\dot{a}}{a}\dot{D} - 4\pi G\bar{\rho}(t)D = 0. \tag{1.11}$$

This equation has two solutions, one that increases with time, and another that decreases. It follows that, if both solutions were present at earlier times, the decreasing one will become irrelevant, so that at later times only the increasing solution will remain. By denoting the increasing solution by $D_+(t)$, and imposing the normalization $D_+(t_0) = 1$, the expression for the density contrast will become

$$\delta(\vec{x}, t) = D_+(t)\delta_0(\vec{x}). \tag{1.12}$$

What is interesting about this solution is that, in terms of spatial shape in comoving coordinates, the density contrast will remain frozen. It will only evolve in terms of time, meaning that the amplitude of the density contrast will increase. This evolution is determined by the growth factor $D_+(t)$, which has an analytical solution for any cosmological model. Considering arbitrary values for the matter and dark energy densities Ω_m and Ω_Λ, $D_+(t)$ has a solution of the form

$$D_+(a) \propto \frac{H(a)}{H_0}\int_0^a \frac{da'}{\left[\Omega_m/a' + \Omega_\Lambda a'^2 - (\Omega_m + \Omega_\Lambda - 1)\right]^{3/2}}. \tag{1.13}$$

where H(a) is the Hubble parameter, but taking the scale factor a as argument.

1.1.2 | Non-linear perturbation theory: Model of Spherical Collapse

Until this point we treated only the evolution of structures by means of a linear perturbation theory. The truth is that this treatment has only a limited range of applicability, since the linear approximation breaks down when density perturbations get bigger and bigger, i.e., when $|\delta|$ is no longer $\ll 1$. In other words, to properly describe the evolution of structure when the

Universe already developed regions with higher density contrasts, such as in the case of clusters of galaxies, we need to consider a non-linear theory. Indeed, a big mathematical effort has being made in the search for analytical solutions considering higher orders of δ and $|\vec{u}|$, but the fact is that we can only achieve reasonable analytical solutions for some particular cases. In general, a smarter and effective approach is the application of numerical simulations. In any case, here we will treat briefly one of these simple solutions: the Model of Spherical Collapse.

Let us start with a spherical region in an expanding universe whose density is enhanced relative to the mean cosmic density $\bar{\rho}(t)$:

$$\rho(t) = [1 + \delta(t)]\bar{\rho}(t). \tag{1.14}$$

At earlier times, when $\delta(t_i) \ll 1$, the density perturbation will grow linearly, as we already saw, i.e., $\delta(t_i) = \delta_0 D_+(t_i)$, where δ_0 is the density contrast linearly extrapolated to the present day. Let R be the physical radius of the sphere, and $R_{\rm com} = R/a$ be its comoving radius. If we remember that for a matter dominated Universe $\bar{\rho} = \rho_0/a^3$, we conclude that the mass inside the sphere is

$$M = \frac{4\pi}{3} R_{\rm com}^3 \rho_0 (1 + \delta_i) \approx \frac{4\pi}{3} R_{\rm com}^3 \rho_0, \tag{1.15}$$

so that we have a direct relation between the initial comoving radius and the mass of the sphere, as long as $\delta(t_i) \ll 1$. As the Universe as a whole expands, the sphere will expand slighly slowly, increasing its density contrast. At a certain point, the expansion of the sphere will come to a halt, and its radius $R(t)$ will reach a maximum. Let us call this moment of maximum expansion of the sphere $t_{\rm max}$. After this moment, the sphere will start to collapse. From the time reversal symmetry of the equation of motion, the time until the full collapse of the sphere, $t_{\rm coll}$ will be two times the time to maximum expansion, i.e., $t_{\rm coll} = 2t_{\rm max}$.

If the sphere was perfectly homogeneous and the particles moved in perfecly radial orbits, it would collapse in a single point. But that clearly is not the case, so what happens in reality is that the particles will scatter due to fluctuations in the gravitational field of the sphere and will virialize. This process is called *violent relaxation*. At $t_{\rm coll}$ the sphere will be essentially virialized, and its average density will be

$$\begin{aligned} &\langle\rho\rangle = (1 + \delta_{\rm vir})\bar{\rho}(t_{\rm coll}), \\ &\text{where } (1 + \delta_{\rm vir}) \simeq 178\Omega_m^{-0.6}. \end{aligned} \tag{1.16}$$

This relation is the origin to the commonly used statement that a virialized region, such as clusters of galaxies, are regions with average density around 200 times that of the critical density of the Universe at the epoch of collapse, which in many cases can be approximated as an Einstein-de Sitter Universe, where $\Omega_m = 1$.

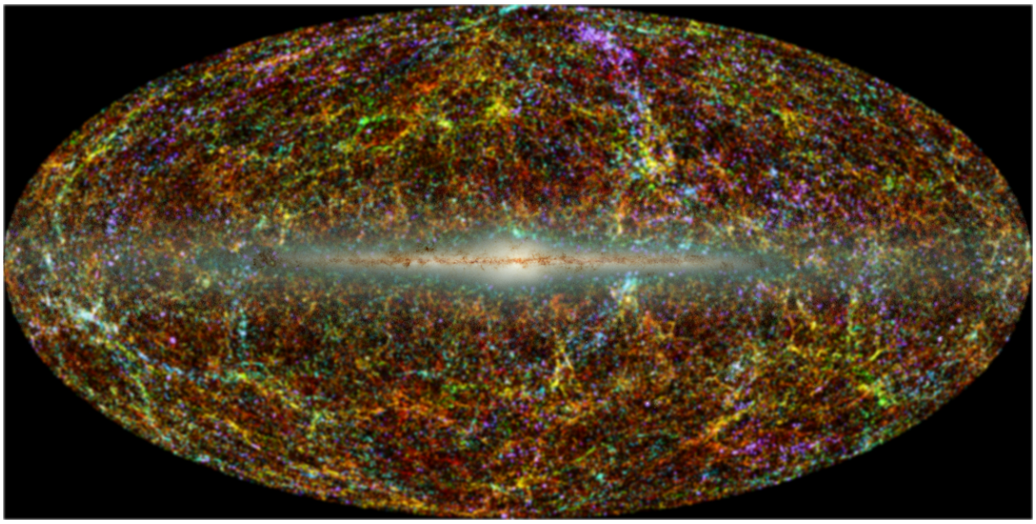

Figure 1.1: Sky distribution of galaxies in the 2MASS survey. Galaxies are color coded by their distance to us, with blue showing the nearest sources, through green and red representing the most distant sources. The Milky Way is represented in the center of the image. Figure extracted from https://lweb.cfa.harvard.edu/~dfabricant/huchra/2mass/.

1.2 | Surveys and the Large Scale Distribution of Galaxies

To understand how galaxies are scattered in the Universe, we need to observe large areas of the sky with telescopes. Such efforts aiming to collect information of galactic and extragalactic objects, are called astronomical surveys, or simply surveys. One of the first observations of galaxies covering a large patch of the sky was published by Shane and Wirtanen (1967), and consisted of a catalog of a count of galaxies on photographic plates from the Lick Observatory covering a vast extension of the Northern Hemisphere. This work resulted in the first studies of the distribution of galaxies in large scales, showing the tendency of clusters of galaxies to clump together into larger structures.

An important step was when de Vaucouleurs et al. (1991) published the Third Reference Catalog of Bright Galaxies (RC3), containing data on 23,000 galaxies with apparent diameters larger than one arc minute, magnitudes brighter than $m_B \approx 15.5$, and redshifts lower than 15,000 km s^{-1} ($z \lesssim 0.05$). Figure 1.2 shows the sky distribution of galaxies in the RC3. Notice that with this relatively shallow catalog it is already possible to notice several concentrations of galaxies into galaxy clusters going as distant as $d \approx 150h^{-1}$Mpc.

With time it became more and more clear that the large scale distribution of galaxies is not completely uniform, and that in fact it follows a pattern that has come to be called the Cosmic Web (Bond et al., 1996; van de Weygaert and Bond, 2008). The cosmic web, as the name suggests, can be described as an intricate web of galaxies scattered in virialized halos or not yet virialized clusters and groups that are interconnected by filaments and sheet-like structures (also called pancakes), which in turn surround low-density regions (voids). The cosmic web is a

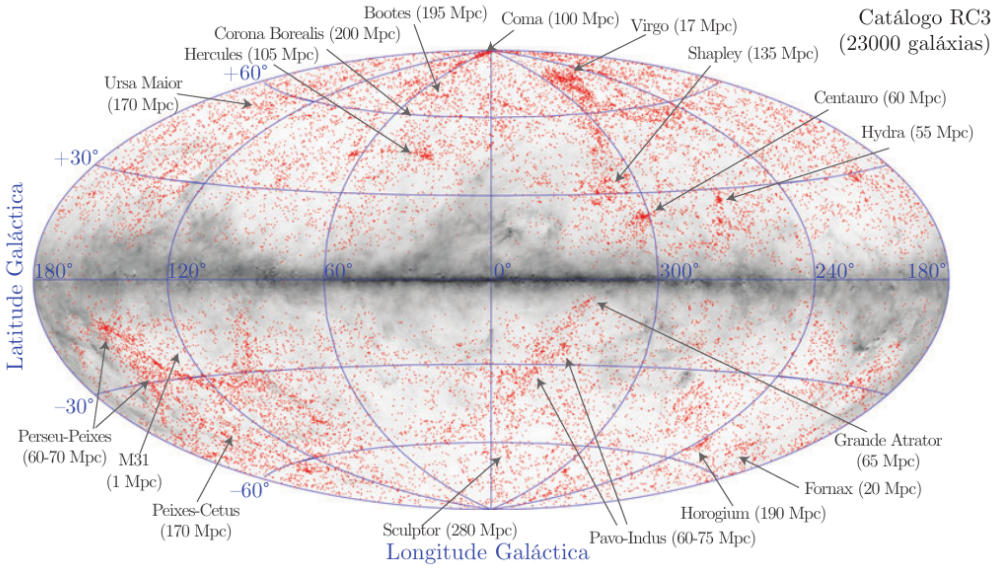

Figure 1.2: Sky distribution of the galaxies in the Third Reference Catalog of Bright Galaxies (RC3) from de Vaucouleurs et al. (1991). The grey region represents the distribution of dust in the plane of the Milky Way (Schlegel et al., 1998), and is known as the "Zone of Avoidance". Figure extracted from Lima Neto (2022).

clear manifestation of the anisotropic nature of gravitational collapse in the Universe, the motor behind the formation of structure, as we already discussed in the last section. It can be observed not only in large surveys, but also emerges in N-body numerical simulations (White et al., 1987; Springel et al., 2005; Vogelsberger et al., 2014a; The EAGLE team, 2017).

From the 1990s onwards there has been a great evolution in both photometric and spectroscopic surveys, which came as a result of growing investments in new telescopes, instruments and of techniques to analyze the data. One of the best examples of this is the Two Micron All Sky Survey (2MASS; Skrutskie et al., 2006), a photometric survey conducted between June 1997 and February 2001 from two dedicated 1.3m telescopes located at Mount Hopkins (Arizona) and Cerro Tololo (Chile), that collected data for 471 million point sources and 1.6 million extended sources (mostly galaxies). Since 2MASS observations were carried in the near-infrared J (1.25 μm), H (1.65 μm), and K_s (2.16 μm) bandpasses, it was able to observe galaxies behind the Milky Way disk, in the region called "Zone of Avoidance" (see figure 1.1). This is roughly a stripe region at low galactic latitudes in which the optical observations are attenuated by dense interstellar dust of the Milky Way. Infrared observations, though, have the advantage of penetrating most of the dust, allowing for observations in the Zone of Avoidance. The Zone of Avoidance is illustrated in figure 1.2 as the gray region close to the Galactic Plane.

Other examples of photometric surveys include the Dark Energy Survey (DES; The Dark Energy Survey Collaboration, 2005), Pan-STARRS1 (PS1; Chambers et al., 2016), and the DESI Legacy Imaging Surveys (Legacy Surveys; Dey et al., 2019).

Going beyond photometric and imaging surveys, we have the spectroscopic surveys, that differ from the photometric ones in that they employ instruments that will extract the eletromagnetic spectrum of objects. Although spectroscopy is much more expensive than photometry, the spectrum of an object provides information on the objects that cannot be achieved with the

same precision with photometry-only observations. One of such information, and arguably the more important, is the redshift. By means of the Hubble Law (Hubble, 1929) and its cosmological extensions (e.g. Hogg, 1999), the redshift can be used as an estimate of the distance to extragalactic objects, which means that spectroscopic surveys can be thought of as 3D surveys of the Universe.

However, we need to be a little careful when dealing with redshifts because in fact they do not show the distribution of objects in real space, but rather in velocity space. In other words, if the distances to the galaxies are determined via the Hubble Law, in most cases we need to assume that their velocities are entirely due to the expansion of the Universe (or Hubble flow), neglecting the fact that they actually possess a proper movement in relation to the Hubble flow. This proper movement, or peculiar velocity as more commonly known, are a consequence of the gravity pull from mass concentrations such as rich galaxy clusters. The tendency is that those galaxies that have a peculiar velocity pointing to the observer will have a lower observed redshift than what should be attributed only to the Hubble flow. On the opposite, galaxies with a peculiar velocity pointing away from the observer will have a higher observed redshift. The result is that rich galaxy clusters and other galaxy concentrations in redshift surveys appear elongated in the direction of the observer when plotted in velocity space. This is called the "fingers of God effect". Another closely related redshift space distortion is the Kaiser effect, that is related to infalling of galaxies in large scale structures such as filaments and superclusters as they assemble (Kaiser, 1987).

The finger of God effect can be seen in figure 1.3, that presents the distribution of galaxies from the 2-degree Field Galaxy Redshift Survey (2dFRGS) in redshift space. It is possible to notice that the galaxy distribution is stretched in the direction of the observer, specially in regions where they are more clustered. The 2dFRGS (Colless et al., 2003) is one the best examples of large redshift surveys. It measured redshifts of around 250.000 galaxies down to magnitudes $b_J = 19.5$ using the 2dF multi-fibre spectrograph installed at the Anglo Australian Telescope.

2dFRGS was the largest redshift survey from 1998, when it overtook the Las Campanas Redshift Survey (Shectman et al., 1996), and until 2003, with the ascension of SDSS (Abazajian et al., 2009), which is today the largest spectroscopic survey ever made. Its last data release (SDSS DR17; Abdurro'uf et al., 2022) includes a total of 1,231,051,050 survey objects, of which 208,478,448 are unique, primary sources identified as galaxies. SDSS represented a revolution in extragalactic astronomy, since spectra provide a variety of information on galaxy properties, and in cosmology, providing several ways to test the standard cosmological model against the observed large-scale distribution of galaxies. One of the most interesting findings with SDSS data was the Sloan Great Wall, a massive cosmic structure formed by the agglomeration of galaxies in a contiguous structure that resembles a wall spanning more than 400 Mpc in length (Gott et al., 2005).

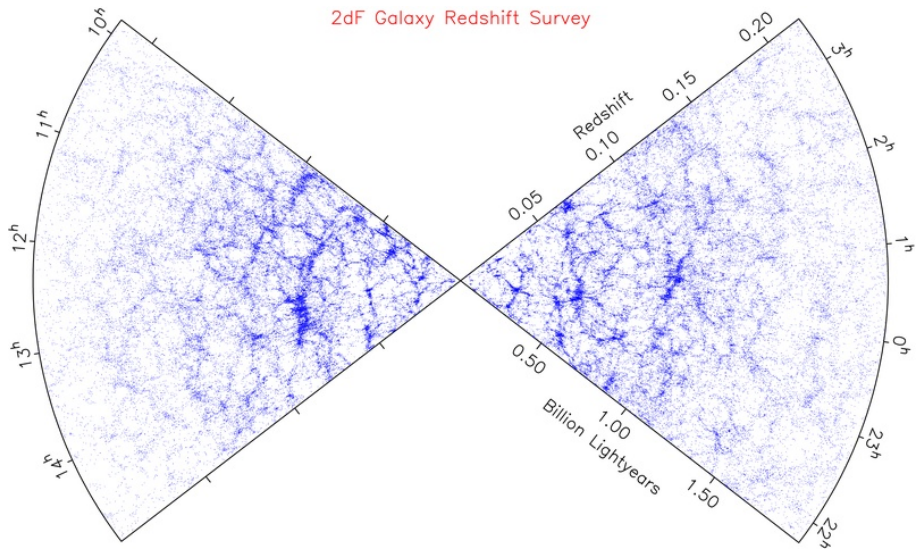

Figure 1.3: Redshift space distribution of galaxies in the 2-degree Field Galaxy Redshift Survey (2dFRGS). Figure extracted from http://www.2dfgrs.net/.

1.3 | Superclusters: definition, characteristics, influence on galactic evolution and cosmology

As the name suggests, superclusters are larger than clusters of galaxies, having typical sizes of around $\sim 30 - 100$ Mpc and typical masses of order $\sim 10^{15} M_{\odot}$. These systems are actually the largest assembly of galaxy clusters in the Universe (Sankhyayan et al., 2023b).

There is no unique definition of supercluster, and in the literature we find several different definitions for them, depending on the author's objective. For instance, in the context of LSS, they can be defined as (i) overdense gravitationally bound systems; (ii) overdense gravitationally unbound systems; (iii) converging peculiar velocity field regions. In the first case (definition (i)) we have e.g. Dünner et al. (2006), who discussed a model of spherical, gravitational collapse of a flat Universe to estimate the size and mass of bound structures in the Universe. With this model they were able to define a physical and practical criterion for the limits of a bound structure, such as superclusters, which has a minimum overdensity of 2.36 times the critical density of the Universe. Cases representing definition (ii) include the work of Einasto et al. (2007a), who compared properties of superclusters found in the 2dF Galaxy Redshift Survey (2dFRGS) with superclusters from the Millenium Simulation. They calculated the smoothed luminosity density field using an Epanechnikov kernel of radius 8 h^{-1} Mpc and defined as superclusters all contiguous regions with density field above a threshold density of 4.6 times the mean luminosity density. Another example appears in Lietzen et al. (2016), who discovered a massive supercluster at redshift $z \sim 0.47$, and for this they applied as definition of supercluster a density higher than 5 times the mean luminosity density of the region. Finally, for definition (iii) we find as an example the famous definition of our home supercluster, the Laniakea Supercluster, by Tully et al. (2014). They used a catalogue of peculiar velocities to trace the motions of galaxies in the

local universe, and defined Laniakea as the region delimited by the locations where the peculiar velocity of galaxies diverge from us, so that inside this volume the motion of galaxies converge.

Superclusters can be studied both individually or collectively through large catalogues obtained from deep surveys of galaxies, such as the 2dFRGS (Colless et al., 2003) and the Sloan Digital Sky Survey (SDSS) (Abazajian et al., 2009).

Large compilations of superclusters were applied, for instance, to study the morphologies and other physical characteristics of superclusters. Some of the main works in this direction were performed by M. Einasto and collaborators using data from large scale spectroscopic surveys such as 2dFRGS and SDSS. Starting with a catalogue of superclusters drawn from 2dFRGS, Einasto et al. (2007b) presented a method to study the morphology and internal structure of superclusters using Minkowski functionals and shapefinders. Their main resuls with this were that superclusters have elongated, filamentary shapes with high density clumps in the core regions. They also compared the observational results with those of model superclusters in the Millennium Simulation and found several differences, although they attributed the discrepancies to the small volume of the simulation, insufficient to cover all the variety of characteristics found in superclusters.

In a later work, Einasto et al. (2011a), this time studying a compilation of superclusters drawn from SDSS DR7, showed that in general superclusters have a filament-like overall shape, but also that these are more elongated, more luminous and with larger diameters than the non-filamentary ones. In the same work, they propose an interesting division of superclusters in four morphological classes: spiders, multispiders, filaments, and multibranching filaments. Using the same dataset, Einasto et al. (2011b) applied principal component analysis (PCA) and found that physical parameters of superclusters such as luminosity, volume and diameter are most equally important in shaping the properties of superclusters as morphological parameters (e.g. the clumpiness and shape).

Another work that investigates the properties of superclusters is Sankhyayan et al. (2023b), who identified 662 superclusters applying a friends-of-friends (FoF) algorithm on the WHL (Wen-Han-Liu) cluster catalog. The authors found that the median mass of superclusters is $\sim 5.8 \times 10^{15} M_{\odot}$ and the median size is $\sim$ 65 Mpc, although these values are found in a wide range of values, as can be seen in figure 1.4a, taken from the paper. Still in the same work, they investigated the effects of the superclusters environment on the cluster's properties, by looking at the mass distribution of clusters in the superclusters and in the field (i.e., clusters that are not members of any supercluster). The result was that clusters in superclusters are slightly more massive than those in the field, or, similarly, that there is a deficiency in less massive clusters in superclusters, showing that they indeed affect the properties of clusters (figure 1.4b).

Indeed, there is increasing evidence that the LSS environment, which include superclusters, affects the properties of galaxy clusters and of the galaxies that reside in those clusters. To cite a few studies on this matter, we have Gavazzi et al. (2010), Lietzen et al. (2012), Costa-Duarte et al. (2013), Luparello et al. (2013), Cohen et al. (2017), Guglielmo et al. (2018), and Santiago-Bautista et al. (2020). Starting at low redshifts, Santiago-Bautista et al. (2020) studied optical galaxies with spectroscopic redshifts from the SDSS DR13 beloging to 46 superclusters up to z = 0.15 and found correlations between galaxy properties (such as mass, morphology,

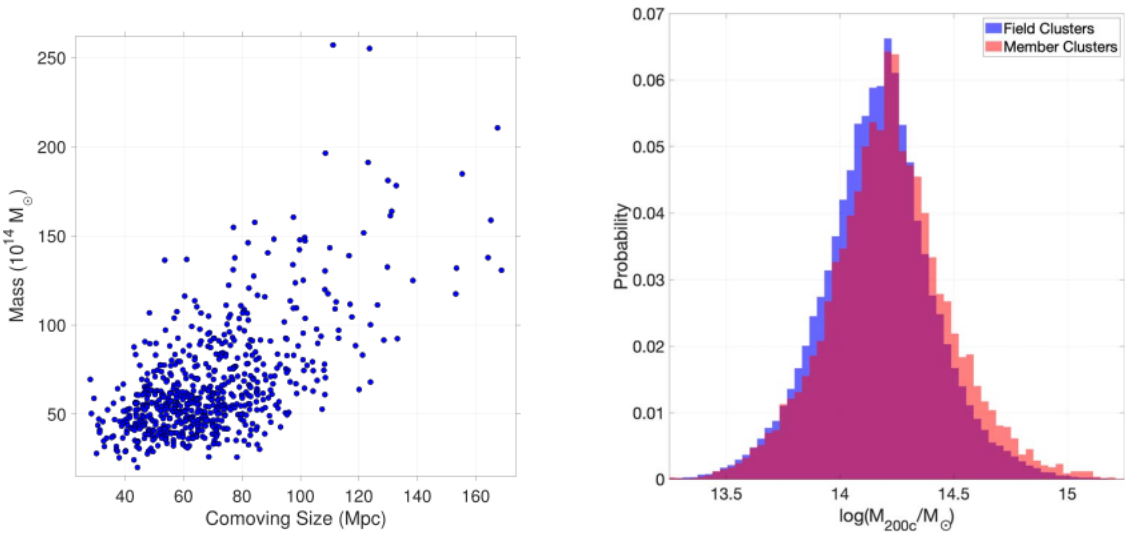

(a) *(b)*

Figure 1.4: (a) Relation between superclusters' mass and size. (b) Normalized histograms of the masses of clusters within superclusters (red histogram) and in the field (blue histogram). Figures extracted from Sankhyayan et al. (2023a).

and activity), and the environment in which they reside (clusters, groups, filaments, and the dispersed component). Their results suggest that galaxies closer to the skeleton of the filaments are up to 25% more massive than those located in the dispersed component, and also that the fraction of active galaxies, which include AGNs and star-forming galaxies, seem to decrease as galaxies approach the filament. A similar result is found by Gavazzi et al. (2010), who used data from the SDSS DR7 of 4132 galaxies in the Coma Supercluster, and showed that the fraction of early-type galaxies increases with the log of the over-density at the position of the galaxy, with their results suggesting a strong galactic evolution induced by environment (Nurture) at z=0.

This tendency to find a higher fraction of early-type and red galaxies, and a lower fraction of late-type, blue and active galaxies in denser environments within superclusters seems to be present also at higher redshifts. For instance, Guglielmo et al. (2018) studied a rich supercluster at $z \sim 0.3$ detected in X-rays by the XXL Survey with the goal of investigating the stellar populations of galaxies in different environments of the supercluster region. They separate galaxies in four types of environments (virial members, outer members, high-density field, and low-density field), and compute the fraction of star forming galaxies by means of their specific star formation rate (sSFR), and the fraction of blue galaxies defined in terms of their $(g - r)_{\rm restframe}$ color. With this, the authors find that the fraction of star-forming and blue galaxies are systematically lower among virial members than in the outer environments, while the fraction of star-forming galaxies seems to be enhanced among the population of outer members, even with respect to the high and low-density field. Figure 1.5 illustrates their findings showing the star-forming fraction/blue fraction of galaxies selected through sSFR and rest frame color, and the quenching efficiency (Q.E.)[1] for galaxies in the different environments of the supercluster. In summary, it

[1]In Guglielmo et al. (2018), the quenching efficiency (Q.E.) is defined according to Nantais et al. (2017) as $Q.E. = (F_{\rm passive/red,\ i} - F_{\rm passive/red,\ low\text{-}density\ field})/(F_{\rm star\text{-}forming/blue,\ low\text{-}density\ field})$, where $F_{\rm passive/red,\ i}$ is the fraction of passive/red galaxies in the environment under consideration, $F_{\rm passive/red,\ low\text{-}density\ field}$ is the fraction of passive/red galaxies in the low-density field, and $F_{\rm star\text{-}forming/blue,\ low\text{-}density\ field}$ is the fraction of star-forming/blue

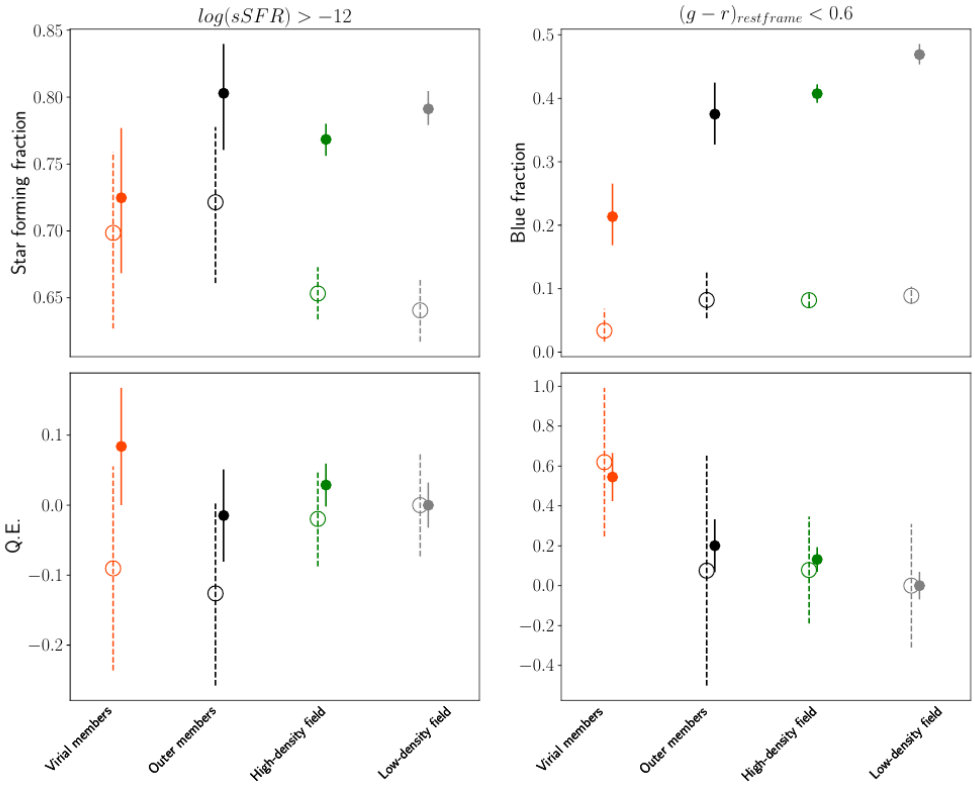

Figure 1.5: Star-forming fraction/blue fraction of galaxies selected through sSFR (left panel) and rest frame color (right panel) (top panels) and the quenching fraction (Q.E.) (lower panel) for galaxies in environments of different density scales, as indicated in the horizontal axis, within the supercluster XLSSsC N01. The fraction obtained via a magnitude-limited sample are represented with filled symbols and solid error bars, while the ones obtained using a mass-limited sample are represented by empty symbols and dashed error bars. Figure extracted from Guglielmo et al. (2018).

is becoming clear that superclusters are very rich environments and serve as a laboratory to test the evolution of galaxies.

Superclusters are also very interesting for cosmology, with one the big examples being the search for the missing baryons in the Universe. This is one of the most relevant cosmological parameters, having influence on how structures form on all scales, on the abundance of primordial nuclei, to the large scale distribution of galaxies and intergalactic gas. In fact, the density of baryons, Ω_b, represents a prediction from the Big Bang model that can be tested observationally. The estimated value for the baryon density according to recent cosmological studies is $\Omega_b h^2 = 0.0224 \pm 0.0001$ (Planck Collaboration et al., 2020b). The problem is that, according to observations at redshifts $z \lesssim 2$, if we sum all the baryons in the form of stars, the cold interstellar medium, residual Lyα forest gas, hot gas in clusters of galaxies, etc., we find just ∼50% of the expected baryons (e.g. Shull et al., 2012). This configures the so-called 'baryon problem' of cosmology. However, studies using hydrodynamical simulations (e.g. Cen and Ostriker, 1999) point out that most of the baryon matter in the Universe at low-redshift ($z < 1$) should be found in a very diffuse gas phase with temperatures $10^5 < T < 10^7$ K, which is not too cold to condense and form stars, but also not hot enough as the hot gas present in galaxy clusters. Most of the gas should account for the missing baryons and is probably distributed in large-scale sheet-like struc-

galaxies in the low-density field.

tures and filaments connecting galaxy clusters, all of these being structures that we find within superclusters. Radio observations of superclusters are able to detect the Sunyaev–Zel'dovich (SZ) signal originated from the interaction between this hot gas and photons from the CMB and can be used to search for the missing baryons in the Universe (e.g. Génova-Santos et al., 2005; Tanimura et al., 2019).

1.4 | Hydra Supercluster

As already mentioned, our work concentrates mainly in studying the galaxies and substructures of the Hydra Supercluster. We are defining Hydra Supercluster as the complex of galaxies comprised roughly in the rectangular region with $150° < \text{R.A.} < 180°$ and $-48° < \text{Dec.} < -15°$, and with redshifts in the interval $0.002 < z < 0.018$. In section 5.1 we elaborate on the details of how we defined Hydra Supercluster members for our work.

The Hydra Supercluster appears in the literature in several ways. For being a relatively poor supercluster, much of the times it is studied together with its larger neighbour, the Centaurus Supercluster, being defined as the "Hydra-Centaurus", "Centaurus-Hydra", or even "Hydra I-Centaurus" Supercluster (e.g. da Costa et al., 1986, 1987; Hopp and Materne, 1985). Although the two structures are commonly studied together, they are considered as two separate superclusters in the work of da Costa et al. (1987).

In figure 1.6 we have an interesting schematic representation of Laniakea Supercluster (Tully et al., 2014), the large structure of galaxies of which several smaller local structures are part of, including the Local Group. The Hydra Supercluster and its neighbour, the Centaurus Supercluster, are part of Laniakea, and can be seen in the right part of the figure. Hydra and Centaurus on their turn seem to be somehow connected also to the Local (Virgo) Supercluster.

The Hydra Supercluster is dominated by two main clusters of galaxies: the Hydra Cluster ($z \sim 0.012$, Babyk and Vavilova, 2013) and the Antlia Cluster ($z \sim 0.009767$, Crook et al., 2008). Hydra Cluster, Hydra I Cluster, or Abell 1060 (Abell et al., 1989), together with Centaurus and Virgo, is one of the largest clusters of galaxies in the nearby universe, being located at a distance of ∼50 Mpc (Misgeld et al., 2011; Arnaboldi et al., 2012). Hydra has no dominant central galaxy, but features two bright galaxies near its center: NGC 3309 and NGC 3311. NGC 3309 is a regular giant elliptical (E3), and NGC 3311 is a cD galaxy with an extended halo (Vasterberg et al., 1991). Their systemic (radial) velocities are 3825 ± 8km s^{-1} (Ventimiglia et al., 2010), and 4099 km s^{-1} (Misgeld et al., 2008) for NGC 3311 and NGC 3309 respectively. Based on the regular X-ray emission and temperature profile, it has been argued that Hydra Cluster can be considered as a prototype of an evolved and dynamically relaxed cluster, without any sign of major subcluster merger in the last several Gyr (Ventimiglia et al., 2011). The mass of the Cluster has been estimated using optical and X-ray data, resulting in values of virial mass $M_{vir} = 5.80 \pm 0.56 \times 10^{14} M_{\odot}$ and X-ray mass $M_X = 9.81 \pm 1.32 \times 10^{14} M_{\odot}$ (Babyk and

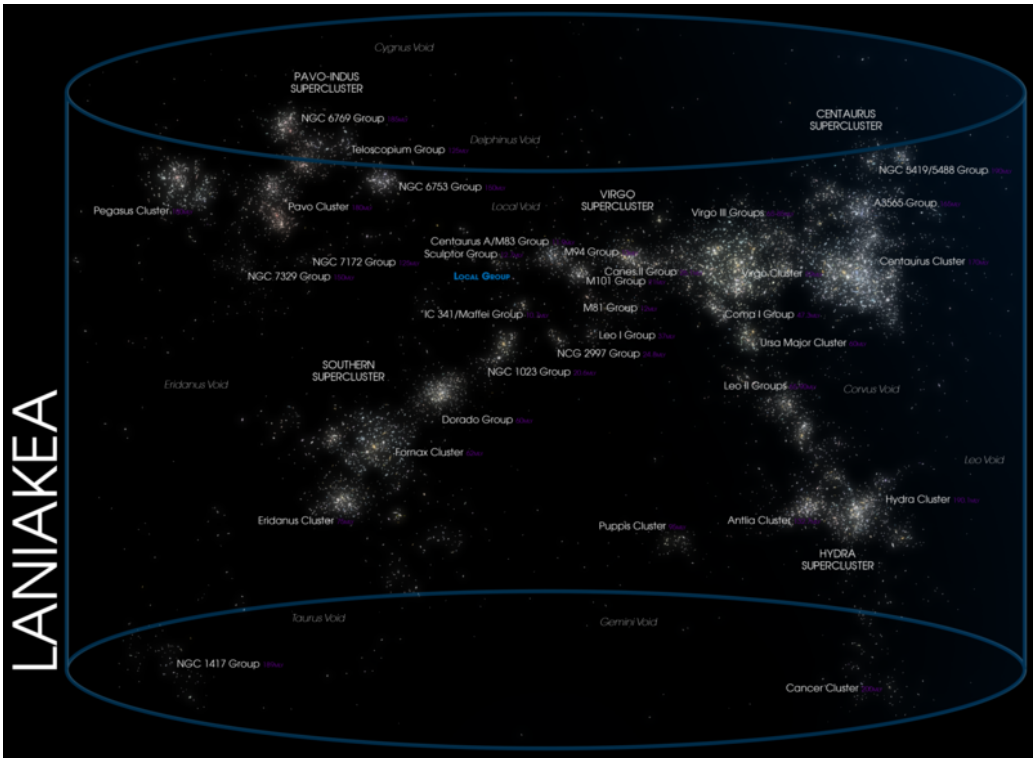

Figure 1.6: Schematic visualization of clusters and superclusters of galaxies within the Laniakea Supercluster. Credits: Andrew Colvin, Wikimedia.

Vavilova, 2013). After selecting galaxies with radial velocities only in the range from 1800 to 6000 km s^{-1}, Lima-Dias et al. (2021) found a biweight velocity dispersion for Hydra Cluster of 690 ± 28 km s^{-1}, which, after applying the relations from Leonard and King (2010), result in $M_{200} = 3.1 \pm 0.4 \times 10^{14} M_{\odot}$ and $R_{200} = 1.4 \pm 0.1$Mpc for Hydra. We apply the values of M_{200} and R_{200} (which are commonly refered as virial mass and virial radius in the literature) from Lima-Dias et al. (2021) for Hydra throughout the work.

Hydra Cluster appears in several studies interested in its galaxy population. For instance, Lima-Dias et al. (2021) used data from the Southern Photometric Local Universe Survey (S-PLUS; Mendes de Oliveira et al., 2019) to select 81 galaxies brighter than magnitude $r \sim 16$ inside $1R_{200}$ of Hydra Cluster and analyzed their structural (Sérsic index, effective radius) and physical (colors, stellar masses, and star formation rates) properties. They found that around 88% of the Hydra cluster galaxies inside $1R_{200}$ are already quenched. Other findings include a clear correlation between the Sérsic index in the r-band (n_r) and the galaxies' stellar mass, with higher values of n_r for larger stellar masses, as well as a correlation between the Sérsic index and the filters used, with early-type and late-type galaxies displaying a slight increase and a slight decrease, respectively, towards redders filters. Other works were interested in the dwarf population of Hydra. For instance, La Marca et al. (2022) searched for low-surface brigthness (LSB) galaxies and Ultra-Diffuse Galaxy (UDG) candidates in the inner ($\approx 0.4R_{vir}$) of the Hydra Cluster using deep images from the VST Early-type GAlaxy Survey (VEGAS), and added 11 UDGs and 8 LSB galaxies to already existing catalogs.

Antlia Cluster (Abell S0636) is another very interesting cluster of galaxies in Hydra Supercluster. In the same way as Hydra Cluster, Antlia is dominated by two bright elliptical galaxies

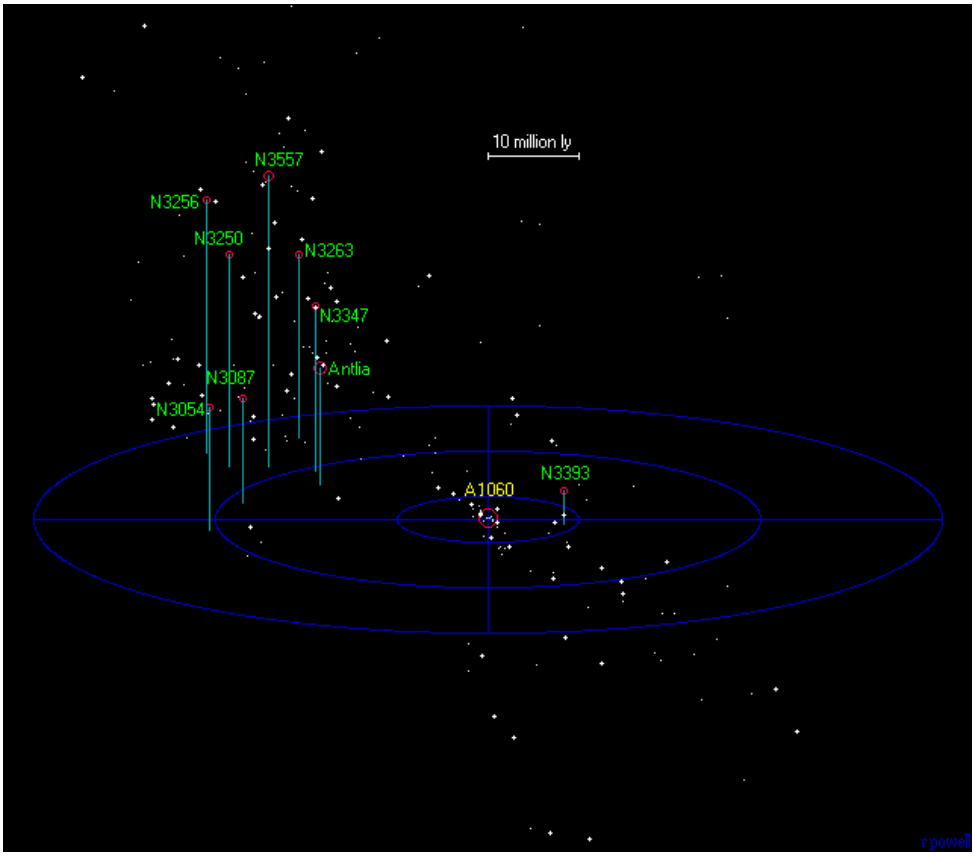

Figure 1.7: Three-dimensional map of Hydra Supercluster, displaying its 250 largest galaxies. Clusters and groups are indicated by their names. Figure extracted from http://www.atlasoftheuniverse.com/superc/hya.html

in its center: NGC 3268, and NGC 3258 (Calderón et al., 2020). The estimated distance to Antlia varies a little from work to work. For instance, Dirsch et al. (2003) gives the value of $D \sim$ 35.2 Mpc, while Cantiello et al. (2005) finds $D = 39.8$ Mpc. By means of X-ray observations, Antlia has been shown to be the nearest non-cool core cluster (Wong et al., 2016). The X-ray emission in Antlia is centered in NGC 3268, and is elongated towards the direction of NGC 3258, which is an indication that Antlia is accreting a subgroup centered on this galaxy (Wong et al., 2016; Pedersen et al., 1997; Nakazawa et al., 2000). Also from X-ray data we find some estimates for the radii and mass of Antlia. Wong et al. (2016) related the R_{500} radius to the X-ray temperature T_X of the Cluster and obtained $R_{500} = 51'$. Considering the angular scale of 11.6 kpc/1′ at the distance of 39.8 Mpc to Antlia, they estimate $R_{200} \approx 1.5R_{500} = 76' = 887$ kpc. In the same work, they estimate the mass of the Cluster as $M_{500(200)} = 5.9\ (7.9) \times 10^{13} M_{\odot}$.

In addition to the dominant Hydra and Antlia clusters, we can find in the literature several other smaller groups of galaxies in Hydra Supercluster. In table 1.1, we have a list of these clusters and groups, together with their sky position (R.A. and Dec.) and radial velocity (v). The same groups and clusters are displayed in figure 1.7, which helps to visualize the three-dimensional distribution of these groups. For reference purposes, our point of view of this figure can be thought approximately as a line connecting the NGC3363 and NGC3256 groups. Notice that Hydra Cluster, at the same time as it is the more massive structure in Hydra Supercluster, is also at the far side from us, having the largest radial velocity. The majority of the other

groups, as well as Antlia Cluster, clump in the region at the top-left, closer to us. Both figure 1.7 and the list of groups and clusters in table 1.1 were taken from The Atlas of the Universe website[2].

[2]http://www.atlasoftheuniverse.com/superc/hya.html

Cluster/group name	R.A. (deg)	Dec. (deg)	v (km s^{-1})	References
A1060 (Hydra)	159.17	-27.52	3,988	[1], [2]
AS0636 (Antlia)	157.51	-35.32	2,928	[3], [4]
NGC3054	149.53	-27.24	2,227	[5]
NGC3318	157.28	-40.35	2,460	[5]
NGC3256/3261	157.14	-44.24	2,339	[5]
NGC3263/3366	158.03	-43.90	2,688	[5]
NGC3347	160.63	-36.77	2,661	[5]
NGC3393/3463	162.10	-25.16	3,450	[6]
NGC3557	167.53	-37.40	2,619	[5]
NGC3087	149.78	-33.09	2,503	[7]

Table 1.1: List of known clusters and groups of galaxies in Hydra Supercluster. References: [1] Smith et al. (2004); [2] Piffaretti et al. (2011); [3] Crook et al. (2008); [4] Abell et al. (1989); [5] Garcia (1993); [6] Makarov and Karachentsev (2011); [7] Fouque et al. (1992).

1.5 | Goals of This Work

As we just saw, Hydra Supercluster is largely non-explored in the literature, with very few or no works dedicated to explore and understand all the substructures that are part of it. At the same time, it is home to Hydra Cluster, one of the richest clusters of galaxies in the nearby Universe, and Antlia Cluster, a dynamically interesting cluster and with a lot of unique features to be investigated. With this in mind, we decided to investigate the Hydra Supercluster of galaxies and its substructures using data from different sources. In specific, we focused our efforts in three main goals:

1. Create a catalogue of candidate galaxies to be observed by the CHileAN Cluster galaxy Evolution Survey (CHANCES) [3];

2. Implement a method to assign galaxy-cluster membership probabilities using photometric redshifts probability distribution functions (photo-z PDFs) and apply it for galaxies in the Hydra Supercluster;

3. Create lists of members of Hydra Supercluster, both in terms of galaxies and of groups and clusters of galaxies.

In other words, we aimed at determining members of Hydra Supercluster and of its clusters (at least the richest ones), creating catalogues and methods that will be useful for future works interested in studying, e.g., the properties and evolution of galaxies in clusters and superclusters.

Here we refer the reader to each of the chapters of this dissertation. We start by chapter 2, where we present the data we used in our work. In the sequence, we discuss the important process of star-galaxy separation in chapter 3. The creation of a catalogue of targets to be observed by CHANCES in the Hydra Cluster is presented in chapter 4. Chapter 5 is dedicated to discuss the methodology employed in the investigation of the whole region of Hydra Supercluster and the results obtained from it, what includes the determination of members of the Supercluster (section 5.1), the method applied to create a contrast density map of the Supercluster (section 5.2), the probabilistic galaxy-cluster membership method (section 5.3), and the creation of an idealized cluster mock (section 5.4) on which we test the membership method (section 5.5). The membership method is also tested on a "realistic" cluster mock in section 5.6 and on Hydra and Antlia clusters (section 5.7). We finalize this chapter with the description of a compilation of groups and clusters of galaxies in the volume of Hydra Supercluster in section 5.8. Finally, the conclusions of our work are presented in chapter 6.

Throughout this work, unless otherwise specified, a standard ΛCDM cosmology was adopted, with $H_0 = 71$ km s^{-1} Mpc^{-1}, $\Omega_m = 0.27$, and $\Omega_\Lambda = 0.73$.

[3] https://chances.uda.cl/

2 Data

In this work, we used data mostly from the fourth data release of the Southern Photometric Local Universe Survey (S-PLUS DR4) (Herpich et al. (*submitted*), section 2.1). S-PLUS is observing the sky with a photometric system of 12 filters (5 broad and 7 narrow bands) with the T-South, an 83 cm telescope at Cerro Tololo, Chile. This survey will provide high quality 12-band photometry for ≈ 9300 deg^2 in the southern skies in the near future.

In addition to S-PLUS data, we also make use of data from the Dark Energy Camera Legacy Survey (Dey et al., 2019, DECaLS, or Legacy henceforward, section 2.2) and from the extragalactic catalog provided by Gaia DR3 (Gaia Collaboration et al., 2022b, section 2.3). Both Legacy and Gaia provide a robust methodology to separate stars and galaxies, a property that was very useful in our work, as will be described in chapter 3. Also, by doing a crossmatch with Legacy and Gaia, we could get rid of most of the duplicate detections in S-PLUS, i.e., objects (mainly galaxies) detected more than once by SExtractor. Finally, Legacy data was required to perform our data selection of targets in Hydra Cluster for CHANCES (section 4).

In several occasions it was necessary to make use of spectroscopic data in our analysis. For this, we adopted the compilation from Lima et al. (in prep.) (section 2.4).

In this chapter, we describe the data we used in more detail.

2.1 | S-PLUS DR4

Most of the data we employ in this work comes from S-PLUS DR4. S-PLUS is one of the largest photometric surveys observing the southern hemisphere skies, and follows the success of the Sloan Digital Sky Survey (York et al., 2000, SDSS), in the same way as other photometric surveys such as 2MASS (Skrutskie et al., 2006), GALEX (Morrissey et al., 2007), and PanSTARRS (Chambers et al., 2016). Each of these surveys have their own characteristics, goals, instrument design, etc., making them complementary. For instance, S-PLUS has the outstanding characteristic of using the Javalambre 12-filter photometric system, consisting of five broad bands (the four SDSS-like bands, *griz*, plus the Javalambre u-band) and seven narrow bands (J0378: [O_{II}], J0395: Ca HK, J0410: Hδ, J0430: G-band, J0515: Mg-triplet, J0660: Hα, J0861: Ca-triplet). A more detailed description of S-PLUS, including its instrumentation, strategies and goals can be found in Mendes de Oliveira et al. (2019).

The most recent data release from S-PLUS, DR4, covers a total area of 3022.7 square degrees in the southern hemisphere, and is shown in blue in Figure 2.1. We downloaded, from the S-

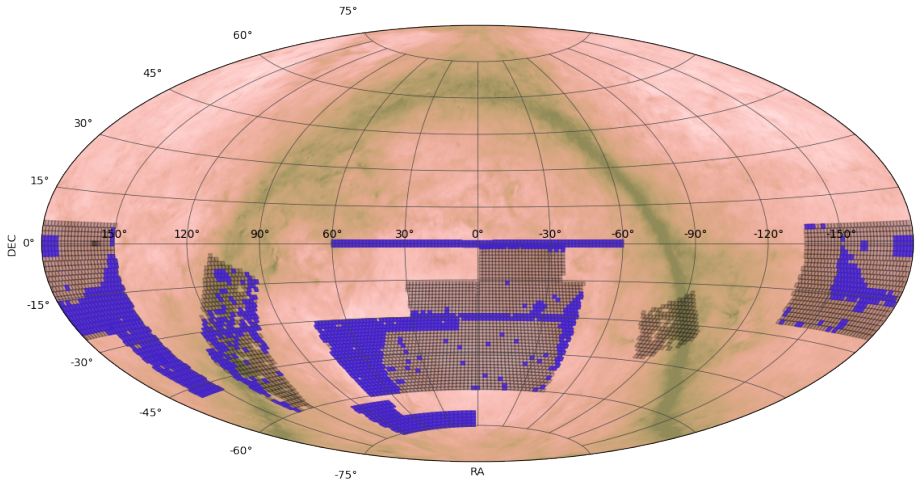

Figure 2.1: The area covered by observations from the S-PLUS internal Data Release 4 (iDR4), shown in blue.

PLUS Cloud [1], data from 333 fields in the region of Hydra Supercluster available in DR4. In section A.1 of the Appendix, we present the query applied to download this data.

S-PLUS also provides value added-catalogues (VACs) for star/galaxy/quasar classification (Nakazono et al., 2021) and photometric redshifts (Lima et al., 2022), both being very useful to our work.

Due to high costs of spectroscopic observations and the absence of comprehensive spectroscopic surveys such as SDSS in the southern hemisphere, photometric redshifts represent a fair alternative, and can be obtained by several methods applied over photometric data, such as template fitting, machine learning, and hybrid methods. In the case of S-PLUS, photometric redshifts were obtained using a type of supervised machine learning algorithm called Bayesian Mixture Density Network model (Bishop, 1994, 1997). This approach allows one to derive both single-point photometric redshifts (SPEs) and probability distribution functions (PDFs). In the first case, the photometric redshift is estimated as a fixed value, i.e., the maximum likelihood, or the peak of the distribution, while in the second it is represented by a probability distribution function, and there is no single value associated to the photometric redshift. In the case of S-PLUS photometric redshifts the PDFs are built through a combination of seven gaussian functions, each one with its associated width, mean and weight. This probabilistic nature of the photometric redshifts allowed us to assign probabilistic membership for galaxies in clusters, as will be described in detail in section 5.3. Throughout the dissertation, we may refer to photometric redshifts in abbreviated forms, such as photo-z, $z_{\rm photo}$, and z_p. See Lima et al. (2022) for a more in depth description of photometric redshifts in S-PLUS.

To illustrate how S-PLUS' photo-zs look like in the region of Hydra Cluster, in figure 2.2 we present histograms of photo-zs and spec-zs for objects classified as galaxies by S-PLUS (PROB_GAL > 0.8, where PROB_GAL stands for the probability of an object being a galaxy), and which are located inside the $1R_{200}$ area of Hydra Cluster. The figure is divided in six panels, each one selecting galaxies with a r_petro magnitude below a certain value, going from 16.0 to 21.0. The main feature in the histograms is the clear presence of a peak in the photo-z distri-

[1] https://splus.cloud

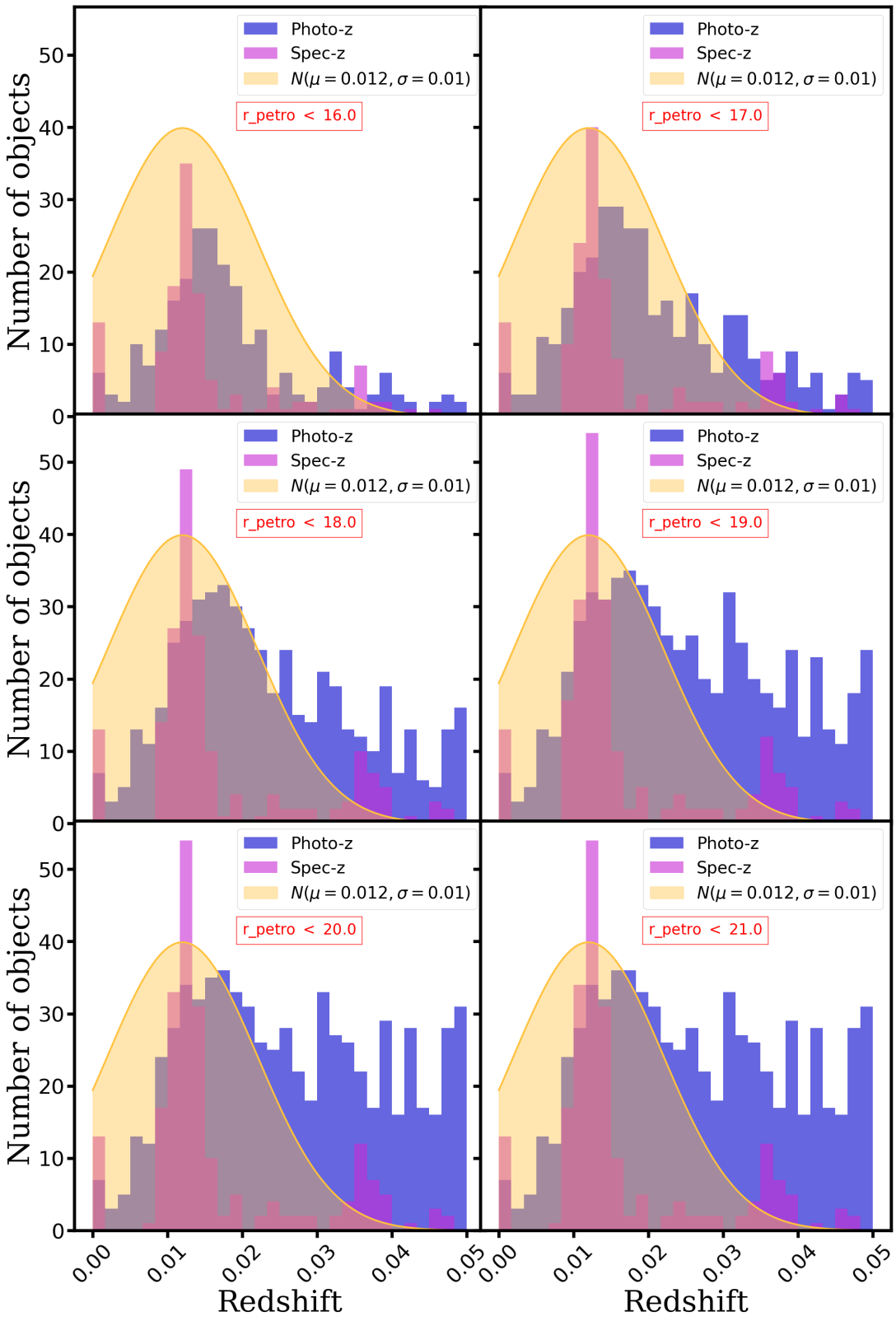

Figure 2.2: Histograms of photometric and spectroscopic redshifts for objects in the $1R_{200}$ region of Hydra Cluster. The yellow shaded region indicates a gaussian distribution centered in the spectroscopic redshift of Hydra ($z_s = 0.012$) and with standard deviation equal to the mean error in the photo-zs at low redshifts. Each panel shows the distributions for objects with r_petro magnitude below a certain value, from 16.0 to 21.0, as indicated.

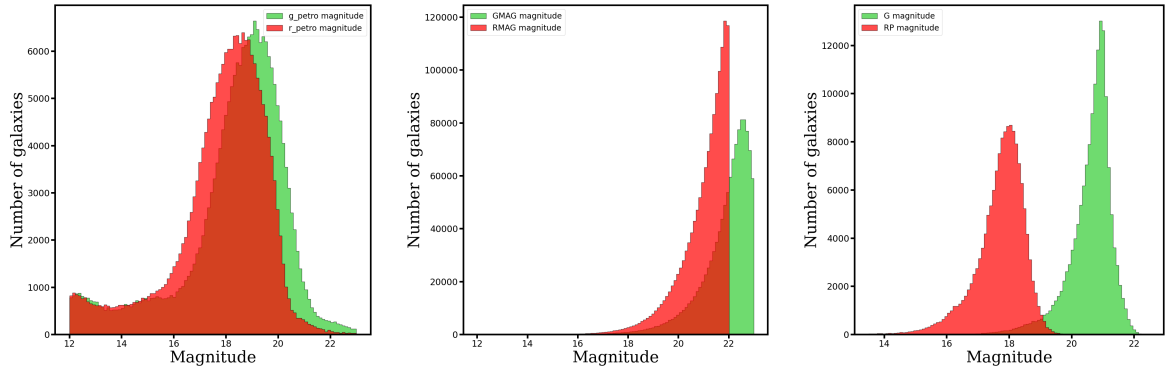

(a) *(b)* *(c)*

Figure 2.3: Magnitude distribution in r and g bands for objects selected as galaxies by each survey in the region of Hydra Cluster (DECaLS) and Hydra Supercluster as a whole (S-PLUS and Gaia) used in this work. From left to right: (a) S-PLUS (r_petro and g_petro magnitudes); (b) DECaLS (RMAG and GMAG magnitudes); (c) Gaia (G and RP magnitudes).

bution close to the redshift of Hydra ($z \approx 0.012$). Comparing to the distribution of spec-zs, the photometric redshifts display a little bias towards higher values, with the peak of the distribution being ~ 0.004 dex higher than spec-zs'. In each panel, we also plot a gaussian centered on the redshift of Hydra and with a width similar to the typical error in the photo-z estimates ($\sigma = 0.01$), which is roughly what we should expect for the distribution of photo-zs of galaxies in Hydra. We see that as we go for higher magnitude cuts, the photo-z distribution would almost match the gaussian curve if it was not for the bias in the values of photo-zs.

In figure 2.3a we present the distribution of r (r_petro) and g (g_petro) magnitudes of S-PLUS objects selected as galaxies (PROB_GAL > 0.8) in the region of Hydra Supercluster. The distribution can be considered complete up to magnitudes $r \sim 19$ and $g \sim 19.5$, with some objects being as faint as magnitudes 22 and beyond.

Furthermore, in figures 2.4 and 2.5, we have, respectively, a comparison of S-PLUS' r_petro and g_petro magnitudes with Legacy's RMAG and GMAg, and Gaia's G and RP magnitudes. The comparisons were made by cross-matching the surveys and selecting objects classified as galaxies by each one. It can be noticed from figure 2.4 that S-PLUS' and Legacy's magnitudes are mostly in agreement, concentrating around a 1:1 line. For fainter magnitudes, S-PLUS' magnitudes for some objects are lower than Legacy's, but that seems to be the case only for a small fraction of objects, and does not represent a big issue. On its turn, when comparing magnitudes of S-PLUS and Gaia (figure 2.5), we see a big disagreement mainly in G magnitudes, with Gaia's objects being systematically brighter by around 3 magnitudes than S-PLUS'. For R magnitudes, there is much more agreement, although Gaia still seems to be a little brighter than S-PLUS, specially for brighter objects. In any case, throughout the work, when working with the combination of S-PLUS and Gaia, we opt to employ only S-PLUS magnitudes, so that these differences have no impact on the results.

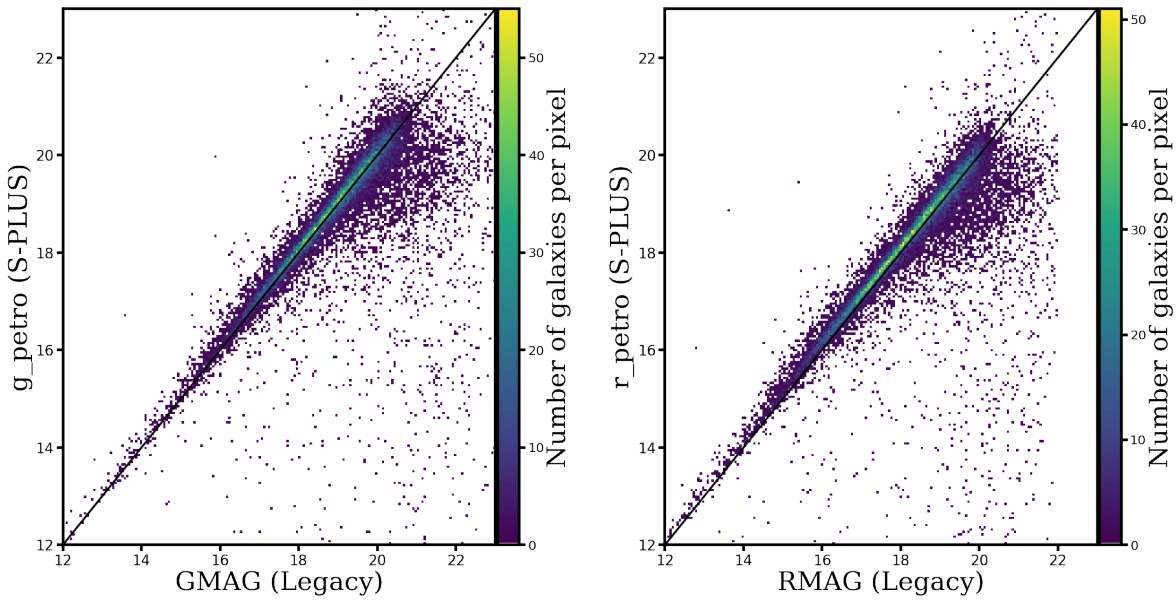

Figure 2.4: Comparison between S-PLUS' and Legacy's magnitudes. The plot was done using a cross-matched sample of objects classified as galaxies by each survey. The number of objects per pixel is indicated by the colorbar. The black line indicates the 1:1 relation between the magnitudes.

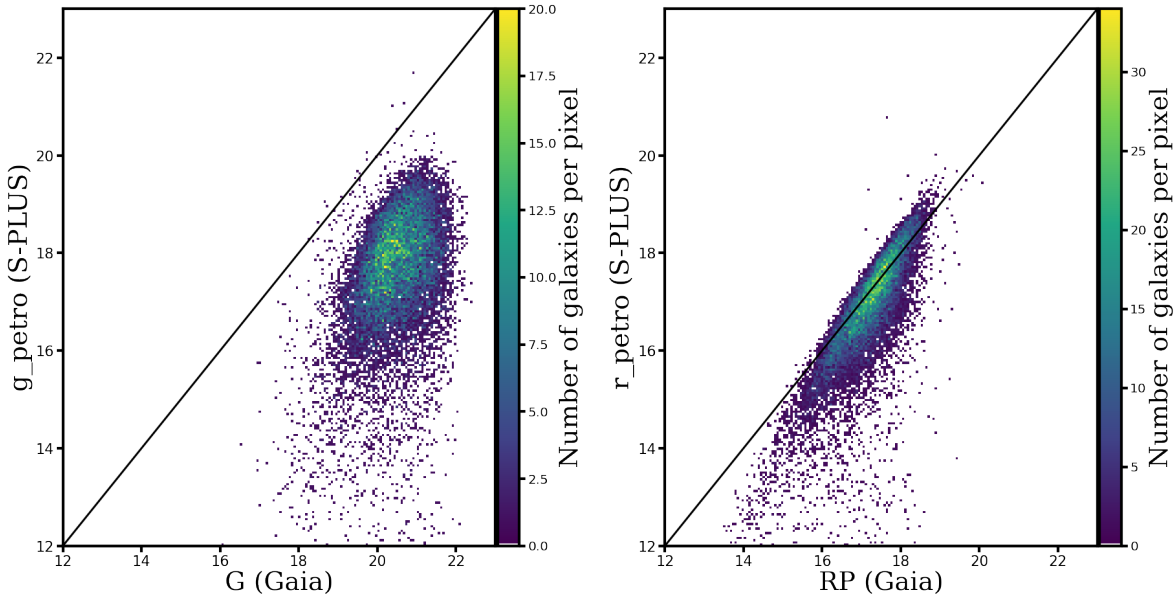

Figure 2.5: Comparison between S-PLUS' and Gaia's magnitudes. The plot was done using a cross-matched sample of objects classified as galaxies by each survey. The number of objects per pixel is indicated by the colorbar. The black line indicates the 1:1 relation between the magnitudes.

2.2 | DECaLS DR10

The Dark Energy Camera Legacy Survey (DECaLS), together with the Beijing-Arizona Sky Survey (BASS), and the Mayall z-band Legacy Survey (MzLS), make up the Dark Energy Spectroscopic Instrument (DESI) Legacy Imaging Surveys[2]. The three projects are observing ≈ 14000 deg^2 of the extragalactic sky in three optical bands (g, r, and z) using telescopes at the Kitt Peak National Observatory and the Cerro Tololo Inter-American Observatory (CTIO). The Dark Energy Camera (DECam), in particular, is installed at the 4m Blanco Telescope at CTIO, and is conducting the imaging for DECaLS, targeting a total of ≈ 3580 deg^2 in the South Galactic Cap (SGC) and ≈ 5770 deg^2 in the North Galactic Cap (NGC). Further information about DECaLS can be found in the paper of Dey et al. (2019).

In our work, we employ data from DECaLS DR10 to perform the selection of targets in Hydra Cluster to be observed by CHANCES (chapter 4). The dataset, containing information of almost 3.5 million stars and galaxies distributed in the region of Hydra Cluster, was provided to us via private communication by the CHANCES PI, Chris Haines, when the DR10 was not public yet. Because of that, the catalogue has some differences to what we would get directly from the public database. For starters, the objects are magnitude limited to r=22. This can be clearly seen in figure 2.3b, in which we present the distribution of r and g (or RMAG and GMAG as named in the catalogue) of objects classified as galaxies in the dataset. The sharp cut in r magnitude also reflects in an approximately sharp cut of the g magnitudes at magnitude $g \sim 23$. One caveat is that DECaLS data is not complete for the entire region of Hydra Cluster, as we show in figure 2.6, that presents the R.A. x Dec. distribution of galaxies in the dataset. Notice that the data covers most of the $5R_{200}$ region of the Cluster, but is still incomplete in the eastern and western parts.

Being almost complete down to r=22, DECaLS is deeper than S-PLUS and Gaia, which is interesting for several reasons. One of those is that the depth of the data allows for a very good star-galaxy separation based on morphological classification of the objects [4]. Objects in the DR10 of DECaLS are divided in several morphological types: point sources ("PSF"), round exponential galaxies ("REX"), de Vaucouleurs ("DEV") profiles (elliptical galaxies), exponential ("EXP") profiles (spiral galaxies), and Sersic ("SER") profiles. There is also a sixth morphological type, "DUP", which corresponds to Gaia sources coincident with, and hence were fit as, extended objects. In our "private" catalogue, all objects identified as extended sources (i.e., all except "PSF") were collected under one category identified by "SG = 0", where SG is the dataset column related to the star-galaxy separation (SG = 0 for galaxies, SG = 1 for stars). Furthermore, objects with morphological type "DUP" do not have global photometric measurements, and were automatically excluded by the magnitude cut.

[2] https://www.legacysurvey.org/

[3] Throughout the work, all circles plotted in R.A. x Dec. space are spherical circles, that is, circles formed by all points that are within a certain angle of the central coordinates on a sphere. This is necessary to represent a circle in sky coordinates.

[4] https://www.legacysurvey.org/dr10/description/#morphological-classification

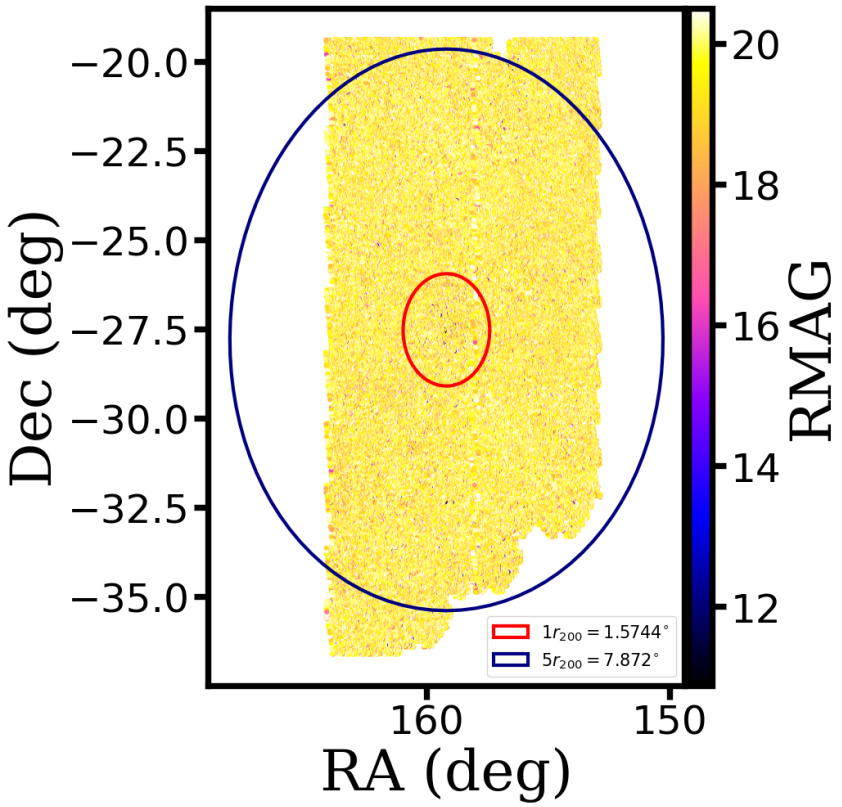

Figure 2.6: R.A. x Dec. distribution of galaxies in the DECaLS dataset used in this work. Red and blue circles indicate $1R_{200}$ *and* $5R_{200}$ *of the Cluster, respectively.* [3]

2.3 | Gaia DR3

The Gaia Mission, by the European Space Agency, is conducting one of the largest studies of stars and other point sources all over the Milky Way. It has observed around 2 billion objects, and has as its primary objective to study the structure and origin of our Galaxy by measuring the distribution, kinematics, and physical properties of its constituent stars (Gaia Collaboration et al., 2016). However, since Gaia is observing the sky multiple times down to a limiting magnitude of G$\sim$ 21, it is also providing observations for millions of extragalactic objects, including galaxies and quasars. Data on these objects is provided as a sub product of the the Third Data Release of Gaia (Gaia Collaboration et al., 2022a, Gaia DR3).

The process behind how extragalactic objects are classified by Gaia is described in depth in Gaia Collaboration et al. (2022b). In summary, Gaia data processing system is equipped with several modules dedicated to the classification of objects. The modules are provided by different and mostly independent coordination units (CUs). Each CU is responsible for analyzing different types of data, for instance: definition of an astrometric reference frame from a pre-defined list of extragalactic point sources (CU3), surface brightness profiles (CU4), varibility from photometric light curves (CU7), classification of objects and estimation of redshift by analysing their astrophysical parameters (CU8). While CU3 and CU4 work with a pre-defined

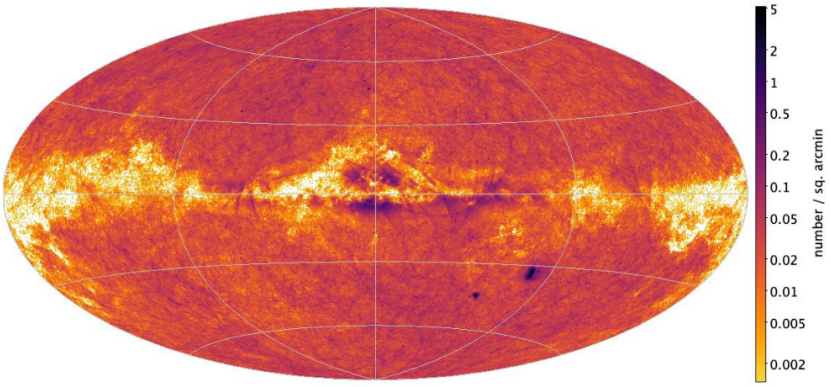

Figure 2.7: Sky distribution of Gaia extragalactic content. Figure extracted from Gaia Collaboration et al. (2022b).

list of extragalactic objects, the modules in CU7 (Vari) and CU8 (Discrete Source Classifier, DSC) apply a supervied machine learning for their characterization.

The `galaxy_candidates` table that we employ in our work is built via a combination of the classifications from the different Gaia modules, and has an estimated purity of 69%. Although a purer subsample can be obtained with additional cuts on the data, we decided to stay with a more complete sample of objects for our study. Anyway, by combining Gaia with S-PLUS, we get a much purer sample of galaxies, as we describe in chapter 3.

There are several examples of studies that combine Gaia data with other surveys to identify extragalactic objects and analyse the properties of galaxies and quasars (Paine et al., 2018; Souchay et al., 2019, e.g.). In the same way, we are relying on the extragalactic content of Gaia DR3 to improve the selection of galaxies in the region of Hydra Supercluster by cross matching it with S-PLUS DR4 data.

Different from DECaLS data, which is available only for a region of roughly $5R_{200}$ around Hydra Cluster center, Gaia extragalactic content covers the entire sky (figure 2.7), making it suitable to be applied for the entire region of the Supercluster. For homogeneity reasons, we then employ Gaia + S-PLUS data on the study of Hydra Supercluster as a whole, without mixing it with DECaLS data, which, as already mentioned, is employed only for CHANCES target selection. Unfortunatelly, Gaia has the disadvantage of being shallower than S-PLUS in the r-band, as can be seen in figure 2.3, going just as deep as magnitude $r \sim 18$.

In the Appendix (section A.2) we present the query applied to download the Gaia extragalactic database data in the region of Hydra Supercluster.

2.4 | Spectroscopic Catalogue

Although our work is focused on photometric data of galaxies, we also employed spectroscopic redshifts of galaxies available in the literature in several occasions when it was necessary to test

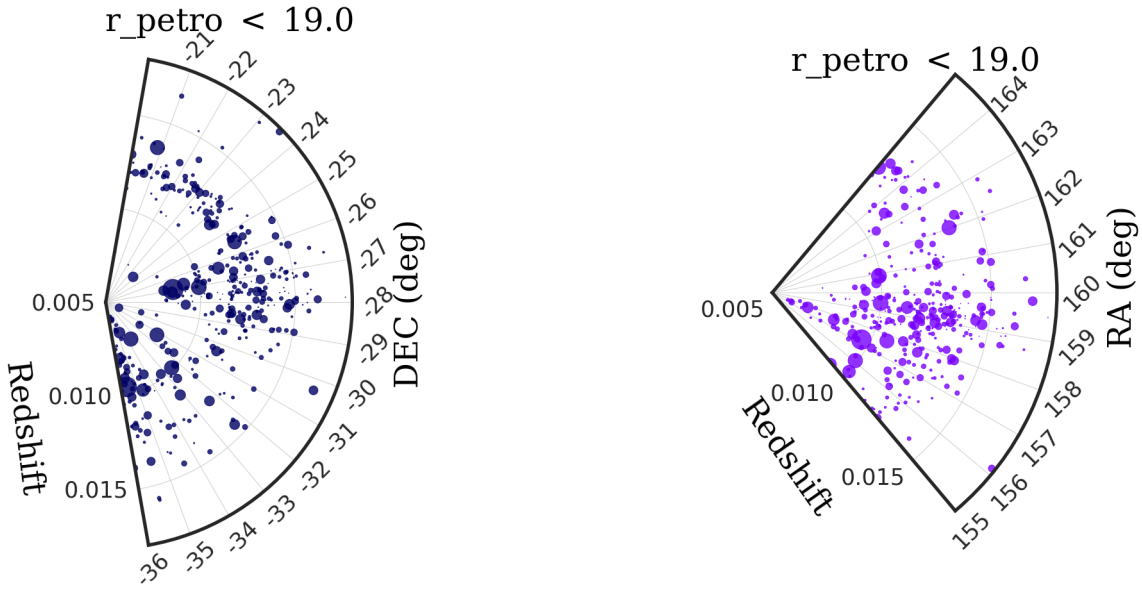

(a) *(b)*

Figure 2.8: Cone plots in declination (left) and right ascencion (right) of spectroscopic objects in the region of Hydra Cluster. Object sizes are inversely proportional to their magnitudes.

the accuracy of our methods. For example, in chapter 4, we estimate the completeness and purity of the Hydra Cluster catalogue using the Cluster's spectroscopic members; similarly, spectroscopic data came in handy to compute the completeness and purity of the Hydra, Antlia and AS0639 clusters' catalogues obtained with a probabilistic galaxy-cluster membership method, as will be described in section 5.7.

These spectroscopic redshifts come from a compilation of 3.800+ catalogues originated from services such as Vizier, HEASARC, SDSS, and others (Lima et al. (in prep)) [5]. It contains spectroscopic information of 5.624.559 objects all over the Southern Hemisphere (below $+5^{\circ}$ declination). A total of 2.673.964 of these objects are classified as galaxies. Notice, however, that this spectroscopic catalogue cannot be considered complete in any sense. The catalogue shall be published in the next months.

In figure 2.8 we present cone plots in declination (figure 2.8a) and right ascension (2.8b) to illustrate the distribution of galaxies in the spectroscopic catalogue in the region of Hydra Cluster. From these plots it is evident the higher number of galaxies with redshift $z \sim 0.012$, corresponding to Hydra Cluster, and with redshift $z \sim 0.009$, corresponding to Antlia Cluster.

[5] https://github.com/ErikVini/SpecZCompilation

3 Star-galaxy separation

One of the more fundamental steps when we want to study a galaxy supercluster is the separation between stars - and other contaminant objects - and galaxies in our sample. In the case of S-PLUS, we usually rely on the parameter PROB_GAL to dictate the probability of an object being a galaxy. The closer PROB_GAL is to unity, the more probable that object is a galaxy (see the work of Nakazono et al., 2021).

By carrying out a visual inspection of the objects selected with a PROB_GAL > 0.8 cut, we noticed a large fraction of contaminant objects (stars, spikes of saturated stars, etc.). An example is in figure 3.1, in which we plotted 25 objects randomly selected with the above criteria, but most of them are not really galaxies.

It is not straightforward to tell the exact fraction of contamination, because of the large number of objects to be analyzed and the fact that some objects have multiple detections in S-PLUS. But, as an alternative, we can make a comparison with the star-galaxy (SG) selection of the Legacy Survey, which, by being a deeper survey, shall provide purer and more complete star-galaxy separation. This is presented in figure 3.2, in which we have the purity and completeness of the star-galaxy separation using several values of PROB_GAL cut (from 0.5 to 0.95). We define purity and completeness as

$$C = \frac{\text{Legacy galaxies} \cap \text{S-PLUS galaxies}}{\text{Legacy galaxies}} \tag{3.1}$$

$$P = \frac{\text{Legacy galaxies} \cap \text{S-PLUS galaxies}}{\text{S-PLUS galaxies}} \tag{3.2}$$

where "Legacy galaxies" and "S-PLUS galaxies" are objects classified as galaxies by Legacy and S-PLUS, respectively.

We present the values obtained for $z_p < 0.03$ (Fig. 3.2a) and $z_p < 0.1$ (Fig. 3.2b), which is a more generous cut, so that we can also test the SG separation for different ranges of photo-z. From the plots it is clear that, although the PROB_GAL cuts maintain a fair value of completeness, the contamination will be significantly high, especially when selecting for objects with lower values of z_p.

In summary, it became clear to us that, if we want a more pure sample of galaxies, the PROB_GAL parameter is not enough. Because of this, we tested other approaches to make the contamination lower.

The first attempt was to crossmatch our sample with some other survey that could improve the star-galaxy separation criteria. At this point we had already used Legacy Survey's star-galaxy separation to estimate the purity and completeness of our sample (and especially for the selection of targets for CHANCES). The point here is that our goal as a whole is to study the whole Hydra Supercluster, not only Hydra Cluster, and, as already described, the last data release of Legacy

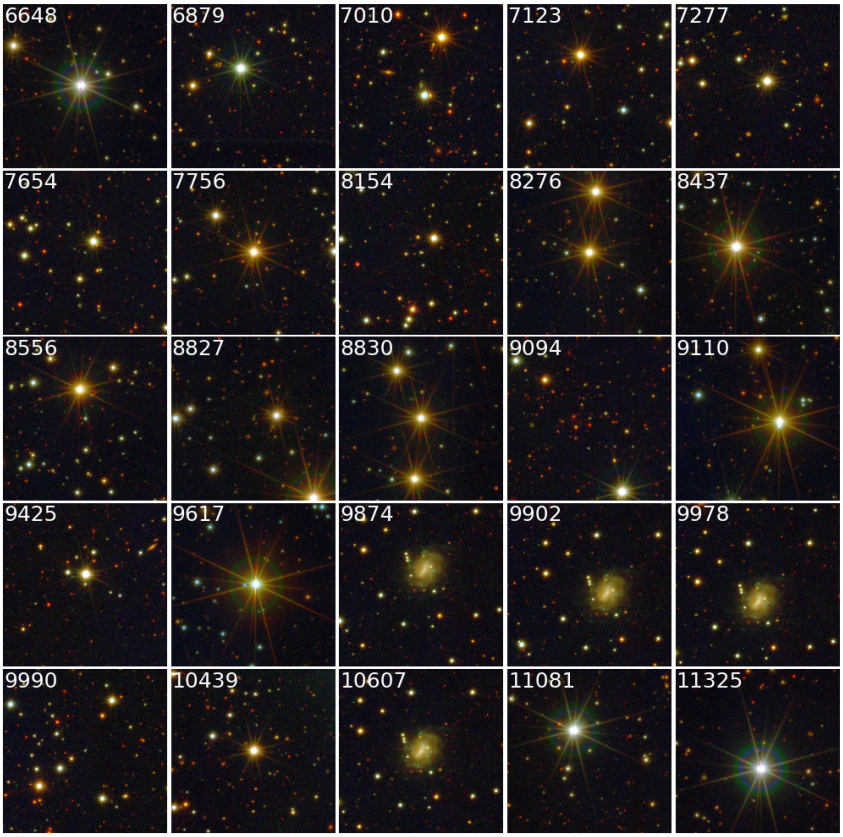

Figure 3.1: Example objects selected with PROB_GAL > 0.8 in a S-PLUS catalogue. Notice the large fraction of contamination by stars, spikes by saturated stars, duplicate objects, etc.

Survey (DR10) covers just the region immediately around Hydra Cluster. Therefore, we adopted Gaia extragalactic database to improve the selection of galaxies when studying the whole region of Hydra Supercluster.

At the same time we explored other auxiliary star-galaxy separation methods, in particular one using the ISOarea × r_petro diagram. In this diagram, we see that stars (contaminants) tend to have smaller values of ISOarea as a function of magnitude than the galaxies. This separation can then be done as a function ISOarea(r_petro), shown in Figure 3.3, with the red line marking this separation for a set of objects in the Hydra Supercluster region.

It can be noticed that, by using the PROB_GAL cut together with the ISOarea × r_petro selection, we can maintain a high value of completeness in our selection while improving a little the purity when compared to just using the PROB_GAL. This selection was done by using a catalogue of objects in the Hydra Supercluster region, observed by S-PLUS, crossmatched with a sample of galaxies in Gaia. We saw that, even after doing the crossmatch with Gaia, we did not get rid of all contamination in Hydra Supercluster, so we still needed to use other ("S-PLUS-ish") selection methods. The results are presented in table 3.1.

We see that using both PROB_GAL + ISOarea(r_petro) cuts, we get purer samples while still maintaining a good value of completeness. For regions not too close to the Milky Way, where the contamination tends to be lower, the purity goes as high as 88%, which is already fairly good for many purposes. For regions closer to the Milky Way, the purity is a little lower, but still workable.

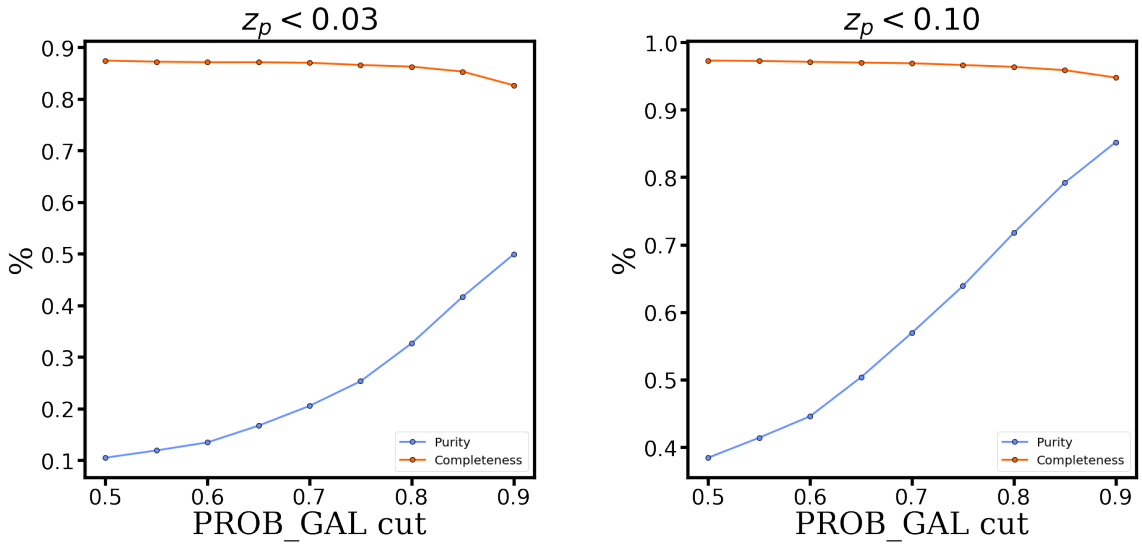

(a) *(b)*

Figure 3.2: (a) Completeness and purity of star-galaxy separation in S-PLUS as a function of the PROB_GAL cut for $z_p < 0.03$; (b) Completeness and purity of star-galaxy separation in S-PLUS as a function of the PROB_GAL cut for $z_p < 0.1$.

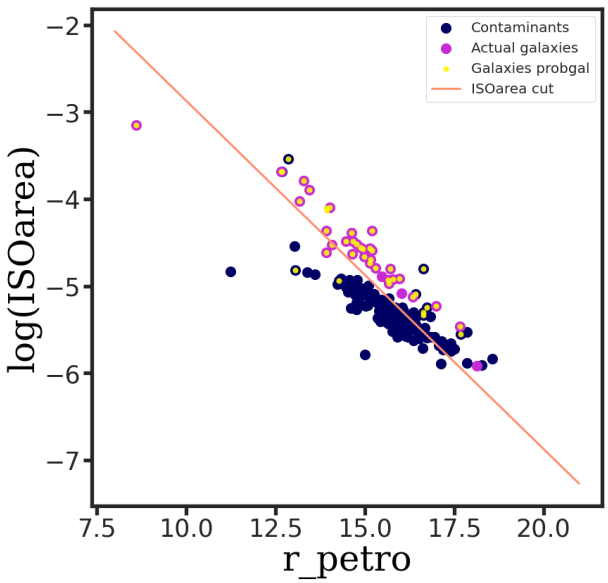

Figure 3.3: The ISOarea x r_petro diagram for a "training sample" of objects in the region of Hydra-Centaurus. Objects visually selected as contaminants and as galaxies are shown in lime and orange respectively, while the blue dots mark the objects selected using PROB_GAL > 0.8. The red line marks a rough separation between contaminants and galaxies.

Objects within -44 <DEC <-42 (closer to the Milky Way)		
	Just PROB_GAL >0.7	PROB_GAL >0.7 + ISOarea(r_petro) cut
Purity	71%	74%
Completeness	94%	91%
Objects within -34 <DEC <-29		
	Just PROB_GAL >0.7	PROB_GAL >0.7 + ISOarea(r_petro) cut
Purity	82%	88%
Completeness	99%	99%

Table 3.1: Purity and completeness of the two SG-separation methods: applying just the PROB_GAL cut, and applying the PROB_GAL + ISOarea cut. The values are presented for two different declination bands of Hydra Supercluster, as indicated.

Using a S-PLUS – Legacy Survey crossmatched sample, we also computed the purity as a function of the magnitude cut for the different selection criteria, and using the star-galaxy selection of Legacy as the "true" classification (Figures 3.5a and 3.5b). In figure 3.5b, we show the purity without applying any cuts in photo-z, while in figure 3.5a we do the same but this time applying a cut of $0 < z_p < 0.03$. Doing this cut in photo-z we see that the purity gets much worse. So, it is useful to have in mind that the selection methods are sensitive to the magnitude and photo-z cuts we apply to our samples.

We just have to be a little cautious about such comparisons between S-PLUS and Legacy because the star-galaxy classification of Legacy, although very good, is not perfect. Indeed, using a random sample of 100 objects of a S-PLUS/Legacy-crossmatched catalogue, we can compute a rough estimate of the Legacy SG-selection purity. Taking 100 objects classified as galaxies by Legacy, we found 81 of them to be actually galaxies (by visual inspection). At the same time, taking 100 objects selected using the PROB_GAL + ISOarea selection of S-PLUS, without the aid of Gaia or Legacy SG-selection, only 25 of them were actually galaxies.

Given the above, our decision was: for the CHANCES target selection in the region of Hydra Cluster, which is observed by Legacy Survey, we rely entirely on the star-galaxy classification of Legacy Survey; for the remaining work, regarding the whole region of the Hydra Supercluster, which is in a big part not observed by Legacy, we relied on a joint star-galaxy selection of Gaia + PROB_GAL + ISOarea(r_petro), given it is a reasonable idea to have a purer sample of galaxies on which we can have reliable results.

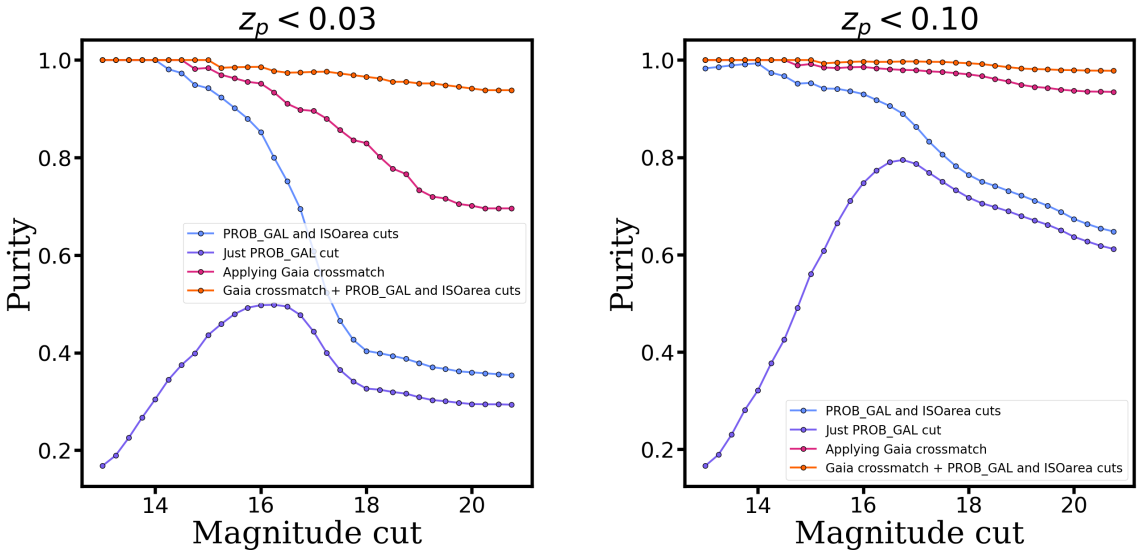

(a) *(b)*

Figure 3.4: (a) Purity as a function of the magnitude cut for a cut in PROB_GAL and a cut in PROB_GAL + ISOarea, after applying $0 < z_p < 0.03$; (b) Purity as a function of the magnitude cut for a cut in PROB_GAL and a cut in PROB_GAL + ISOarea, without applying any cuts in the photo-z.

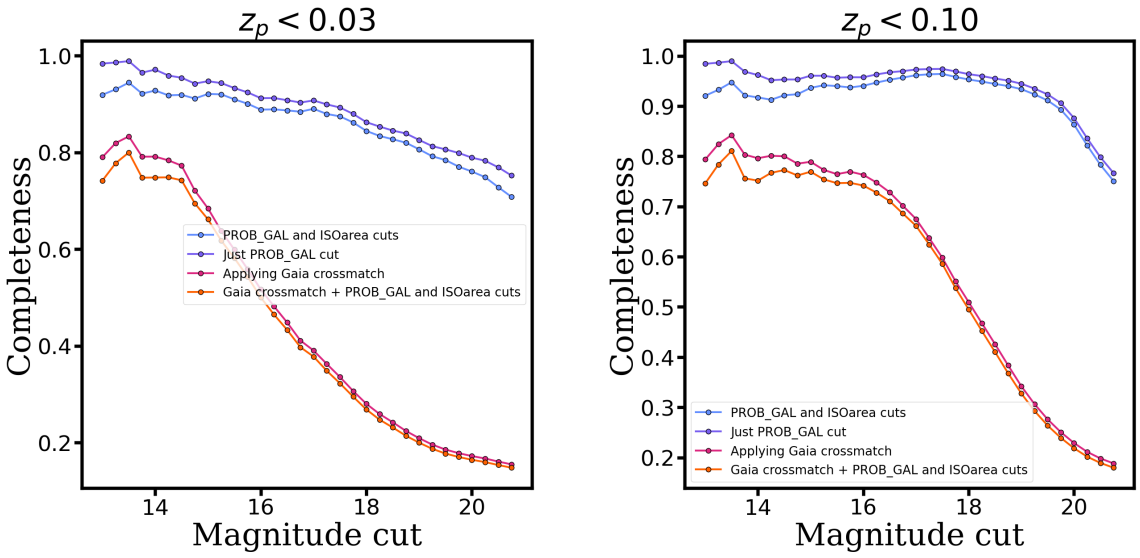

(a) *(b)*

Figure 3.5: (a) Completeness as a function of the magnitude cut for a cut in PROB_GAL and a cut in PROB_GAL + ISOarea, after applying $0 < z_p < 0.03$; (b) Completeness as a function of the magnitude cut for a cut in PROB_GAL and a cut in PROB_GAL + ISOarea, without applying any cuts in the photo-z.

4 Target selection for CHANCES

CHANCES stands for CHileAN Cluster galaxy Evolution Survey, and it aims to provide legacy spectroscopic support for the eROSITA X-ray mission, complementing the 4MOST Consortium eROSITA Cluster Redshift Survey (S5). The observations will be carried with the 4-metre class telescope VISTA (Visible and Infrared Survey Telescope for Astronomy), that will be equipped with the 4-metre Multi-Object Spectroscopic Telescope (4MOST)[1], a facility that will be able to obtain spectra of ∼2400 objects distributed in a field of view of 4.2 square degrees. CHANCES, in particular, will target around 500.000 galaxies around 150 of the most massive clusters over $0 < z < 0.4$, extending up to $5R_{200}$ and down to $r_{AB} \sim 21$. We are collaborating with the CHANCES team by making the selection of targets in the Hydra Cluster. In this chapter, We describe how we performed the target selection for Hydra, and how the submitted catalogue looks like.

When performing the target selection for CHANCES, some points need consideration: i) 4MOST observations require, preferentially, the astrometry from DECam Legacy Survey; ii) although Legacy Survey provides photometric redshifts for some of its observed galaxies, S-PLUS provide them for much more objects and with greater accuracy, making it more appropriate to be used in the target selection; iii) Legacy Survey's star-galaxy separation, for being more robust, as described in the last section, is prefered over S-PLUS'; iv) we want targets for magnitudes as deep as $r \sim 21$. Under these considerations, the Hydra Cluster catalogue for CHANCES was built using a combination of S-PLUS iDR4 (section 2.1) and DECam Legacy DR10 (section 2.2) data. The parent catalogue, i.e., the catalogue over which the quality cuts are to be applied, is the result of a 2 arcsecs crossmatch between these S-PLUS and Legacy data.

Next came the actual magnitude and quality cuts on this parent catalogue. For the magnitudes, we decided to use `RMAG` $<$ `20.5` for Legacy, and `r_petro` $<$ `21` for S-PLUS. These values were based on a rough estimate of what magnitude cuts would be needed to eliminate, e.g., false multiple detections of the same galaxy, which were mistaken as faint objects and other high magnitude artifacts, while still having in mind the goal of selecting objects as faint as $r \sim 21$.

Additional cuts were, for Legacy: `type` $\neq$ `"DUP"` and `brick_primary` = `True`, which, when used together, are useful to get rid of duplicates in the data, that is, objects that may be detected more than once, because of the overlap between different "bricks" observed by Legacy. Also, to select galaxies, we used `SG` = 0, which is the Legacy keyword used for SG-separation (SG = 0 for galaxies and SG = 1 for stars).

For S-PLUS data, an additional cut was applied to the `SEX_FLAGS_DET`. These are the standard SEXtractor photometric flags to control the quality of the photometry. `SEX_FLAGS_DET` comes in values of 1, 2, 4, 8, 16, 23, 64 and 128. We applied the cut of `SEX_FLAGS_DET` $<$ 4, meaning that we are allowing just objects with flags 1 (the object has neighbors, bright and

[1] https://www.4most.eu/cms/home/

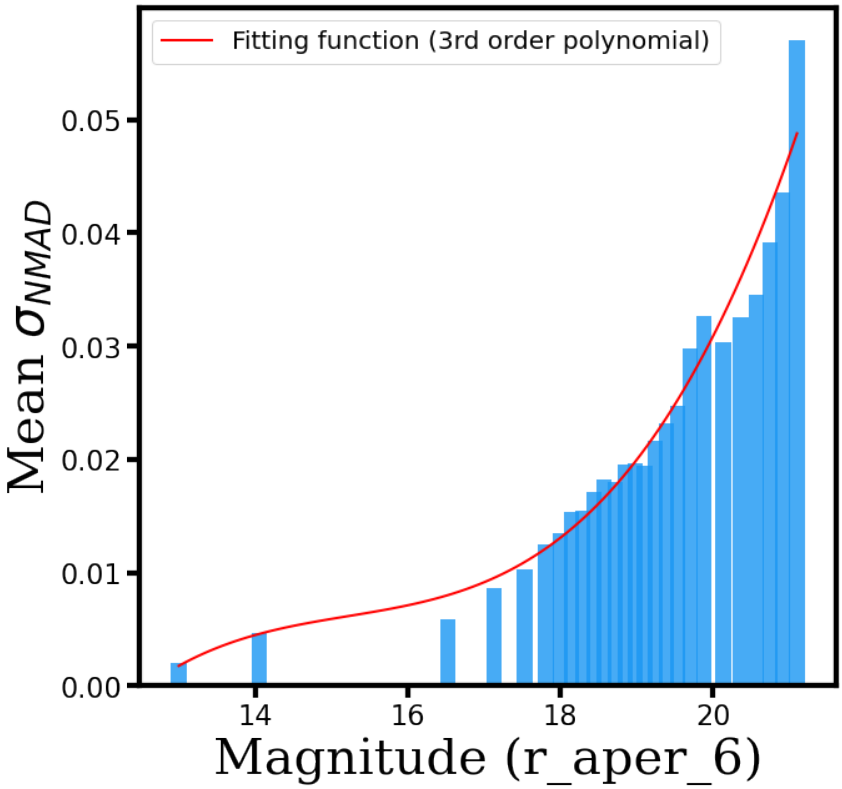

Figure 4.1: Distribution of the photo-z uncertainty, σ_{NMAD}, as a function of the r_aper_6 magnitude for a training set of objects with available z_{spec}. The red line a 3rd degree polynomial function fit to the distribution.

close enough to significantly bias the photometry or bad pixels), and 2 (the object was originally blended with another one).

The last selection procedure to apply is the photo-z cut. Usually, what we do is to apply a sharp cut at a given photo-z value for all targets. For CHANCES, however, we decided to apply a photo-z selection that took into account the variation of the photo-z estimation uncertainty. More specifically, we measure the uncertainty using $\sigma_{\rm NMAD}$, as defined by Brammer et al. (2008):

$$\sigma_{\rm NMAD} = 1.48 \times \text{median}\left(\left|\frac{\delta z - \text{median}(\delta z)}{1 + z_{\rm spec}}\right|\right) \tag{4.1}$$

where $\delta z = z_{\rm photo} - z_{\rm spec}$, $z_{\rm photo}$ is the photometric redshift, and $z_{\rm spec}$ is the true (spectroscopic) redshift of the object. Both these values of photometric and spectroscopic redshifts used to compute the $\sigma_{\rm NMAD}$ came from the training sample used to compute the photo-zs for S-PLUS.

The fainter the object, the bigger the associated $\sigma_{\rm NMAD}$ tends to be. Figure 4.1 present $\sigma_{\rm NMAD}$ as a function of the r_aper_6 magnitude. The red line in the figure is a 3rd degree polynomial fit to the $\sigma_{\rm NMAD}$ distribution. The photo-z selection procedure was done in the following way: for objects above RMAG = 16.5, we select objects whose photo-z belongs to the range $0 \leqslant z_{\rm cluster} - 2.5\sigma_{\rm NMAD,\,mag} \leqslant z_{\rm photo} \leqslant z_{\rm cluster} + 2.5\sigma_{\rm NMAD,\,mag}$, where $z_{\rm cluster}$ is the redshift of the cluster ($z_{\rm cluster} \approx 0.012$ in the case of Hydra) and $\sigma_{\rm NMAD,\,mag}$ is the value of σ_{NMAD} at a given magnitude, according to the 3rd degree polynomial function. On their turn, the objects with RMAG $\leqslant$ 16.5 where selected in the same way as before, but using a constant value of $\sigma_{\rm NMAD} = \sigma_{NMAD}(\text{RMAG} = 16.5) \approx 0.008$, i.e., the value $\sigma_{\rm NMAD}$ assumes at the value

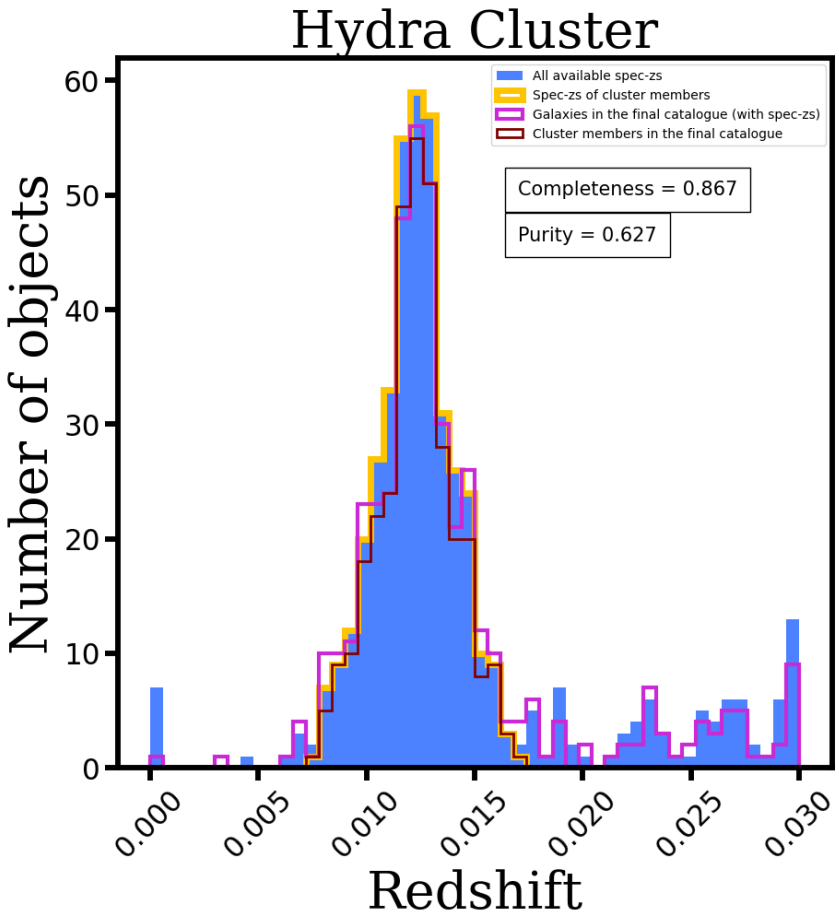

Figure 4.2: Distribution of spectroscopic redshifts of i) all galaxies available in the region of Hydra Cluster (blue), ii) cluster members defined via 3-sigma clipping (yellow), iii) galaxies in the final Hydra catalogue (purple), and iv) cluster members in the final catalogue, i.e., the intersection between the previous two.

of RMAG = 16.5. The decision to make the selection like this is because, for the brighter magnitudes, we do not have too much objects to make a reliable fit to the σ_{NMAD} distribution, so we assumed a more simple, constant value for it.

An extra step was needed at the end to add some of the brightest cluster galaxies in the catalogue. By visualizing the cluster with `Aladin`, we noticed that several bright galaxies, specially in the center of the Cluster, were lacking in our selection. After inspecting a little further, we found out that there was no S-PLUS data for those galaxies, what may be probably due to photometry issues, given that those galaxies are large, complex, and bright, making the process of extracting their photometry more prone to problems[2]. We added them by hand in the catalogue. Since there was no S-PLUS data for these galaxies, just their Legacy data was added.

The final catalogue has a total of 9.346 objects. We can describe the quality of our catalogue in terms of its completeness and purity. To estimate both of these quantities, we need some way of computing how many members galaxies the cluster "truly" has. Of course this is not feasible, otherwise there would be no point in creating a catalogue of candidate objects. But one

[2] Actually, the process of extracting the photometry of bright galaxies has a strong dependence of SExtractor parameters, so that in some cases they will be absent in photometric catalogs. For S-PLUS, Haack et al. are working to create catalogs of bright galaxies by optimizing SExtractor parameters when performing the photometry of these objects.

alternative method is to consider as "all" members galaxies of the cluster the ones we can select by applying a sigma clipping method over the spectroscopic redshifts of objects that have this quantity available. Sigma clipping is commonly used in astronomy as an outlier rejection method, in which data is assumed as a normal distribution and is rejected if outside a certain number of standard deviations from the sample's mean. In Python, sigma clipping is implemented under the `astropy.stats.sigma_clip` method, and we apply it to select cluster members as the ones with spectroscopic redshift inside 3 sigma from the sample's mean. The completeness (C) and purity (P) are then defined as

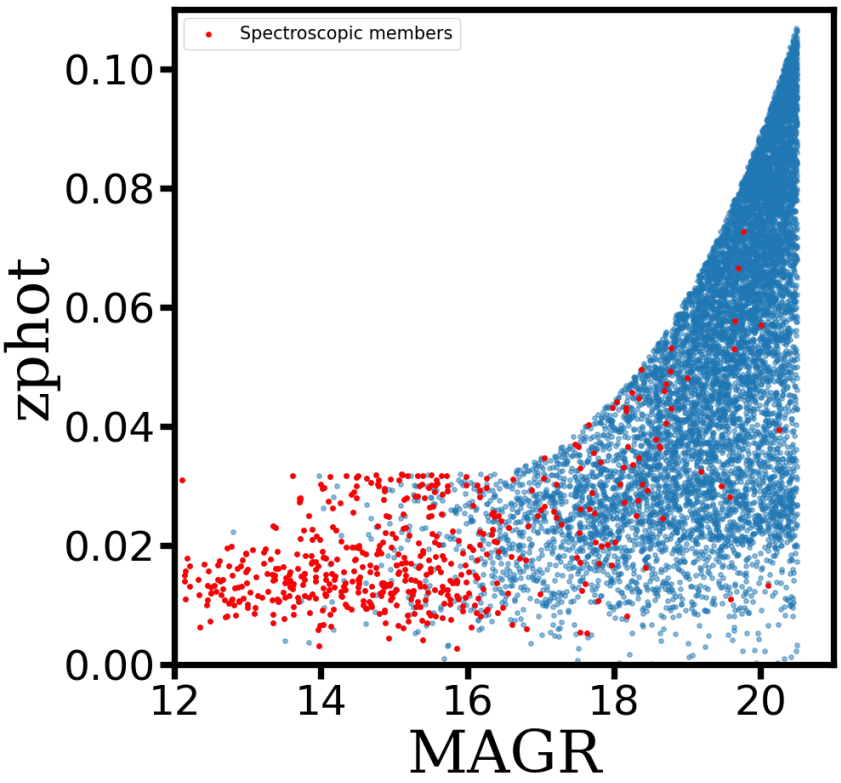

Figure 4.3: Distribution of photometric redshifts (zphot) as a function of r magnitude (MAGR) of galaxies in the final catalogue (blue), and of spectroscopic members (red).

$$C = \frac{\text{Member galaxies} \cap \text{Selected galaxies}}{\text{Member galaxies}} \tag{4.2}$$

$$P = \frac{\text{Member galaxies} \cap \text{Selected galaxies}}{\text{Selected galaxies}} \tag{4.3}$$

where member galaxies are galaxies with spectroscopic redshifts selected with 3-sigma clipping, and selected galaxies are the galaxies in our target catalogue. The resulting completeness and purity were C = 0.867 and P = 0.627, respectively. In figure 4.2 the completeness and purity of the catalogue are illustrated in the distribution of spectroscopic redshifts. In this figure, the filled, blue histogram is the distribution of all spectroscopic redshifts of galaxies in the parent catalogue, the yellow histogram represents the spectroscopic redshifts of cluster members (the denominator in the expression for completeness), the pink histogram is the distribution of galaxies with available spectroscopic redshifts in the final catalogue (the denominator in the expression for purity), and the dark red histogram is representing the cluster members in the final catalogue

(the numerator in both the expression for completeness and purity).

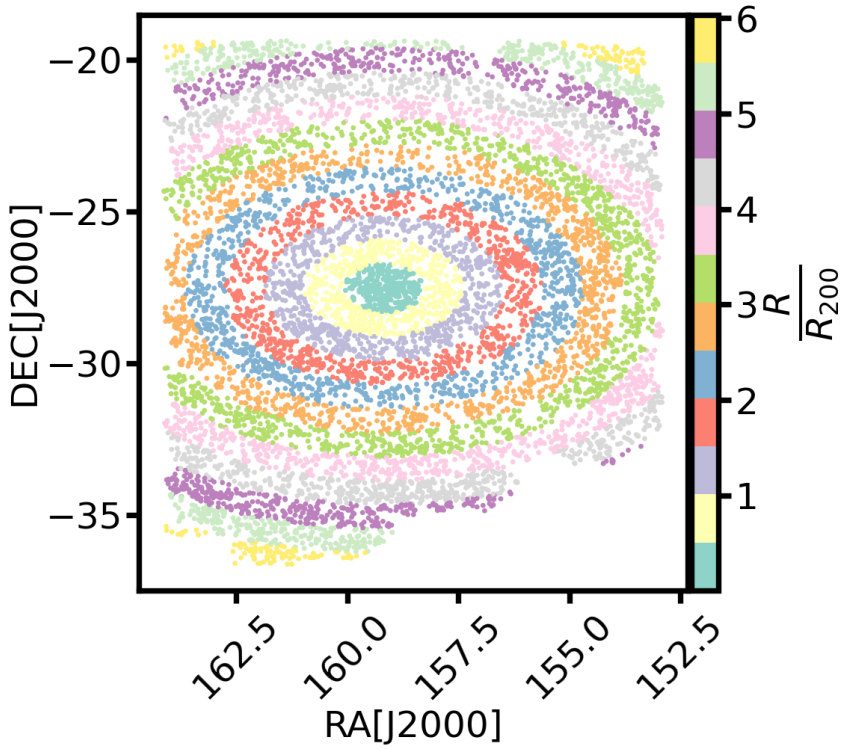

Figure 4.4: Sky distribution of galaxies in the final catalogue. The galaxies are colored by their cluster-centric distances.

It is important to emphasize that these values for completeness and purity are based on the spectroscopic information of the objects we have. In other words, it is biased for lower magnitude galaxies, which were already observed spectroscopically. So, for instance, it can be that in the higher magnitudes we are selecting more objects than actually needed, making the completeness higher and the purity lower. Or, on the contrary, it can be that we are underestimating the photo-zs of these low magnitude galaxies so that we are losing cluster members, making the completeness lower, although with a higher purity. The values of purity and completeness just mentioned are just the best guesses, given the available information. This discussion can be illustrated by figure 4.3, where we present the distribution of photometric redshifts (zphot) of galaxies in the final catalogue and of spectroscopic galaxies as a function of r magnitude (MAGR), showing that most of the spectroscopic objects have lower magnitudes.

The R.A. X Dec. distribution of galaxies in the final catalogue is presented in figure 4.4, where the galaxies are colored by their distance to the Cluster's center. The catalogue is covering almost all the region up to $3R_{200}$, and goes to $5R_{200}$ and beyond in the northern and southern regions of the Cluster, although it is lacking data in the eastern and western regions. This reflects the lack of coverage of S-PLUS and mainly Legacy Surveys in these regions, as already described in chapter 2. Further observations by both surveys are needed to fully cover the $5R_{200}$ area of Hydra Cluster.

5 Investigating the Hydra Supercluster: Methodology and Results

From the beginning, our intent was to perform a photometric investigation of all the structure of Hydra Supercluster. As already discussed in chapter 3, to study this larger area of the sky, we are going to employ a data set of objects resulting from the crossmatch of S-PLUS and Gaia data. At this point, we already have a good selection of galaxies in the region of the Supercluster, but there is still one step lacking to truly select galaxies that are part of Hydra Supercluster, such as a definition of a redshift interval for supercluster members.

In this chapter, we describe the methodology employed in the study of Hydra Supercluster and the results obtained from it, starting by the selection of members through a range of redshifts (spectroscopic and photometric) (section 5.1.1) and a search for X-ray sources in the volume of the Supercluster (section 5.1.2), followed by the method employed to construct a density map of Hydra Supercluster (section 5.2). In section 5.3 we present what may be the main point of our work: the development of a probabilistic galaxy-cluster membership method, which we employed to derive membership probabilities of galaxies in the two richest clusters of Hydra Supercluster: Hydra and Antlia. It is followed by a description of the construction of an idealized cluster mock to test the membership method (section 5.4), as well as the application of the membership method on it (section 5.5). We also test the method on a "realistic" cluster mock, and describe the results in section 5.6. The membership method is also applied on Hydra and Antlia clusters, as described in section 5.7. Finally, we describe our compilation of groups and clusters from the literature in the volume of Hydra Supercluster (section 5.8).

5.1 | Members of Hydra Supercluster

5.1.1 | Redshift distribution

To define the three-dimensional structure that comprises the Supercluster, it is essential to determine what is its extent in redshift space. This allows us to know not only what clusters and cluster galaxies are part of the Supercluster, but also to know what other galaxies, located

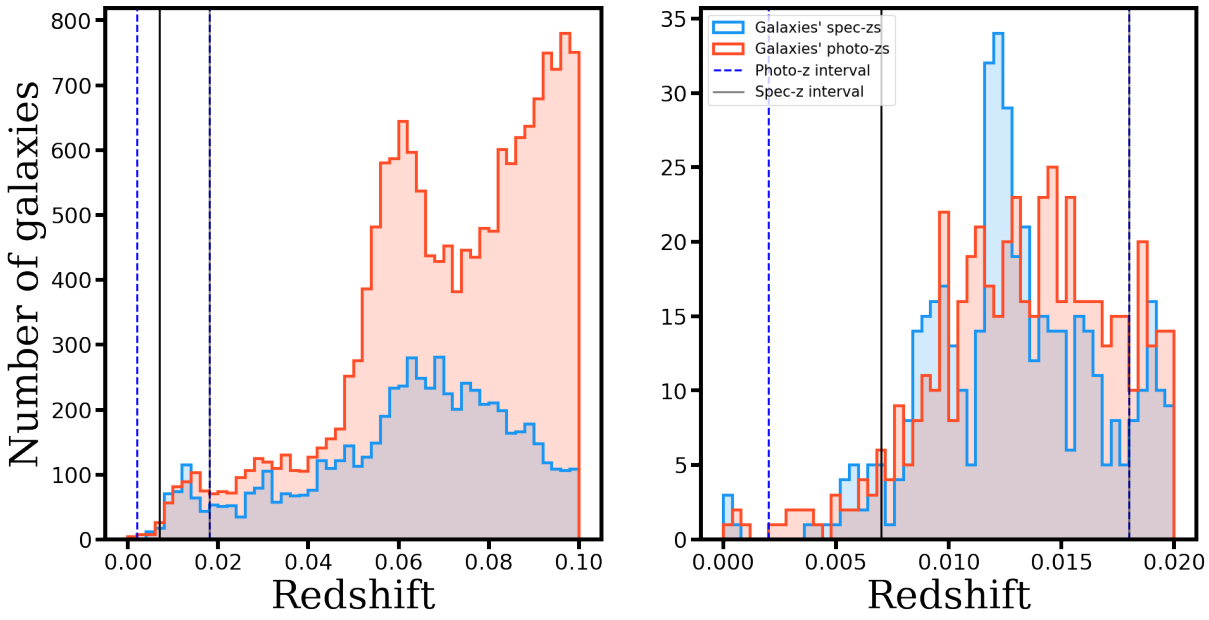

Figure 5.1: Left: distribution of spectroscopic (blue) and photometric (red) redshifts of galaxies in the area of Hydra Supercluster, in the range z=0 to z=0.1. Right: the same as left, but zooming in the interval z=0 to z=0.02. The dashed blue and solid black vertical lines indicate respectively the interval of photo-zs and spec-zs to select Supercluster members.

for instance in filaments or in the field, are part of it.

Contrary to galaxy clusters, that in general are already relaxed and have simpler geometries, superclusters are more complex structures, and cannot be assumed to have, e.g., a gaussian distribution in redshift space. Fortunately, we already have some indication of the location of Hydra Supercluster in redshift space by knowing the redshifts of its two main components: Hydra and Antlia clusters, at z=0.012 and 0.0097, respectively, but further insights can be given by looking at the redshift distribution of galaxies projected in the area of the Supercluster.

This is what we do in figure 5.1, that shows the distribution of spectroscopic and photometric redshifts of galaxies located in the area of Hydra Supercluster. In this histogram, the peak associated to Hydra Supercluster is apparent around the 0.012 redshift of Hydra Cluster. In the background of the figure in the left, we also see a very prominent peak around redshift 0.06, which is mainly associated to the Shapley Supercluster (Haines et al., 2018).

One approach we can take here is to define a range $[z_{\rm min}, z_{\rm max}]$ of redshifts to select supercluster members. This has to be done separately to spectroscopic and photometric redshifts, since the errors associated to photometric redshifts are much larger.

For the lower bound value of photometric redshifts, $z_{\rm min,phot}$, we opt to apply the value of 0.002, which is a safe margin to avoid selecting stars and low-redshift galaxies in the foreground. On its turn, the value of $z_{\rm max,phot}$ has to be such that we separate Hydra Supercluster members from background structures. Since supercluster galaxies are gravitationaly linked, they tend to agglomerate and form a peak in redshift space, as we already saw. In this way, a reasonable strategy to define an upper bound for the redshift interval is finding a drop in the number of galaxies in the distribution of redshifts, which will represent a lower density of galaxies reflecting the separation between Hydra Supercluster and background structures. We find such a drop in the distribution of photometric redshifts around the value of $z_p = 0.018$. With this, the range of

photometric redshifts we define for Hydra Supercluster is $[z_{\rm min,phot} = 0.002, z_{\rm max,phot} = 0.018]$.

A similar reasoning was applied for spectroscopic redshifts. We also find a drop at $z = 0.018$, so that we define $z_{\rm max,spec} = z_{\rm max,phot} = 0.018$. However, for the lower bound we decide to apply a higher value of $z_{\rm min,spec} = 0.007$, to ensure that we are avoiding the selection of stars and galaxies in the foreground. This value of lower bound is similar to what we find in the literature, although the upper bound that we defined is a little more generous. For instance, Radburn-Smith et al. (2006), define the interval $2000 < {\rm cz} < 4000$ km s^{-1}, roughly equivalent to $0.007 < z < 0.013$, for the the whole Hydra-Centaurus Supercluster.

5.1.2 | eROSITA X-ray sources

An important feature of clusters and groups of galaxies is that they are filled with hot, ionized plasma trapped in their potential wells that emits in X-rays. Therefore, X-rays constitute an additional tool to detect and characterize clusters and groups of galaxies. Indeed, recently we had the publication of the First Data Release of the SRG/eROSITA All Sky Survey (eRASS1). eROSITA (extended ROentgen Survey with an Imaging Telescope Array; Predehl et al., 2021) is a telescope array aboard the Spektrum Roentgen Gamma (SRG) satellite that begun its observations in December 2019 with the goal of surveying the sky producing list of X-ray detected sources with an unprecedented depth. Its main science goal is the assembly of a large sample of X-ray detected cluster of galaxies to study astrophysical processes, test theories of growth of structure, and constrain cosmological parameters. In this way, eRASS1 include a catalogue of 12,247 optically confirmed galaxy groups and clusters detected in the $0.2 - 2.3$ keV (Bulbul et al., 2024; Kluge et al., 2024). The catalogue is divided in a "primary", a "cosmology", and an "optical" catalogue. "Primary" contains basic information on the 12,247 clusters, such as cluster name, coordinates, best available cluster redshift, and X-ray properties, while "cosmology" is a subsample from "primary" with a higher purity level (95%), comprising a total of 5,259 clusters, and that will be used for cosmology studies. Both are described in Bulbul et al. (2024). On its turn, "optical" contains the same 12,247 clusters of "primary", but aggregates their optical properties using data from the DESI Legacy Imaging Surveys, such as photometric redshift, richness, optical center, and BCG position. A more in depth description of the "optical" catalogue can be found in Kluge et al. (2024).

As an increment to our list of groups and clusters in Hydra Supercluster, we searched for all X-ray sources from eRASS1 satisfying $150° <$ R.A. $< 180°$, $-48° <$ Dec. $< -15°$, $0.002 < z < 0.018$.

We found three X-ray sources classified as clusters of galaxies from eRASS1 in the volume of Hydra Supercluster. The clusters' names, R.A. and Dec. of the X-ray detections, best available cluster redshift ($z_{\rm best}$), bias-corrected cluster photometric redshift ($z_{\lambda,\rm corr}$), and richness normalized to the definition of the grz run ($\lambda_{\rm norm}$), as described in Kluge et al. (2024), are presented in table 5.1. The three sources are also illustrated in figure 5.2 in R.A. X Dec. space, with

Hydra Supercluster galaxies for reference. Two of the sources can be easily identified. `1eRASS J103007.9-351905` is at the location of Antlia Cluster, and `1eRASS J103639.8-273055` can be associated to Hydra Cluster. The third one, `1eRASS J100013.4-193806`, on its turn is associated with NGC 3091, an elliptical galaxy on the northern part of the Supercluster (de Carvalho et al., 1997).

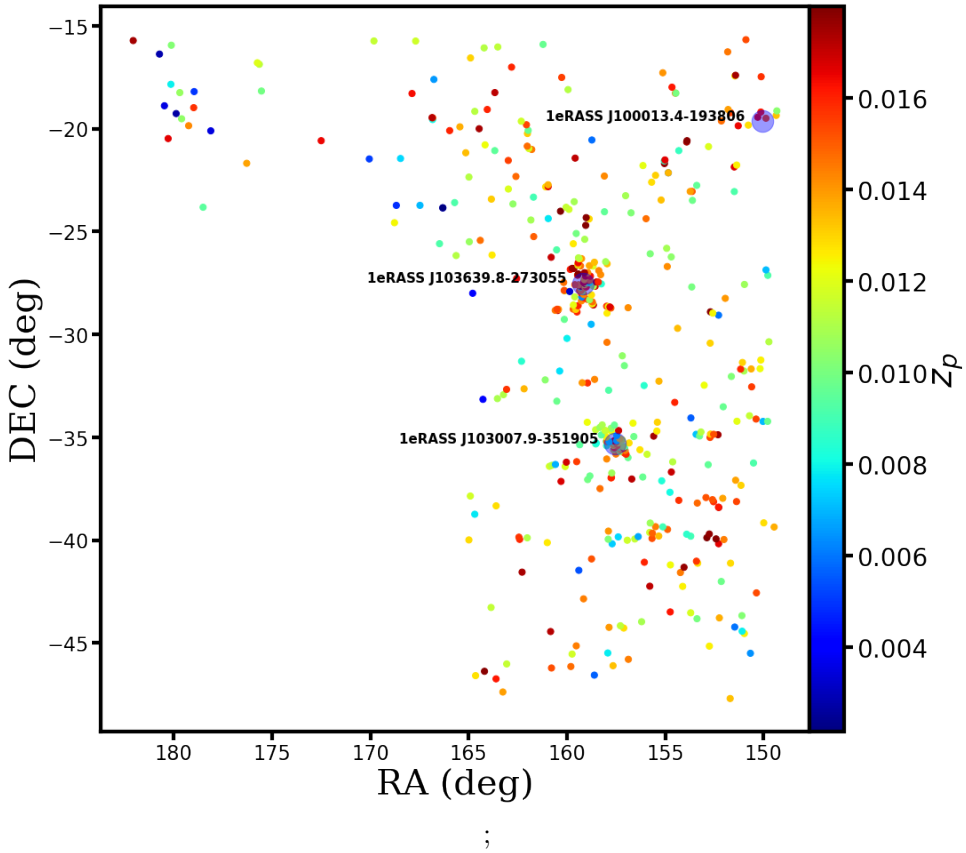

;

Figure 5.2: Spatial (R.A. x Dec.) distribution of galaxies (smaller circles) and clusters of galaxies (big circles) detected in X-ray in eRASS1. The clusters are identified by their names as in the original catalogue. Galaxies are colored according to their photo-zs.

NAME	RA_X (deg)	DEC_X (deg)	$z_{\rm best}$	$z_{\lambda,\rm corr}$	$\lambda_{\rm norm}$
1eRASS J100013.4-193806	150.0562	-19.63504	0.01217	0.41176	50.85
1eRASS J103007.9-351905	157.5332	-35.31822	0.0087		
1eRASS J103639.8-273055	159.1659	-27.51543	0.0114	0.05909	8.03

Table 5.1: X-ray sources identified as clusters of galaxies from the eRASS1 survey.

5.2 | Contrast density map

A useful approach to visualize and better understand the projected distribution of galaxies in the Supercluster is by computing the projected number density of galaxies. There are different approaches to estimate the number density, such as Kernel density estimation (KDE) and K-Nearest Neighbors (KNN). Both methods work nonparametrically, i.e., without the need of specifying a specific functional model. Such nonparametric methods are preferred over parametric ones, given that they don't require real data to follow a simple, predictable distribution, and are then able to capture every aspect of the density's distribution.

Although KDE is an interesting and commonly used method to estimate number densities, it often results in an excessive smoothing of the structures, with the underestimation of densities in crowded regions and the overestimation in sparsely populated ones, specially when a fixed value of bandwidth - i.e., the characteristic size associated to each galaxy in the density estimation - is applied. Because of this, we decided to invest in a different approach for the density estimation: the K-nearest neighbors (KNN) method. Let us introduce this technique.

5.2.1 | K-nearest neighbors density estimation

KNN is a very simple technique for estimating density in structured data, and has a good sensitivity to local density (Ivezić et al., 2020). It works by estimating the density in a given point (e.g., in a 2-dimensional grid) by taking the distance to the Kth-nearest neighbor, d_k. The density at that point will then be

$$\hat{f}_k(x) = \frac{K}{V_D(d_k)}, \tag{5.1}$$

where the volume V_D depends on the dimension D we are in: for $D = 2$, $V_2 = \pi d^2$; for $D = 3$, $V_3 = 4\pi d^3/3$, and so on. However, an even better way of estimating the density using KNN, with the resulting error being diminished without a degradation of the spatial resolution, is by considering the distances to all K nearest neighbors instead of the distance to only the Kth-nearest-neighbor:

$$\hat{f}_K(x) = \frac{C}{\sum_{i=1}^{K} d_i^D} \tag{5.2}$$

where d_i, $(i = 1, ..., K)$, are the distances to all the K-nearest neighbors. The derivation of this formula comes from bayesian analysis. It can also be shown that the proper normalization when computing local density without regard to overall mean density is

$$C = \frac{K(K+1)}{2V_D(1)} \tag{5.3}$$

where $V_D(1)$ is the volume in D dimensions of a sphere with radius 1.

We again refer to Ivezić et al. (2020) for a more in deep discussion about K-nearest neighbors density estimation and for other references as well.

We applied the `astroML.density_estimation.KNeighborsDensity` method available in Python to compute the KNN density estimation, with a small adaptation on the code to change from Minkowski to Haversine metric[1] when calculating the distances. After some tests, we decided to stick with K=10, which is a reasonable value of nearest neighbors to avoid large values of variance in the estimation.

5.2.2 | Density contrast

More than just the density map, we are interested in calculating the density contrast. The density contrast is simply defined as

$$\delta = \frac{\Sigma - \bar{\Sigma}}{\bar{\Sigma}} = \frac{\Sigma}{\bar{\Sigma}} - 1 \tag{5.4}$$

where Σ is the density at each point and $\bar{\Sigma}$ is the mean background density throughout the region. The density contrast is a useful way of comparing the density fluctuations (both under and overdensities) with the background. A density contrast value of $\delta \sim -1$ means a void, while values of $\delta >> 0$ in general trace the presence of structures.

The key point in the density contrast calculation is the determination of the background density, $\bar{\Sigma}$. We estimate $\bar{\Sigma}$ as follows: i) First, we need a way to mask the regions without data, since we do not want to bias the estimation of the background density with unrealistic low-density regions. Therefore, we start by considering as region without data all points with density lower than a certain cut value, taking care to not eliminate voids inside the supercluster region. ii) Then, we also mask the borders, considering as a point in the border all points that are within a certain distance from the points without data. This is necessary because the density in the borders is biased due to the proximity to regions without data, given the definition of KNN. iii) Finally, we define the background density as the mean of the density distribution.

With $\bar{\Sigma}$ in hands, we can apply it to equation 5.4 and obtain the density contrast map. The result is shown in figure 5.3. We also plot the three eRASS1 X-ray sources in the region of the Supercluster, and smaller groups from the literature, for reference. We notice that by the higher overdensities are associated to Hydra and Antlia clusters, as expected. We can also notice overdense regions extending to the north of Hydra and to west of Antlia, in the direction

[1] The Haversine metric is used for two-dimensional data to compute the distance between points $((x_{\rm lon}, x_{\rm lat})$ and $(y_{\rm lon}, y_{\rm lat}))$ on the surface of a sphere, and is defined as $D(x,y) = 2\arcsin\left[\sin^2(x_{\rm lat} - y_{\rm lat}/2) + \cos(x_{\rm lat})\cos(y_{\rm lat})\sin^2((x_{lon} - y_{lon})/2)\right]$

of NGC 3347 group, what can be an indication that the clusters are accreting matter from the surroundings. Other possible structures can also be seen to the south and east of Antlia, as well as to the northeast of Hydra.

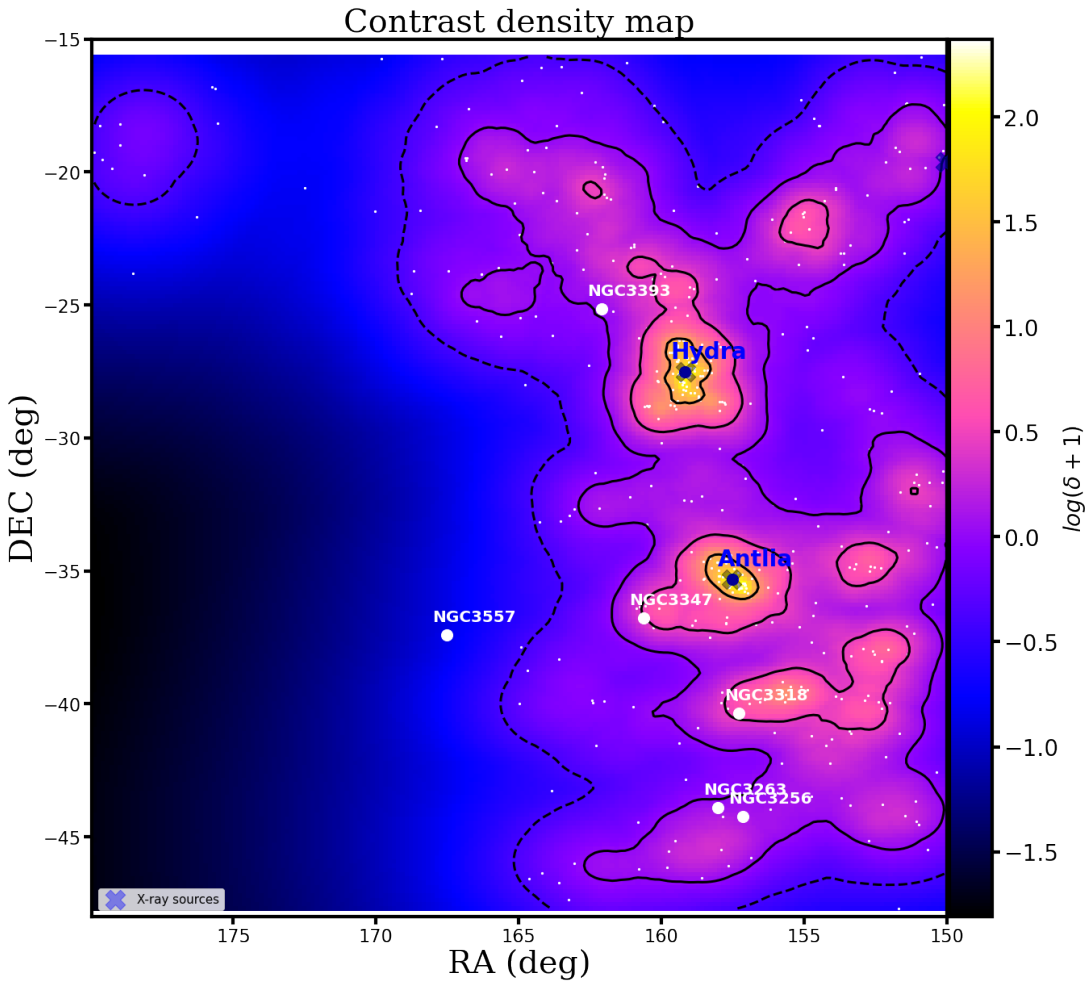

Figure 5.3: Contrast density map of Hydra Supercluster estimated with KNN method. The main groups and clusters in the Supercluster are indicated by their names. Contours indicate 50, 75, 95., 99.5 density percentiles, respectively. Groups and clister from the literature compilation are shown as black X marks, while X-ray sources are represented by blue circles.

5.3 | Probabilistic Galaxy-Cluster Membership Method

In the study of galaxies in large scale structures, such as groups and clusters, one of the fundamental steps is to reliably dictate which galaxies belong to a given structure of interest. Ideally, this could be done using the spectroscopic redshift (spec-z) of the galaxy. However, in practice, spectroscopic information is available only in a few cases, mostly for the brightest galaxies, due to the relatively high observational costs associated with this kind of observation.

Because of that, we usually opt for alternative methods using photometric data.

In chapter 4, we already discussed a way of selecting galaxies in a cluster using photo-zs, and how we applied it to perform the selection of targets in the Hydra Cluster for CHANCES. However, this method consists on the determination of memberships using only the single-point estimates of photometric redshifts, and does not take into account the more complex form of their PDFs. With that in mind, we also explored a new method to assign cluster-galaxy memberships. The method is based on the bayesian approach of George et al. (2011), and the general idea is that it use as input the whole photo-z PDF, resulting in a galaxy-cluster membership probability for each galaxy. In this section we describe in detail how the method works.

We first start by calculating the probability density function (PDF) associated with the galaxy's photo-z. We denote the photo-z PDF by $\mathcal{P}(z)$. We assume galaxies to belong either to a cluster (C) or to the field (F), and assign a Bayesian probability of a particular galaxy g belonging to the cluster.

The probability that a galaxy belongs to a cluster given $\mathcal{P}(z)$ is expressed as

$$P(g \in C|\mathcal{P}(z)) = \frac{P(\mathcal{P}(z)|g \in C)P(g \in C)}{P(\mathcal{P}(z))} \tag{5.5}$$

where the term $P(\mathcal{P}(z))$ is given by

$$\begin{aligned} P(\mathcal{P}(z)) = P(\mathcal{P}(z)|g \in C)P(g \in C) \\ +P(\mathcal{P}(z)|g \in F)P(g \in F) \end{aligned} \tag{5.6}$$

In this calculation, $\mathcal{P}(z)$ is normalized, i.e., $\int \mathcal{P}(z)dz = 1$.

We assume that the prior probability of a galaxy being a cluster member can be written as $P(g \in C) = N_C/(N_C + N_F) = 1 - P(g \in F)$, which expresses the relative number of galaxies in the cluster (N_C) or in the field (N_F).

The idea behind the calculation of the priors is that we need an *a priori* way of estimating how many galaxies are cluster members and how many are field galaxies in the cluster region.

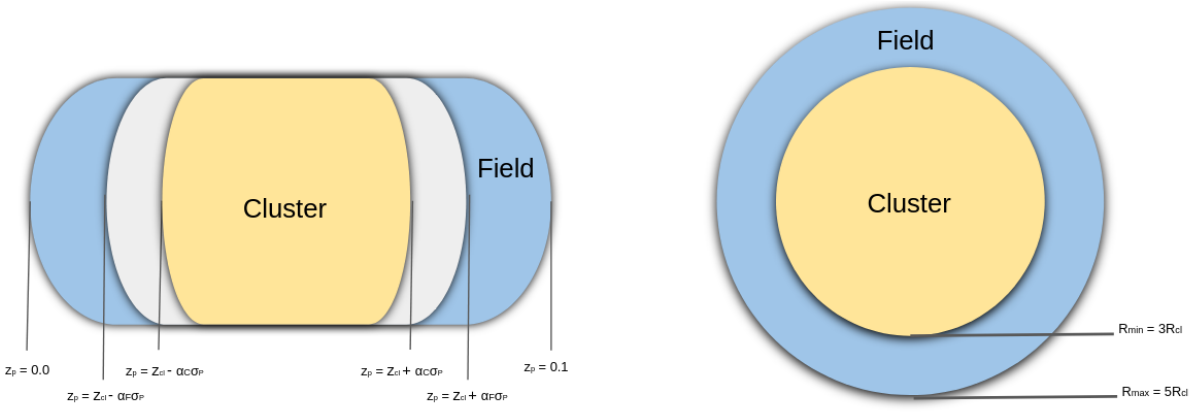

Figure 5.4: Schematic illustration of the separation between cluster and field regions utilized for the estimation of priors for the probabilistic membership method. The values of radii and photometric redshifts used to define each separation are indicated in the figure.

To do that, we define a region where we assume that all galaxies are field members and compute their number density. With the density in hands, we then estimate the number of field galaxies in the region of the cluster by multiplying it by the volume of the cluster. This idea is illustrated in figure 5.4, in which we have a cluster region and a field region, defined both in radial and photo-z space.

To do it in practice, we define as field all galaxies with clustercentric distance R_g and photo-z z_p satisfying $R_{min} < R_g < R_{max}$ and $z_C - \alpha_F \sigma_{\mathcal{P}}(m) > z_p > z_C + \alpha_F \sigma_{\mathcal{P}}(m)$, where z_C is the redshift of the cluster and $\alpha_F > 0$. Furthermore, we define $R_{\rm min} = \min\{R_g | g \in F\} = \max\{R_g | g \in C\}$ and $R_{\rm max} = \max\{R_g | g \in F\}$. This means $R_{\rm min}$ will define a radial division between field and cluster in the calculation of priors, and $R_{\rm max}$ denotes the maximum radius of the field region. We state more explicitly the values used when we describe the application of method on mocks and real clusters. Finally, $\sigma_{\mathcal{P}}(m)$ is the uncertainty in the photo-z estimations as a function of the magnitude m of the galaxy.

Once applied this selection, we define all such galaxies as being field galaxies, and compute their number density as $n_F = N_{F,o}/V_F$, where $N_{F,o}$ is the number of field galaxies as we just defined, and $V_F = \pi \left(R^2_{max} - R^2_{min}\right)(z_{max} - z_{min})$ is the volume of the field region. Here, $z_{max} = max\{z_p | g \in F\}$ and $z_{min} = min\{z_p | g \in F\}$.

With n_F in hand, we can then estimate the total number of field galaxies in the region inside R_{min} as being $N_{F,i} = n_F \times V_C$, where $V_C = \pi R^2_{min} z_{min}$ is the volume of the cluster. So, finally, computing the total number of galaxies projected in the direction of the cluster, N_{tot}, as the ones satisfying $R_g < R_{min}$ and $z_C - \alpha_C \sigma_{\mathcal{P}}(m) < z_p < z_C + \alpha_C \sigma_{\mathcal{P}}(m)$, we can obtain $P(g \in C)$ and $P(g \in F)$ as the fractions defined previously, i.e., $P(g \in C) = (N_{tot} - N_{F,i})/N_{tot} = 1 - P(g \in F)$. Notice that here we define another value of α for the cluster, i.e., α_C, which we choose to be lower than α_F to impose a fair separation in photo-z space between cluster and field.

The last terms of equation 5.5, $P(\mathcal{P}(z)|g \in C)$ and $P(\mathcal{P}(z)|g \in F)$, express the likelihoods of measuring the particular photo-z PDF $\mathcal{P}(z)$ for a known cluster or field member, respectively. Here we have to define a prior distribution of redshifts for each population. For cluster members, we define the redshift distribution as a gaussian of width $\sigma_{\mathcal{P}}(m)$, which accounts for the photo-z measurement uncertainty, and centered at the cluster redshift z_C. We denote this gaussian by $\mathcal{N}(z_C, \sigma_{\mathcal{P}})$. For the field density distribution we assume an uniform distribution and require that the integral over the redshift range $z_C \pm 3\sigma_{\mathcal{P}}$ is unity, so that the width normalization parameter is given by $w(\sigma_{\mathcal{P}}(m)) = 6\sigma_{\mathcal{P}}(m)$. We will then have:

$$P(\mathcal{P}(z)|g \in C) = \int_{-3\sigma}^{3\sigma} \mathcal{P}(z)\mathcal{N}(z_C, \sigma_{\mathcal{P}})dz \tag{5.7}$$

$$P(\mathcal{P}(z)|g \in F) = \int_{-3\sigma}^{3\sigma} \frac{\mathcal{P}(z)}{w(\sigma_{\mathcal{P}})}dz = \int_{-3\sigma}^{3\sigma} \frac{\mathcal{P}(z)}{6\sigma_{\mathcal{P}}(m)}dz \tag{5.8}$$

The uncertainty in the photo-z estimation, $\sigma_{\mathcal{P}}(m)$, is in general a function of the magnitude m of the galaxy. Here, we opt to use the σ_{NMAD}, in the same way as defined in equation 4.1.

With such simple assumptions, we can then estimate the probability $P(g \in C|\mathcal{P}(z))$ of a galaxy g being a member of a cluster C given its photo-z PDF $\mathcal{P}(z)$.

5.4 | Construction of an idealized cluster mock

Before applying the membership procedure on the real clusters, we test it on cluster mocks. Since a cluster mock is a built system, and not an observed one, we have complete control over what galaxies actually belong to the cluster or not, allowing us to test the purity and completeness of the membership method in a controlled case.

Cluster mocks aim, in general, to emulate real clusters. Here, however, we test the probabilistic membership in two types of cluster mocks. The first one, used only to test the probabilistic approach, is an idealized cluster mock, consisting of a uniform sphere of galaxies and a uniform distribution of field galaxies (section 5.5). In a second moment, we tested the method on a more "realistic" cluster mock taken from a simulated light-cone that more closely resembles the large-scale distribution of galaxies (section 5.6).

In this section we describe the construction of the simpler mock. It consists of a distribution of galaxies in three dimensions (x, y, z), in which x and y will be the coordinates of each galaxy projected on the plane of the sky, and z is the coordinate along the line of sight, which we interpret as the redshift. Additionally, each galaxy will be associated with a magnitude m. We apply a Monte Carlo simulation to assign each galaxy with a redshift, a magnitude, and the (x, y) coordinates.

The mock was built taking into consideration the geometry of a ΛCDM Universe, with $H_0 = 70$ km s^{-1} Mpc^{-1}, $\Omega_m = 0.3$ and $\Omega_\lambda = 1 - \Omega_m - 0.4165\ H_0^{-2}$.

In order to apply the Monte Carlo method, we will need expressions for the cumulative distribution of luminosities of the galaxies. For this, we consider a Luminosity Function (LF), which expresses the number of galaxies per unit volume with luminosities between L and $L + dL$. The most used in the literature, and the one we use here as well, is the Schechter LF (Schechter, 1976), which is expressed analitically as:

$$\Phi(L) = \Phi^* \left(\frac{L}{L^*}\right)^\alpha \exp\left(-\frac{L}{L^*}\right) \frac{dL}{L^*} \tag{5.9}$$

We assume the typical values of $M^* = -21$ and $\alpha = -1.25$ for the characteristic magnitude M^* (which is associated to the characteristic luminosity L^*) and the faint-end-slope respectively (e.g. Khosroshahi et al., 2006; Trentham et al., 2006).

We also know that the magnitude m is proportional to the log of the flux f of the galaxy, i.e.

$$m \propto -2.5\log f = -2.5\log\left(\frac{L}{4\pi d_L^2}\right) \tag{5.10}$$

where $d_L(z)$ is the luminosity distance, which we calculated using the cosmological calculator from Edward L. Wright[2].

If we write $L/L^* = x$, the above expression can also be written as

$$m = m_0 - 2.5\log x + 5\log d_L(z) \tag{5.11}$$

[2] https://www.astro.ucla.edu/~wright/CC.python

where m_0 is a constant of proportionality, corresponding to lowest value of the apparent magnitude at the redshift of the cluster, which we considered as $z_C = 0.01$.

At the same time, we have

$$\begin{aligned} M - M^* &= -2.5\log\left(\frac{L}{L^*}\right) \\ &= -2.5\log x \\ &\Rightarrow x = 10^{-0.4(M-M^*)} \end{aligned} \tag{5.12}$$

We will need this to calculate m_0. First, we assume that $M_{min} = -15.5$ is the absolute magnitude corresponding to the limit magnitude $m_{lim} = 20$ in a certain band at z_C, so that

$$x_{min}(z_{agl}) = 10^{-0.4(M_{min}-M^*)} \tag{5.13}$$

Finally:

$$m_0 = m_{lim} + 2.5\log x_{min} - 5\log d_L(z_{agl}) \tag{5.14}$$

Inputing all values, we get $m_0 = 6.32$.

With this, we can write the minimum luminosity observed at a redshift z as

$$x_{min}(z) = \frac{L_{min}(z)}{L^*} = 10^{-0.4(m_{lim}-m_0-5\log d_L(z))} \tag{5.15}$$

The maximum luminosity will then be $x_{max} = L_{max}/L^* = x_{min}(z_{max}) \simeq 147.6$, with a corresponding absolute magnitude of $M^* - 2.5\log x_{max} \simeq -26.4$.

Next, to obtain a sample of magnitudes for the galaxies, we have to take into consideration the distribution of redshifts. The number of galaxies per unit volume at a redshift z, $n(z)$ will be given by integrating the Schechter function (eq. 5.9) from the minimum luminosity at the redshift ($L_{min}(z)$) up to the maximum luminosity (L_{max}):

$$n(z) = \frac{dN}{dV} = \int_{L_{min}(z)}^{L_{max}} \Phi(L)dL \tag{5.16}$$

The cumulative number of galaxies up to redshift z, on its turn, is

$$N(< z) = \int_{z_{min}}^{z} n(z)dV \tag{5.17}$$

In this expression, we have to consider the effect of cosmology on the volume element dV. The comoving volume element in a solid angle Ω and a redshift interval dz is given by (Hogg, 1999):

$$dV = \frac{\Omega}{4\pi} d_H \frac{(1+z)^2 d_A(z)^2}{E(z)} dz, \tag{5.18}$$

where $d_H = c/H_0$ is the Hubble distance, $d_A = d_L/(1+z)^2$ is the angular diameter distance, and the function $E(z)$ is defined as

$$E(z) = \sqrt{\Omega_m(1+z)^3 + \Omega_K(1+z)^2 + \Omega_\lambda}, \tag{5.19}$$

Supposing the Universe has a null curvature, i.e., that it is flat (as far as we know this is actually the case), we will have

$$E(z) = \sqrt{\Omega_m(1+z)^3 + \Omega_\lambda} \tag{5.20}$$

The final expression for $N(< z)$ will then be

$$N(< z) \propto \int_{z_{min}}^{z} \frac{n(z) d_L(z)^2}{(1+z)^2 E(z)} dz. \tag{5.21}$$

And finally, the expression for the cumulative distribution of redshifts is then

$$F_z(z) = \frac{N(< z)}{N(< z_{max})} \tag{5.22}$$

Similarly, we can find a cumulative distribution of luminosities at redshift z. Notice that, for a given redshift z, we will just observe galaxies more luminous than $x_{min}(z)$. This means that the cumulative distribution of luminosities will be given by the integral of the Schechter function from the minimum luminosity expected at redshift z, $x_{lim}(z)$, up to the minimum luminosity expected at the maximum redshift, $x_{min}(z_{max})$. With that, we will be quantifying all luminosities we can observe up to the maximum redshift as a function of redshift. Finally, we normalize the distribution by dividing by the same integral, but from $x_{min}(z_{min})$ to $x_{min}(z_{max})$. The final expression will then be:

$$F_L(L|z) = \frac{\int_{x_{min}(z)}^{x_{min}(z_{max})} l^\alpha e^{-l} dl}{\int_{x_{min}(z_{min})}^{x_{min}(z_{max})} l^\alpha e^{-l} dl} \tag{5.23}$$

For our mock we used $z_{min} = 0.001$ and $z_{max} = 1.0$, although in practice the distribution of redshifts in the mock drops very quickly and we have almost no galaxy with $z > 0.2$. Notice also that we dropped the constants present in the Schechter Function, and used the substitution $L/L^* = l$.

Now we are ready to apply Monte Carlo to obtain a sample of redshifts and magnitudes for the galaxies in the mock. We assign a value of redshift for each galaxy solving the equation $F_z(z) - \gamma_z = 0$, where γ_z is a random number between 0 and 1. Indeed, from now on, every γ constant will be a number uniformly sorted from 0 to 1.

Next, given z, we solve the equation $F_L(L|z) - \gamma_L = 0$. From z and L, we calculate the magnitude m using equation 5.11.

Now we can proceed to the (x, y) coordinates of the galaxies. We divide the galaxies in two groups: field galaxies and cluster galaxies. For the field galaxies, we calculate their (x, y) positions using the radial coordinate (R) and the polar angle (ϕ). We start by sorting ϕ uniformly distributed between 0 and 2π:

$$\phi = 2\pi\gamma_\phi \tag{5.24}$$

The radial coordinate of field galaxies, on its turn, will span the interval $[0, R_{\rm field}]$, where we consider $R_{\rm field} = 10°$. Assuming the galaxies in the field are distributed uniformly, so that the density is constant, the expected number of galaxies between the projected radii R and $R + dR$ will be proportional to $2\pi RdR$, and the cumulative distribution of R will be

$$F_R = \left(\frac{r}{R_{\rm field}}\right)^2, \tag{5.25}$$

which implies that R can be sampled as

$$R = R_{\rm field}\gamma_R^{1/2} \tag{5.26}$$

Given ϕ and R, the coordinates of a field galaxy will be

$$\begin{aligned} x &= R\ \cos\phi \\ y &= R\ \sin\phi \end{aligned} \tag{5.27}$$

On their turn, the galaxies of the cluster will be sampled from an isothermal sphere centered at a redshift $z_C = 0.01$ and within a radius $R_C = R_{max} = 5°$. The density of the sphere can be expressed as:

$$n_a(r) \propto r^{-2} \tag{5.28}$$

Implying in a cumulative radial function which is proportional to r:

$$F_a = \left(\frac{r}{R_{max}}\right), \tag{5.29}$$

so that the radial coordinate can be sampled as

$$r = R_{max}\gamma_r^{1/3} \tag{5.30}$$

Similarly we can show that the polar and azimuthal coordinates can be sampled as

$$\begin{aligned} \theta &= \cos^{-1}(1 - 2\gamma_\theta) \\ \phi &= 2\pi\gamma_\phi \end{aligned} \tag{5.31}$$

Finally, the 3D coordinates of the cluster galaxies will be given by:

$$\begin{aligned} x &= r\ \sin(\theta)\ \cos(\phi) \\ y &= r\ \sin(\theta)\ \sin(\phi) \\ z &= r\ \cos(\theta) + z_C \end{aligned} \tag{5.32}$$

In figure 5.5, we show from left to right the sky distribution (x (R.A.), y (Dec.)), redshift distribution and magnitude distribution of cluster and field galaxies in the mock. Notice this is

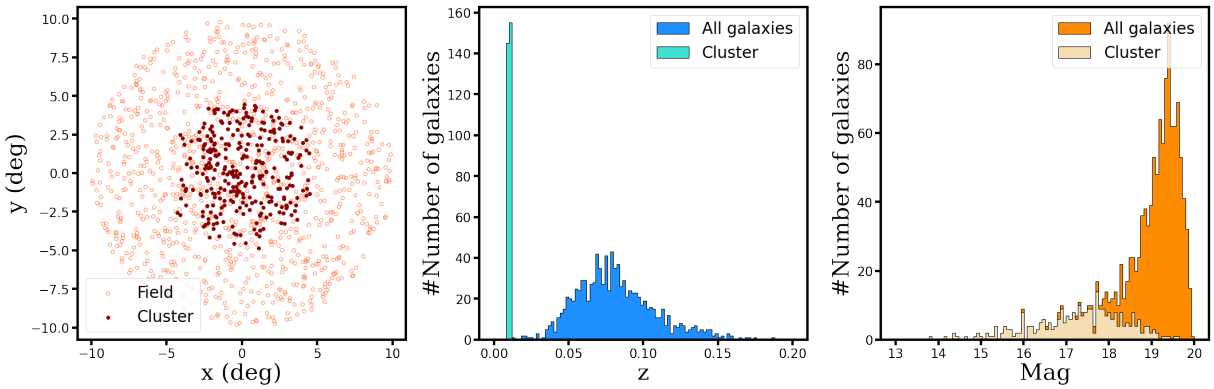

Figure 5.5: From left to right: sky distribution (x (R.A.), y (Dec.)), redshift distribution and magnitude distribution of cluster and field galaxies in our mock. In each case, the colors representing cluster and field galaxies are indicated in the legend.

a low redshift mock cluster, with its galaxies being reasonably well separated from field galaxies in redshift space. As we emphasized earlier, this is a system constructed so that we could test the membership method under ideal circumstances. In a later moment, we also test the method in a more complex cluster mock (section 5.6).

5.5 | Testing the membership method on the idealized mock

With the mock built, we are ready to test the membership method on it. The main input is the galaxy's photo-z PDF, $\mathcal{P}(z)$. For the mock, we expressed the PDFs as gaussians centered in the galaxy's simulated redshift, z, and with a width given by the typical uncertainty in the photo-z expected for the galaxy's magnitude. This uncertainty can be computed as a function of magnitude. In the same way as done in other parts of the work, here we applied $\sigma_{\rm NMAD}(m)$ uncertainty, as defined in equation 4.1.

In summary, the PDFs for the galaxy's in the mock will be expressed as

$$\mathcal{P}(x,z,m) = \frac{1}{\sigma_{\rm NMAD}(m)\sqrt{2\pi}} \exp\left(-\frac{1}{2}\frac{(x-z)^2}{\sigma_{\rm NMAD}(m)^2}\right) \tag{5.33}$$

In a very similar way, the cluster is represented in the redshift space as a gaussian:

$$\mathcal{N}(x,z_C,\sigma) = \frac{1}{\sigma\sqrt{2\pi}} \exp\left(-\frac{1}{2}\frac{(x-z_C)^2}{\sigma^2}\right) \tag{5.34}$$

where here we consider σ as the median of all $\sigma_{\rm NMAD}(m)$ of galaxies in the region of the cluster.

The priors for the mock were calculated using $R_{min} = R_C = 5^{\rm o}$, $R_{max} = R_{field} = 10^{\rm o}$, $\alpha_F = \alpha_C = 5.0$ (giving a $z_{min} = z_C + 5\sigma$), and $z_{max} = 0.2$, which is the value of redshift at

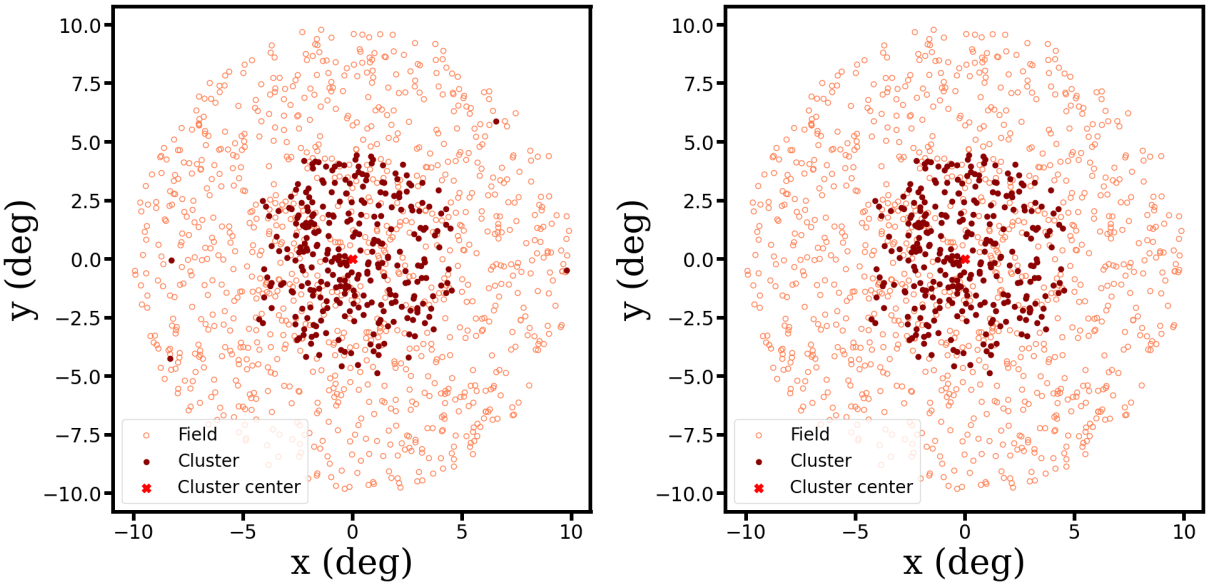

Figure 5.6: Final result of the application of the membership method over the idealized cluster mock. From left to right: i) Cluster/field separation after applying a cut of $P(g \in C|\mathcal{P}(z)) \equiv P_{mem} = 0.89$, and ii) True cluster/field separation in the mock.

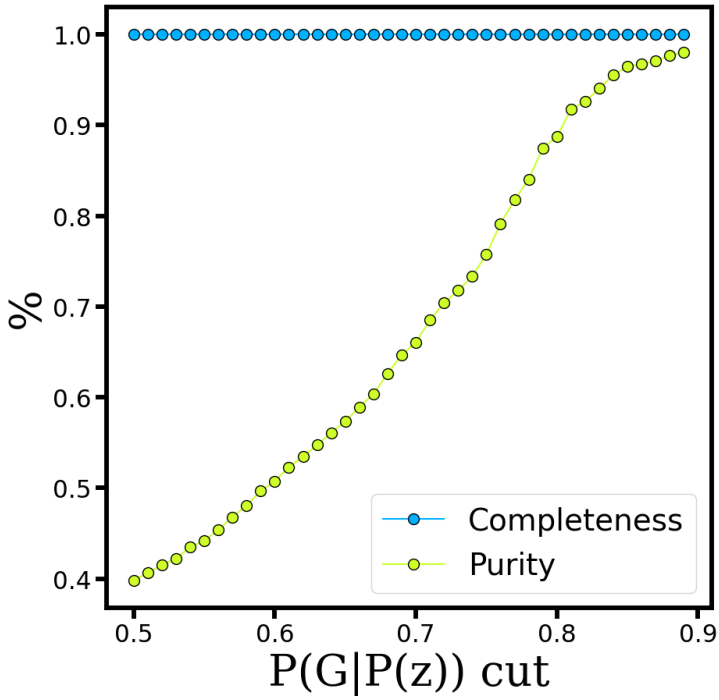

Figure 5.7: Purity (in yellow) and completeness (in blue) of the membership method as a function of $P(g \in C|\mathcal{P}(z))$ cut for galaxies in the idealized mock.

which the distribution of redshifts in the mock drops to virtually zero. The final values of the priors were $P(g \in F) = 0.23$ and $P(g \in C) = 0.77$.

The final result of the membership method applied in the mock is shown in figures 5.6 and 5.7. More specifically, figure 5.6 shows the cluster/field separation applying a cut of $P(g \in C|\mathcal{P}(z)) > 0.89$, and the true cluster/field separation of the mock. From this, we already see that the method can separate almost perfectly the cluster from the field. A more useful way of visualizing this is by computing the purity and completeness of the selection as a function of the $P(g \in C|\mathcal{P}(z))$ cut (figure 5.7). We define purity as

$$P = \frac{N_{\text{selected}} \cap N_{\text{true}}}{N_{\text{selected}}} \tag{5.35}$$

and completeness as

$$C = \frac{N_{\text{selected}} \cap N_{\text{true}}}{N_{\text{true}}} \tag{5.36}$$

where N_{selected} is the number of galaxies selected by our membership method, and N_{true} is the number of galaxies actually in the cluster.

The results in this idealized mock point that the method works satisfactorily in a simple, simulated cluster treated as a uniform sphere of galaxies, and a uniform distribution of galaxies in the field, producing a very high completeness for almost all cuts in $P(g \in C|\mathcal{P}(z))$, and a purity that increases to almost 100% with higher values of $P(g \in C|\mathcal{P}(z))$ cut.

5.6 | Testing the method on a "realistic" cluster mock

To access the performance of the membership method in a controlled case that more closely resembles the structure of a real cluster, we also run it on a "realistic" cluster mock, i.e., a galaxy cluster taken from a simulated light-cone that mimics the intricate large-scale distribution of galaxies in clusters, groups, filaments and other structures. This lightcone covers an area of 324 deg^2 and goes up to redshift z$\sim$ 0.5. The galaxy properties are modeled from a combination of the L-GALAXIES (Henriques et al., 2015) semi-analytical model (SAM) and the Millenium Simulation scaled Planck 1 cosmology (Springel et al., 2005; Angulo and White, 2010, h = 0.673, $\Omega_m = 0.315$, and $\Omega_\Lambda = 0.685$). Additional details about the mock construction can be found in (Araya-Araya et al., 2021).

Another characteristic of this mock that makes it more suitable to test the membership method is that galaxies in the mock will have an assigned S-PLUS-like photo-z.

In order to apply the membership, we need to identify a galaxy cluster in the mock. We call galaxy clusters all Millenium Simulation halo groups whose most massive subhalo has $M_{200} \geqslant 10^{14} M_\odot$. We can identify which galaxies belong to a particular mock cluster by using their `firstHaloInFOFGroupId`, which is the ID that assigns a galaxy to the most massive subhalo in a given halo. In other words, each halo will have several subhalos, but we are just interested in

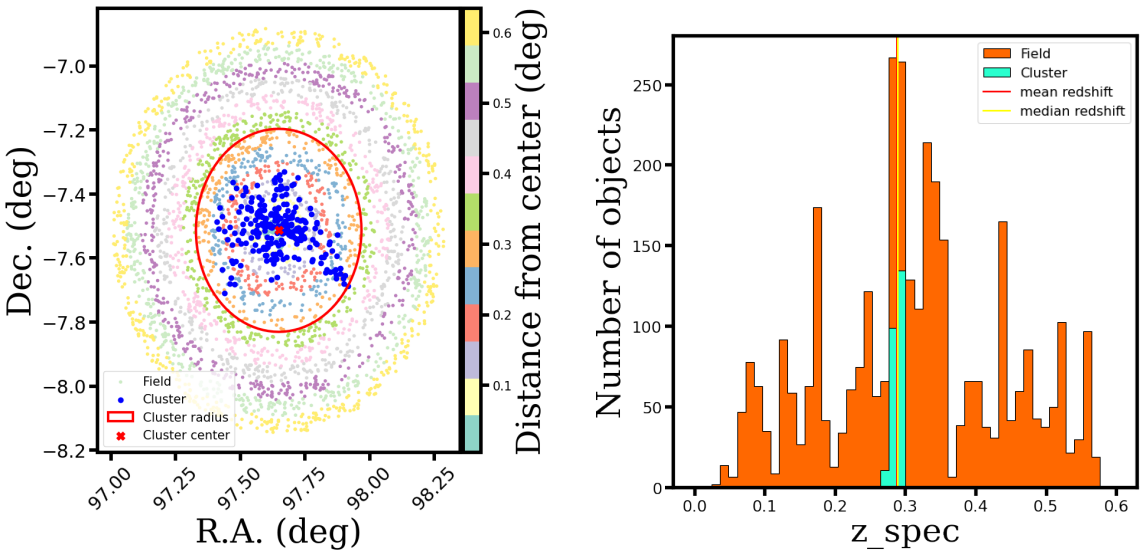

(a) *(b)*

Figure 5.8: (a) Sky distribution of galaxies in the $2R_C$ region of the mock cluster. The galaxies are colored according to their clustercentric distances. The cluster center and cluster radius are indicated in red. Blue points indicate the galaxies that actually belong to the mock cluster. (b) Distribution of redshifts of mock field and cluster galaxies in the $2R_C$ region of the mock cluster. The vertical red and yellow red lines indicate the mean and median redshift of galaxies in the cluster, respectively.

the galaxies of its most massive component.

First, we select for galaxies with available photo-z in the mock. Then we group them by their `firstHaloInFOFGroupId`, and identify which halo has the largest number of galaxies. The most populated halo, with 246 members, was chosen as the galaxy cluster on which we applied the membership procedure.

We also need to determine some parameters for this cluster: its central coordinates (α_0 and δ_0), its redshift z_C, and its radius R_C. We define α_0 and δ_0 as the mean of the right ascension and declination, respectively, of all galaxies in the cluster. Similarly, the redshift is defined as the the mean redshift of all galaxies in the cluster. An alternative definition could be the median of redshifts of galaxies in the cluster, but both values end up being very similar. Finally, the radius of the cluster is defined as the distance to the farthest galaxy from the cluster center. In figure 5.8a we show cluster galaxies and field galaxies up to $2R_C$, as well as the location of the cluster center and the cluster radius. In figure 5.8b we show the redshift distribution of cluster and field galaxies, and vertical lines representing the mean and median redshift of the galaxies in the cluster. Notice that different from the idealized mock, the cluster in this "realistic" mock does present an irregular geometry, which imposes a challenge for the membership method.

With the cluster and its center, redshift and radius defined, we are ready to apply the membership method. It proceeded very similarly as in the case of the simpler mock. The photo-z PDFs for the galaxies are again expressed as gaussian functions centered on the galaxy's photo-z and width given by $\sigma_{NMAD}(m)$ (equation 4.1), i.e., as in equation 5.33, and the cluster is represented by the same gaussian function of equation 5.34. For the prior estimation, we considered $R_{min} = R_C$, $R_{max} = 2R_C$, $\alpha_F = 5.0$ and $\alpha_C = 3.0$, and the resulting values were $P(g \in F) = 0.18$ and $P(g \in C) = 0.82$.

The result is presented in figures 5.9 and 5.10. Figure 5.9 shows a comparison between the real cluster galaxies in the mock (left) and what galaxies we get by applying a cut of $P(g \in C|\mathcal{P}(z)) > 0.87$ in the membership probability (right). Figure 5.10 presents the values of purity and completeness we obtain as a function of the $P(g \in C|\mathcal{P}(z))$ cut.

As expected, the completeness and purity obtained here are lower than the ones obtained with the idealized cluster mock. Two immediate reasons for what are the non-spherical symmetry of the cluster and the proximity in redshift space of cluster and field galaxies, as can be seen in figure 5.8. Nevertheless, we obtain reasonable values of purity (41%) and completeness (65%) with a $P_{\rm mem} = 0.85$ cut.

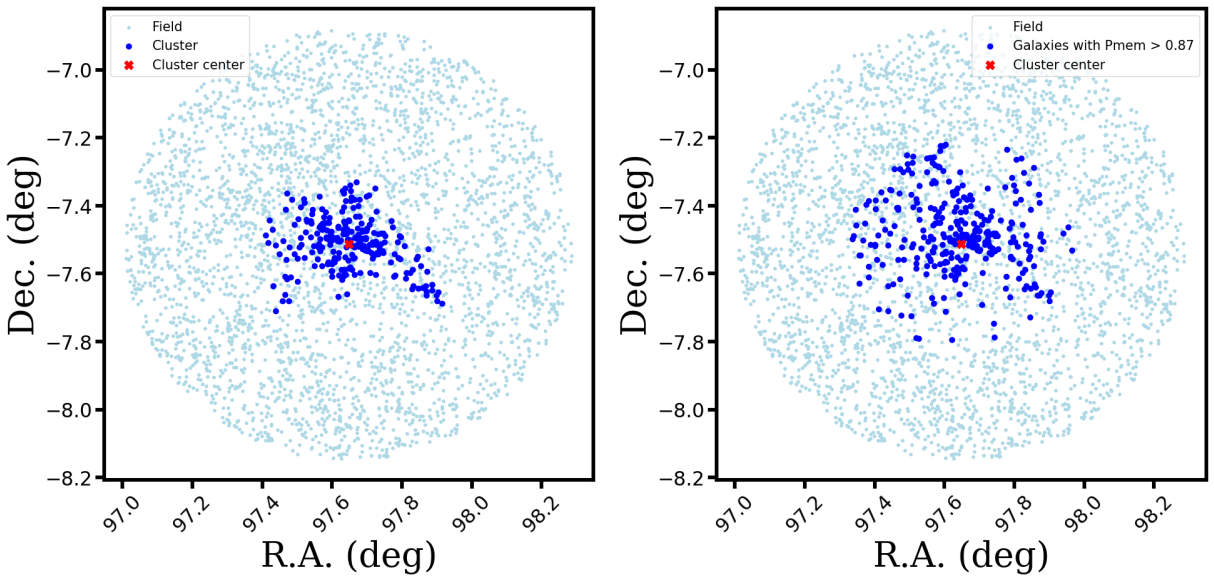

Figure 5.9: Final result of the application of the membership method over the "realistic" cluster mock. From left to right: i) Cluster/field separation after applying a cut of $P(g \in C|\mathcal{P}(z)) \equiv P_{mem} = 0.87$, and ii) True cluster/field separation in the mock.

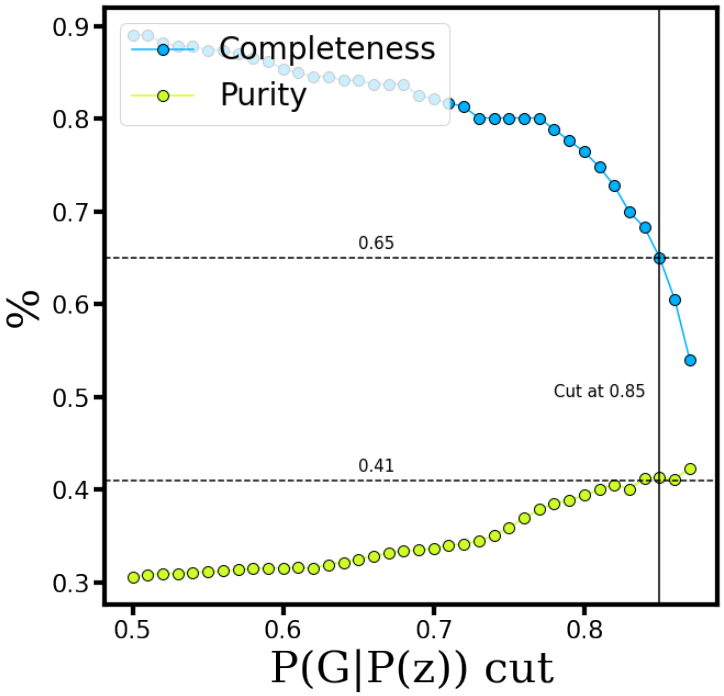

Figure 5.10: Purity (in yellow) and completeness (in blue) of the membership method as a function of $P(g \in C|\mathcal{P}(z))$ cut for galaxies in the realistic mock.

5.7 | Applying the method in real clusters

With the membership method tested on the mocks, it is time to apply it to the real clusters. In this section, we present the results for the two main clusters of Hydra Supercluster: Hydra and Antlia. In the Appendix (A.3), we also present the membership for Abell AS0639, a cluster located at redshift 0.0211 (Garilli et al., 1993), a little "behind" Hydra Supercluster, and that represents an interesting case to illustrate the application of the membership method in a higher-z cluster.

For each cluster, we first calculate the clustercentric distance of all galaxies in the Supercluster and select the ones inside $5R_{200}$ of the cluster to apply the membership procedure. We consider $R_{200} = 1.5744^{\circ}$ for Hydra (Lima-Dias et al., 2021). On its turn, for Antlia we assume $R_{200} = 1.0°$. In the same way as for the mock, we have to compute the priors for the clusters. For that, we applied $R_{\rm min} = 3R_{200}$, $R_{\rm max} = 5R_{200}$, $\alpha_F = 5.0$, and $\alpha_C = 3.0$. For Hydra the priors assumed the values $P(g \in F) = 0.73$ and $P(g \in C) = 0.27$, while for Antlia we have $P(g \in F) = 0.81$ and $P(g \in C) = 0.19$.

We access the purity and completeness of the photometrically selected members of each cluster in a very similar way as the one adopted for the target selection for CHANCES in chapter 4. In summary, we define as "true" cluster members the galaxies selected by applying a 3-sigma clipping over the spectroscopic redshifts. Then we compute completeness and purity using equations 4.2 and 4.3, respecively. In the end, we define as cluster members the galaxies with a membership probability ($P(g \in C|\mathcal{P}(z))$) higher than a certain cut value that is determined for each cluster so as to obtain reasonable values of purity and completeness simultaneously. However, other cut values can be chosen if higher values of purity or of completeness are required.

5.7.1 | Hydra

In figure 5.11 we show the sky distribution of galaxies in Hydra Cluster colored according to their clustercentric distances (left) and the distribution of spectroscopic and photometric redshifts (right). In figure 5.12a we plot a histogram showing the spectroscopic cluster members using applying the probabilistic membership method, as well as the members using 3-sigma clipping. This histogram is useful to illustrate the purity and completeness obtained for Hydra, which is shown in figure 5.12b. Chossing a cut value of $P(g \in C|\mathcal{P}(z)) = 0.35$, we obtain a completeness of 92% and a purity of 68%. Notice that if we choose for slightly lower values of $P(g \in C|\mathcal{P}(z))$ cut, the completeness will be higher, although at the expense of a much lower purity. The opposite happens if we choose a slightly higher value of $P(g \in C|\mathcal{P}(z))$ cut. We obtain a total of 256 cluster members using the 0.35 cut.

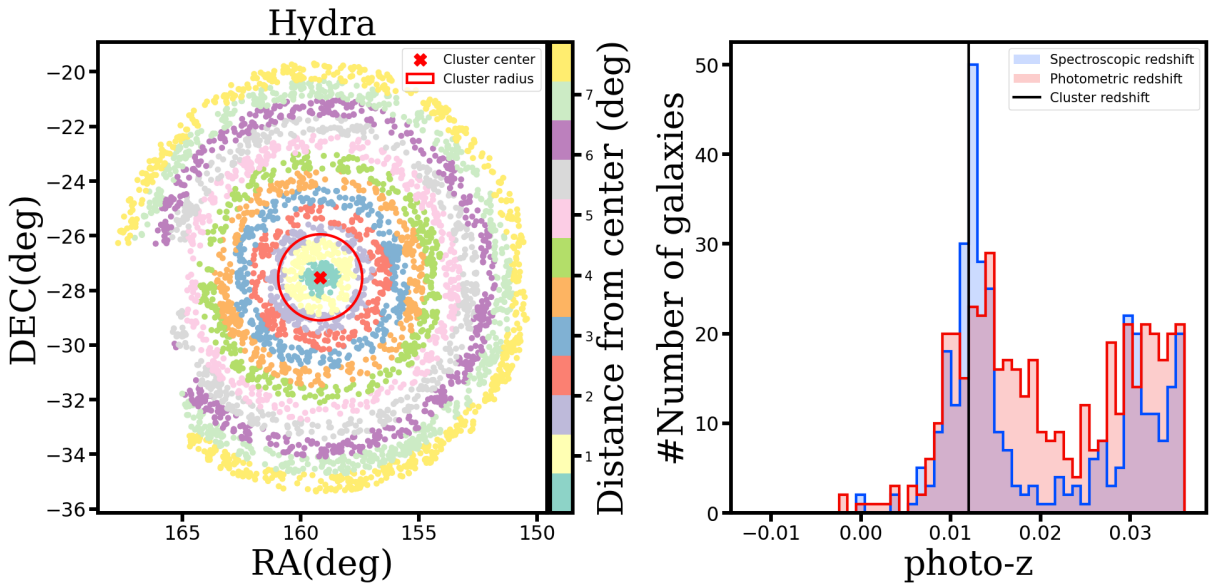

Figure 5.11: Left: sky distribution of galaxies in the $5R_{200}$ region of Hydra Cluster. The galaxies are colored according to their clustercentric distances. The cluster center and cluster radius are indicated in red. Right: spectroscopic (blue) and photometric (red) redshifts distribution of galaxies in the $5R_{200}$ region of Hydra Cluster. The vertical black line indicates the Cluster redshift.

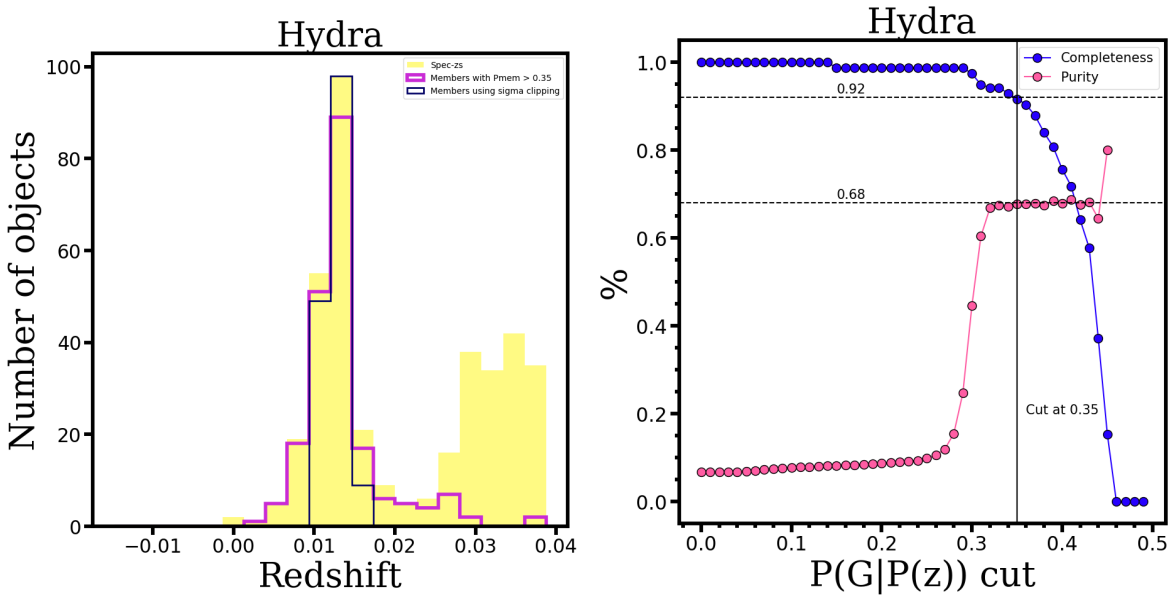

(a) *(b)*

Figure 5.12: Result of the membership method on Hydra Cluster. (a) Histograms of spectroscopic redshifts of galaxies inside $5R_{200}$ of the cluster (yellow), galaxies selected as members of the cluster using the probabilistic membership method with a cut of $P(g \in C|\mathcal{P}(z)) = 0.35$ (dark blue), and cluster members selected using 3-sigma clipping over spectroscopic redshifts (pink). (b) Purity (pink) and completeness (blue) of the membership method as a function of $P(g \in C|\mathcal{P}(z))$ cut.

5.7.2 | Antlia

In figure 5.13 we illustrate the sky distribution of galaxies in the $5R_{200}$ region of Antlia cluster, with galaxies colored according to their clustercentric distantes (left), and the distribution of spectroscopic and photometric redshifts (right). We can already notice that Antlia region is not so populated as Hydra, as expected. This also reflects on the distribution of spectroscopic and photometric redshifts, with the peak associated to Antlia Cluster not being so well pronounced as Hydra's. In the same way as for Hydra, we also show the distribituion of spectroscopic redshifts in figure 5.14a, with galaxies selected by the probabilistic membership method in pink, and galaxies selected with 3-sigma clipping in dark blue. For Antlia, we obtain completeness and purity of 81% when selecting galaxies with $P(g \in C|\mathcal{P}(z)) > 0.29$. Notice again that higher values of purity or completeness can be obtained for other probability cut values, although at the expense of a lower value of the other one.

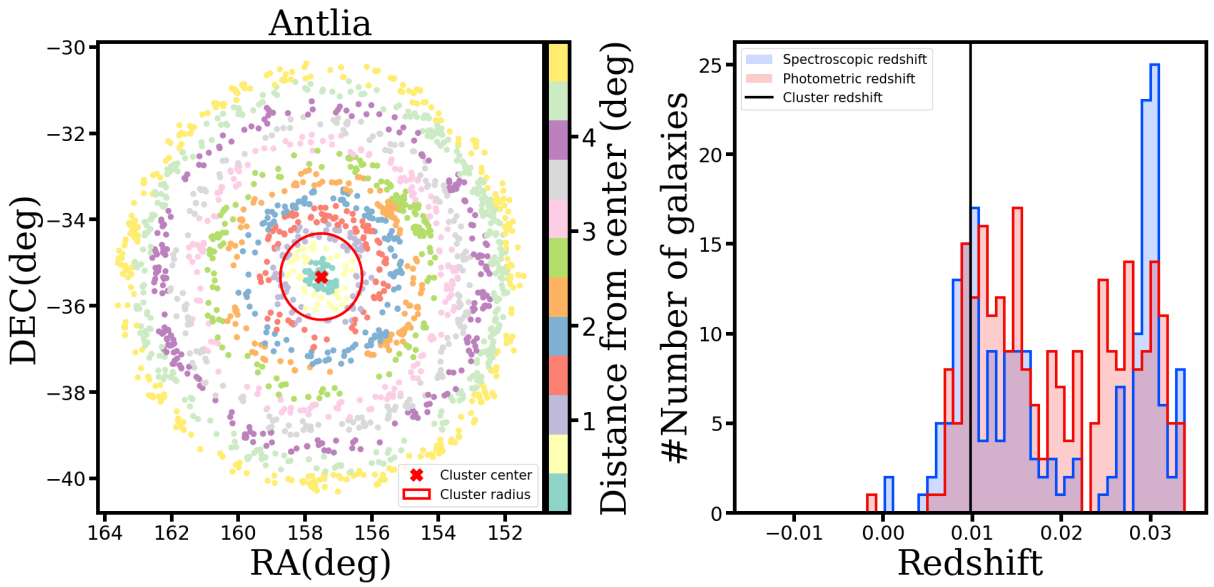

Figure 5.13: Left: sky distribution of galaxies in the $5R_{200}$ region of Antlia Cluster. The galaxies are colored according to their clustercentric distances. The cluster center and cluster radius are indicated in red. Right: spectroscopic (blue) and photometric (red) redshifts distribution of galaxies in the $5R_{200}$ region of Antlia Cluster. The vertical black line indicates the Cluster redshift.

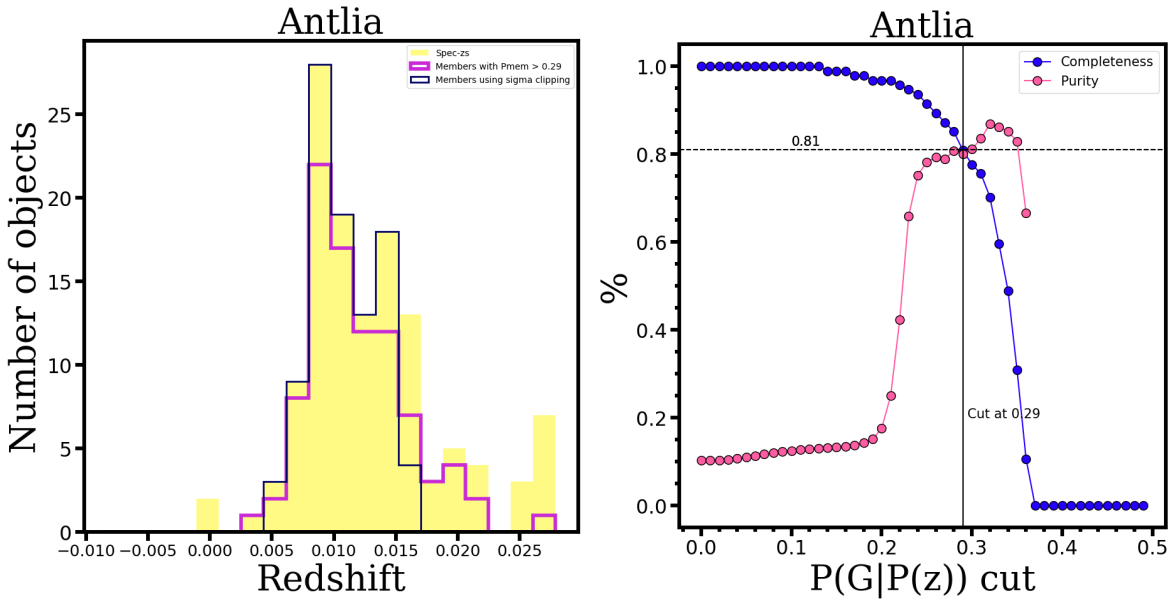

(a) *(b)*

Figure 5.14: Result of the membership method on Antlia Cluster. (a) Histograms of spectroscopic redshifts of galaxies inside $5R_{200}$ of the cluster (yellow), galaxies selected as members of the cluster using the probabilistic membership method with a cut of $P(g \in C|\mathcal{P}(z)) = 0.29$ (dark blue), and cluster members selected using 3-sigma clipping over spectroscopic redshifts (pink). (b) Purity (pink) and completeness (blue) of the membership method as a function of $P(g \in C|\mathcal{P}(z))$ cut.

5.8 | Compilation of groups and clusters

More than knowing what galaxies are members of Hydra Supercluster and its clusters, we are also interested in the groups and clusters that constitute this large structure. In the introduction we already presented a list of groups and clusters that can be found in Hydra Supercluster according to the literature. However, by performing a systematic search in the public library of published astronomical catalogues *VizieR*[3], we found hundreds of additional sources identified as groups and clusters of galaxies in the area of the Supercluster.

We built the compilation in the following way. First, we searched in *VizieR* for all catalogues of groups and clusters of galaxies than contain at least one group or cluster in a region of 30° around Hydra Cluster. We then manually filtered for the catalogues actually containing information about groups and clusters of galaxies based on their descriptions, given that some catalogues were on properties of BCG galaxies and other non-relevant information for our purposes. Then, we automated the download of the catalogues using a resource from the `astroquery` package in Python. The next step was to collect the names of the columns containing the right ascension, declination and redshifts of the groups and clusters, joining all of them in a single catalogue. Finally, to eliminate duplicates, we first applied the selection of redshifts $0.002 < z < 0.018$ and performed an internal crossmatch in the catalogue using a radius of 30 arcmin, meaning that all clusters and groups inside this radius were considered as the same. This resulted in several families of "repeated" objects, each one with a slightly different value of right ascension, declination, and redshift. To create a list of "unique" objects, we restricted the list to the right ascension, declination, and redshift of the first object in each family.

In table 5.2 we present the coordinates (R.A. and Dec.) and redshifts (z) of the final list of groups and clusters. We also illustrate it in figure 5.15, with groups and clusters being displayed in R.A. vs. Dec. (figure 5.15a) and redshift space (figure 5.15b). We have a total of 121 groups and clusters in the volume of Hydra Supercluster. In figure 5.15a, the groups and clusters are plotted as X marks. In the same figure we plot the galaxies for reference. We can see that Hydra (at R.A. = 158.97617°, Dec. = −27.61368°, and z = 0.01222) and Antlia (at R.A. = 157.51676°, Dec. = −35.30206°, and z = 0.01258) clusters are included in the list. The redshift associated with Antlia here, however, is higher than what we find in other sources, and is probably associated with some other nearby structure due to the way we built the compilation. Issues like that may be fixed in future versions of the compilation.

The distribution of redshifts of the groups and clusters in the compilation is shown in figure 5.15b. In this histogram we see some peaks at $z \approx 0.005, 0.009, 0.012,$ and 0.016. The peaks at $z \approx 0.009$ and 0.012 are probably somewhat associated to Hydra and Antlia, and may show some tendency of the groups to concentrate close to these two dominant structures of the Supercluster.

We emphasize, however, that this is still work in progress. We intend to collect other information about the groups and clusters, such as their mass and richness. In a later moment, we will also employ this list to guide a systematic study of groups and clusters in the region of

[3] https://vizier.unistra.fr/

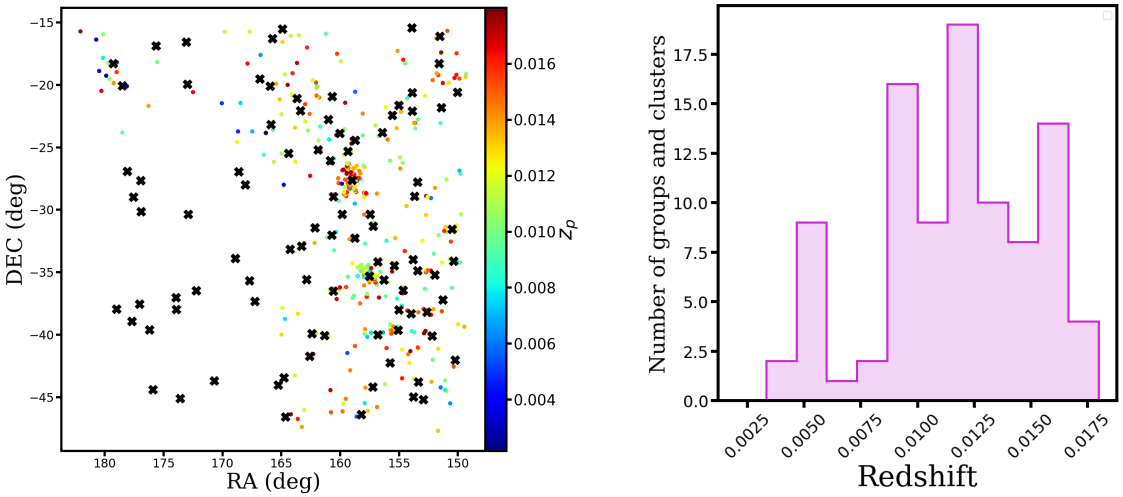

(a) *(b)*

Figure 5.15: (a) Spatial (R.A. x Dec.) distribution of galaxies (circles) and groups/clusters collected from the literature in the area of Hydra Supercluster (x marks), with colors indicating galaxies' photo-zs (z_p). (b) Distribution of redshifts of the same groups and clusters.

Hydra Supercluster, establishing their properties.

R.A. (deg)	Dec. (deg)	z	R.A. (deg)	Dec. (deg)	z
177.70476	-38.91416	0.00985	156.80719	-34.16631	0.01283
179.00167	-37.94472	0.00994	157.20063	-31.32342	0.01424
177.0413	-37.5333	0.01018	157.44645	-30.36791	0.01376
176.93156	-30.13672	0.00553	163.27392	-32.90632	0.0109
177.56326	-28.98524	0.00573	162.16285	-31.41917	0.01032
176.94443	-27.65105	0.00662	160.71819	-32.01303	0.00955
172.92343	-30.35947	0.00574	159.82327	-30.35696	0.01157
168.63658	-26.93316	0.00473	160.57035	-28.9322	0.01221
164.40676	-25.46624	0.01295	151.95252	-35.20645	0.01496
165.89569	-23.16594	0.00388	150.3539	-34.0944	0.00935
178.50444	-20.06817	0.0055	150.5004	-31.54708	0.00883
173.09416	-16.55331	0.01277	153.4221	-27.76642	0.00848
163.36865	-22.05585	0.01361	158.97617	-27.61368	0.01222
166.82753	-19.51378	0.01228	160.83326	-26.05833	0.01484
160.67594	-20.91308	0.01225	161.89202	-25.20363	0.01251
179.29555	-18.27218	0.00537	158.72472	-24.41703	0.01214
153.92158	-15.44219	0.01169	160.02812	-23.87754	0.01257
158.19861	-46.40608	0.0092	161.01545	-22.7761	0.01264
157.22101	-44.18275	0.00922	156.43233	-23.82131	0.01209
173.6013	-45.10678	0.01758	155.58797	-22.43454	0.01246
170.71614	-43.67418	0.01742	153.86976	-22.10412	0.01251
173.9283	-37.97682	0.00903	151.42159	-21.81461	0.01249
173.97153	-37.01585	0.01016	155.02688	-21.64527	0.01189
164.79262	-43.43003	0.01645	153.89486	-20.61533	0.01204
162.60848	-41.70852	0.0158	151.55747	-16.0912	0.01597
161.33802	-40.06791	0.01646	158.76172	-32.26865	0.01533
162.42051	-39.90762	0.01643	153.68895	-28.91461	0.00476
167.24028	-37.31762	0.00955	150.04941	-20.57745	0.01409
172.2262	-36.46742	0.01001	178.08578491	-26.90588951	0.0078374
167.71209	-35.66723	0.00955	168.07189941	-28.00233078	0.0054794
168.91034	-33.90102	0.00982	175.64503479	-16.86943054	0.0094676
152.94613	-45.2024	0.01355	163.66703796	-21.0665493	0.0136396
153.78162	-44.9935	0.0036	165.96238708	-20.09299088	0.013691
153.37821	-43.76758	0.01486	165.74861145	-16.28943062	0.0140912
155.10141	-39.63878	0.01539	164.90904236	-15.52632046	0.0114034
150.24734	-42.04583	0.01022	175.89698792	-44.39934158	0.0153693
152.17824	-40.08794	0.0175	176.19120789	-39.61529922	0.0105239
153.98469	-38.32588	0.01557	164.64280701	-46.58388901	0.0105222
152.66295	-38.18325	0.01547	165.28643799	-44.03953934	0.0057101
151.27829	-37.21183	0.01601	155.78164673	-42.2375412	0.0096705
156.80736	-40.00746	0.00918	155.01690674	-37.99901962	0.0159923
160.58478	-36.49503	0.01002	156.28152466	-35.60514832	0.0126246
162.86797	-35.5833	0.01553	153.42874146	-34.86256027	0.0156852
154.65028	-36.44056	0.01418	164.26760864	-33.15579987	0.0139279
155.40908	-34.48208	0.00978	159.35603333	-25.31944084	0.0135196
153.81762	-33.98734	0.00944	151.60444641	-18.27523041	0.0177698
157.51676	-35.30206	0.01258	172.9699602	-19.9509492	0.016

Table 5.2: List of clusters and groups of galaxies in the volume of Hydra Supercluster collected from the literature.

6 Conclusion

We performed a dedicated photometric study of the Hydra Supercluster of galaxies, focusing on the determination of galaxy-cluster memberships of its main components, Hydra and Antlia Clusters, and the selection of targets in Hydra Cluster to be observed by the upcoming CHANCES spectroscopic survey. Our study resulted in methods that can be applied to several cluster and supercluster systems, as well as in catalogs of galaxies and of groups and clusters of galaxies from different sources in the region of Hydra Supercluster.

For CHANCES, we created a catalogue of 9.346 candidate galaxies in Hydra Cluster using S-PLUS DR4 and DECaLS DR10 data that will be observed by the 4MOST spectroscopic facility. Via a 3-sigma clipping procedure, we estimated a completeness of 86.7% and a purity of 62.7%. The catalogue itself can already be employed in different studies that seek to investigate the galaxy population of Hydra Cluster and the properties of the Cluster itself, but more than that, it will provide a rich list of targets that will be observed spectroscopically, enabling for a variety of studies of Hydra Cluster and its member galaxies.

Going beyond, we implemented a probabilistic galaxy-cluster membership method that can be applied to several cluster systems using photometric redshifts. Leveranging the high-precision photometric redshifts already available in S-PLUS DR4, we applied the membership method to Hydra and Antlia clusters, and obtained catalogs with estimed values of 92% and 81% for completeness, and 68% and 81% for purity for Hydra and Antlia, respectively. The method was also tested in an idealized cluster mock, in which the values of purity and completeness were close to 100%, and a "realistic" cluster mock, that resulted in 65% completeness and 41% purity, showing that even under challenging circumstances the method works reasonably well.

As we are interested in the whole region of Hydra Supercluster, we also created a compilation of groups and clusters collected from the literature that can be used for future investigations of the structures present in the Supercluster. We also searched for X-rays sources in the First Data Release of SRG/eROSITA All Sky Survey (eRASS1) in the volume of Hydra Supercluster, and found counterparts in the location of Hydra and Antlia clusters, as well as a third source associated with NGC 3091, an elliptical galaxy in the northern part of the Supercluster. We also developed a contrast density map of Hydra Supercluster to better understand the spatial distribution of galaxies.

We have several ideas for the continuation of the work. They include:

- Perform the analysis of the properties of galaxies of Hydra Supercluster. Indeed, a machine learning method to derive properties of stellar populations using S-PLUS data was already developed by Cernic et al. (*in prep.*) and can be implemented for the galaxies of Hydra Supercluster selected in our work;

- Implement a method to identify the presence of filaments in the region we are studying. We

plan to make this with the SCONCE software (Zhang et al., 2022). Actually, we already tested the code with our data, and the results seem quite promising. The code is able to identify density bridges consistent with the presence of possible filaments;

– Elaborate alternative method to perform the star-galaxy separation, specially for fainter galaxies, so that we can extend our results to higher magnitudes for the whole region of Hydra Supercluster;

– Apply spectroscopic data obtained by the CHANCES survey to study Hydra Cluster galaxies when it becomes available;

– Apply the probabilistic membership method to other cluster systems. Indeed, we are already applying the method in Abell 3128 and Abell 3158. Other 64 galaxy clusters within S-PLUS footprint are also candidates for applying the method;

– Extend our studies to other supercluster systems. We have the intent of searching for a new target within the catalog of superclusters detected by eROSITA (Liu et al., 2024).

Bibliography

Abazajian, K. N. et al., "The Seventh Data Release of the Sloan Digital Sky Survey", ApJS, vol. 182, no. 2, pp. 543–558, 2009. 0812.0649, URL http://dx.doi.org/10.1088/0067-0049/182/2/543.

Abdurro'uf et al., "The Seventeenth Data Release of the Sloan Digital Sky Surveys: Complete Release of MaNGA, MaStar, and APOGEE-2 Data", ApJS, vol. 259, no. 2, 35, 2022. 2112.02026, URL http://dx.doi.org/10.3847/1538-4365/ac4414.

Abell, G. O., Corwin, J., Harold G. and Olowin, R. P., "A Catalog of Rich Clusters of Galaxies", ApJS, vol. 70, p. 1, 1989. URL http://dx.doi.org/10.1086/191333.

Angulo, R. E. and White, S. D. M., "One simulation to fit them all - changing the background parameters of a cosmological N-body simulation", MNRAS, vol. 405, no. 1, pp. 143–154, 2010. 0912.4277, URL http://dx.doi.org/10.1111/j.1365-2966.2010.16459.x.

Araya-Araya, P., Vicentin, M. C., Sodré, J., Laerte, Overzier, R. A. and Cuevas, H., "Protocluster detection in simulations of HSC-SSP and the 10-yr LSST forecast, using PCcones", MNRAS, vol. 504, no. 4, pp. 5054–5073, 2021. 2104.10161, URL http://dx.doi.org/10.1093/mnras/stab1133.

Arnaboldi, M., Ventimiglia, G., Iodice, E., Gerhard, O. and Coccato, L., "A tale of two tails and an off-centered envelope: diffuse light around the cD galaxy NGC 3311 in the Hydra I cluster", A&A, vol. 545, A37, 2012. 1205.5289, URL http://dx.doi.org/10.1051/0004-6361/201116752.

Babyk, I. V. and Vavilova, I. B., "Comparison of Optical and X-ray Mass Estimates of the Chandra Galaxy Clusters at z $<$ 0.1", *Odessa Astronomical Publications*, vol. 26, p. 175, 2013.

Bishop, C., "Mixture density networks", Workingpaper, Aston University, 1994.

Bishop, C. M., "Bayesian Neural Networks", *Journal of the Brazilian Computer Society*, vol. 4, no. 1, p. 61–68, 1997, ISSN 0104-6500. URL http://dx.doi.org/10.1590/S0104-65001997000200006.

Bond, J. R., Kofman, L. and Pogosyan, D., "How filaments of galaxies are woven into the cosmic web", Nature, vol. 380, no. 6575, pp. 603–606, 1996. astro-ph/9512141, URL http://dx.doi.org/10.1038/380603a0.

Brammer, G. B., van Dokkum, P. G. and Coppi, P., "EAZY: A Fast, Public Photometric Redshift Code", ApJ, vol. 686, no. 2, pp. 1503–1513, 2008. 0807.1533, URL http://dx.doi.org/10.1086/591786.

Bulbul, E. et al., "The SRG/eROSITA All-Sky Survey: The first catalog of galaxy clusters and groups in the Western Galactic Hemisphere", *arXiv e-prints*, arXiv:2402.08452, 2024. 2402.08452, URL http://dx.doi.org/10.48550/arXiv.2402.08452.

Calderón, J. P., Bassino, L. P., Cellone, S. A., Gómez, M. and Caso, J. P., "Early-type galaxies in the Antlia cluster: global properties", MNRAS, vol. 497, no. 2, pp. 1791–1806, 2020. 2007.05598, URL http://dx.doi.org/10.1093/mnras/staa2043.

Cantiello, M. et al., "Detection of Radial Surface Brightness Fluctuations and Color Gradients in Elliptical Galaxies with the Advanced Camera for Surveys", ApJ, vol. 634, no. 1, pp. 239–257, 2005. astro-ph/0507699, URL http://dx.doi.org/10.1086/491694.

Cautun, M., van de Weygaert, R., Jones, B. J. T. and Frenk, C. S., "Evolution of the cosmic web", MNRAS, vol. 441, no. 4, pp. 2923–2973, 2014. 1401.7866, URL http://dx.doi.org/10.1093/mnras/stu768.

Cen, R. and Ostriker, J. P., "Where Are the Baryons?", ApJ, vol. 514, no. 1, pp. 1–6, 1999. astro-ph/9806281, URL http://dx.doi.org/10.1086/306949.

Chambers, K. C. et al., "The Pan-STARRS1 Surveys", *arXiv e-prints*, arXiv:1612.05560, 2016. 1612.05560, URL http://dx.doi.org/10.48550/arXiv.1612.05560.

Cohen, S. A., Hickox, R. C., Wegner, G. A., Einasto, M. and Vennik, J., "Star Formation and Supercluster Environment of 107 nearby Galaxy Clusters", ApJ, vol. 835, no. 1, 56, 2017. 1612.04813, URL http://dx.doi.org/10.3847/1538-4357/835/1/56.

Colless, M. et al., "The 2dF Galaxy Redshift Survey: Final Data Release", *arXiv e-prints*, astro-ph/0306581, 2003. astro-ph/0306581, URL http://dx.doi.org/10.48550/arXiv.astro-ph/0306581.

Costa-Duarte, M. V., Sodré, L. and Durret, F., "Stellar populations in superclusters of galaxies", MNRAS, vol. 428, no. 1, pp. 906–911, 2013. 1210.0455, URL http://dx.doi.org/10.1093/mnras/sts088.

Crook, A. C. et al., "Erratum: "Groups of Galaxies in the Two Micron All Sky Redshift Survey" (ApJ, 655, 790 [2007])", ApJ, vol. 685, no. 2, pp. 1320–1323, 2008. URL http://dx.doi.org/10.1086/590385.

da Costa, L. N., Willmer, C., Pellegrini, P. S. and Chincarini, G., "The Centaurus-Hydra Supercluster Region. II.", AJ, vol. 93, p. 1338, 1987. URL http://dx.doi.org/10.1086/114416.

da Costa, L. N. et al., "Redshift observations in the Centaurus-hydra supercluster region. I.", AJ, vol. 91, pp. 6–12, 1986. URL http://dx.doi.org/10.1086/113974.

de Carvalho, R. R., Ribeiro, A. L. B., Capelato, H. V. and Zepf, S. E., "Redshift Survey of Galaxies around a Selected Sample of Compact Groups", ApJS, vol. 110, no. 1, pp. 1–8, 1997. URL http://dx.doi.org/10.1086/312992.

de Vaucouleurs, G. et al., *Third Reference Catalogue of Bright Galaxies* (1991).

Dey, A. et al., "Overview of the DESI Legacy Imaging Surveys", AJ, vol. 157, no. 5, 168, 2019. 1804.08657, URL http://dx.doi.org/10.3847/1538-3881/ab089d.

Dirsch, B., Richtler, T. and Bassino, L. P., "The globular cluster systems of <ASTROBJ>NGC 3258</ASTROBJ> and <ASTROBJ>NGC 3268</ASTROBJ> in the <ASTROBJ>Antlia cluster</ASTROBJ>", A&A, vol. 408, pp. 929–939, 2003. astro-ph/0307200, URL http://dx.doi.org/10.1051/0004-6361:20031027.

Dünner, R., Araya, P. A., Meza, A. and Reisenegger, A., "The limits of bound structures in the accelerating Universe", MNRAS, vol. 366, no. 3, pp. 803–811, 2006. astro-ph/0603709, URL http://dx.doi.org/10.1111/j.1365-2966.2005.09955.x.

Einasto, J. et al., "Superclusters of galaxies from the 2dF redshift survey. II. Comparison with simulations", A&A, vol. 462, no. 2, pp. 397–410, 2007a. astro-ph/0604539, URL http://dx.doi.org/10.1051/0004-6361:20065501.

Einasto, M. et al., "The richest superclusters. I. Morphology", A&A, vol. 476, no. 2, pp. 697–711, 2007b. 0706.1122, URL http://dx.doi.org/10.1051/0004-6361:20078037.

Einasto, M. et al., "SDSS DR7 superclusters. Morphology", A&A, vol. 532, A5, 2011a. 1105.2124, URL http://dx.doi.org/10.1051/0004-6361/201116564.

Einasto, M. et al., "SDSS DR7 superclusters. Principal component analysis", A&A, vol. 535, A36, 2011b. 1108.4372, URL http://dx.doi.org/10.1051/0004-6361/201117529.

Fouque, P., Gourgoulhon, E., Chamaraux, P. and Paturel, G., "Groups of galaxies within 80 Mpc. II. The catalogue of groups and group members.", A&AS, vol. 93, pp. 211–233, 1992.

Gaia Collaboration et al., "The Gaia mission", A&A, vol. 595, A1, 2016. 1609.04153, URL http://dx.doi.org/10.1051/0004-6361/201629272.

Gaia Collaboration et al., "Gaia Data Release 3: Summary of the content and survey properties", *arXiv e-prints*, arXiv:2208.00211, 2022a. 2208.00211, URL http://dx.doi.org/10.48550/arXiv.2208.00211.

Gaia Collaboration et al., "Gaia Data Release 3: The extragalactic content", *arXiv e-prints*, arXiv:2206.05681, 2022b. 2206.05681, URL http://dx.doi.org/10.48550/arXiv.2206.05681.

Garcia, A. M., "General study of group membership. II. Determination of nearby groups.", A&AS, vol. 100, pp. 47–90, 1993.

Garilli, B., Maccagni, D. and Tarenghi, M., "Galaxy velocities in eight southern clusters.", A&AS, vol. 100, pp. 33–46, 1993.

Gavazzi, G., Fumagalli, M., Cucciati, O. and Boselli, A., "A snapshot on galaxy evolution occurring in the Great Wall: the role of Nurture at z = 0", A&A, vol. 517, A73, 2010. 1003.3795, URL http://dx.doi.org/10.1051/0004-6361/201014153.

Génova-Santos, R. et al., "A Very Small Array search for the extended Sunyaev-Zel'dovich effect in the Corona Borealis supercluster", MNRAS, vol. 363, no. 1, pp. 79–92, 2005. astro-ph/0507285, URL http://dx.doi.org/10.1111/j.1365-2966.2005.09405.x.

George, M. R. et al., "Galaxies in X-Ray Groups. I. Robust Membership Assignment and the Impact of Group Environments on Quenching", ApJ, vol. 742, no. 2, 125, 2011. 1109.6040, URL http://dx.doi.org/10.1088/0004-637X/742/2/125.

Gott, I., J. Richard et al., "A Map of the Universe", ApJ, vol. 624, no. 2, pp. 463–484, 2005. astro-ph/0310571, URL http://dx.doi.org/10.1086/428890.

Guglielmo, V. et al., "The XXL Survey: XXX. Characterisation of the XLSSsC N01 supercluster and analysis of the galaxy stellar populations", A&A, vol. 620, A15, 2018. 1805.03842, URL http://dx.doi.org/10.1051/0004-6361/201732507.

Haines, C. P. et al., "Shapley Supercluster Survey: mapping the filamentary network connecting the clusters", MNRAS, vol. 481, no. 1, pp. 1055–1074, 2018. URL http://dx.doi.org/10.1093/mnras/sty2338.

Henriques, B. M. B. et al., "Galaxy formation in the Planck cosmology - I. Matching the observed evolution of star formation rates, colours and stellar masses", MNRAS, vol. 451, no. 3, pp. 2663–2680, 2015. 1410.0365, URL http://dx.doi.org/10.1093/mnras/stv705.

Hogg, D. W., "Distance measures in cosmology", *arXiv e-prints*, astro-ph/9905116, 1999. astro-ph/9905116, URL http://dx.doi.org/10.48550/arXiv.astro-ph/9905116.

Hopp, U. and Materne, J., "The Antlia cluster of galaxies and its environment : the Hydra I-Centaurus supercluster.", A&AS, vol. 61, pp. 93–106, 1985.

Hubble, E., "A Relation between Distance and Radial Velocity among Extra-Galactic Nebulae", *Proceedings of the National Academy of Science*, vol. 15, no. 3, pp. 168–173, 1929. URL http://dx.doi.org/10.1073/pnas.15.3.168.

Ivezić, Ž., Connolly, A. J., VanderPlas, J. T. and Gray, A., *Statistics, Data Mining, and Machine Learning in Astronomy. A Practical Python Guide for the Analysis of Survey Data, Updated Edition* (2020).

Kaiser, N., "Clustering in real space and in redshift space", MNRAS, vol. 227, pp. 1–21, 1987. URL http://dx.doi.org/10.1093/mnras/227.1.1.

Khosroshahi, H. G., Maughan, B. J., Ponman, T. J. and Jones, L. R., "A fossil galaxy cluster: an X-ray and optical study of RX J1416.4+2315", MNRAS, vol. 369, no. 3, pp. 1211–1220, 2006. astro-ph/0603606, URL http://dx.doi.org/10.1111/j.1365-2966.2006.10357.x.

Kluge, M. et al., "The First SRG/eROSITA All-Sky Survey: Optical Identification and Properties of Galaxy Clusters and Groups in the Western Galactic Hemisphere", *arXiv e-prints*, arXiv:2402.08453, 2024. 2402.08453, URL http://dx.doi.org/10.48550/arXiv.2402.08453.

La Marca, A. et al., "Galaxy populations in the Hydra I cluster from the VEGAS survey. II. The ultra-diffuse galaxy population", A&A, vol. 665, A105, 2022. 2206.07385, URL http://dx.doi.org/10.1051/0004-6361/202142367.

Leonard, A. and King, L. J., "A new tool to determine masses and mass profiles using gravitational flexion", MNRAS, vol. 405, no. 3, pp. 1854–1866, 2010. 0910.0842, URL http://dx.doi.org/10.1111/j.1365-2966.2010.16573.x.

Lietzen, H. et al., "Environments of galaxies in groups within the supercluster-void network", A&A, vol. 545, A104, 2012. 1207.7070, URL http://dx.doi.org/10.1051/0004-6361/201219353.

Lietzen, H. et al., "Discovery of a massive supercluster system at z ~0.47", A&A, vol. 588, L4, 2016. 1602.08498, URL http://dx.doi.org/10.1051/0004-6361/201628261.

Lima, E. V. R. et al., "Photometric redshifts for the S-PLUS Survey: Is machine learning up to the task?", *Astronomy and Computing*, vol. 38, 100510, 2022. 2110.13901, URL http://dx.doi.org/10.1016/j.ascom.2021.100510.

Lima-Dias, C. et al., "An environmental dependence of the physical and structural properties in the Hydra cluster galaxies", MNRAS, vol. 500, no. 1, pp. 1323–1339, 2021. 2010.15235, URL http://dx.doi.org/10.1093/mnras/staa3326.

Lima Neto, G. B., *Astronomia Extragaláctica e Cosmologia* (2022).

Liu, A. et al., "The SRG/eROSITA All-Sky Survey: First catalog of superclusters in the western Galactic hemisphere", *arXiv e-prints*, arXiv:2402.08454, 2024. 2402.08454, URL http://dx.doi.org/10.48550/arXiv.2402.08454.

Luparello, H. E. et al., "Effects of superstructure environment on galaxy groups", MNRAS, vol. 432, no. 2, pp. 1367–1374, 2013. 1304.0456, URL http://dx.doi.org/10.1093/mnras/stt556.

Makarov, D. and Karachentsev, I., "Galaxy groups and clouds in the local (z$\sim$ 0.01) Universe", MNRAS, vol. 412, no. 4, pp. 2498–2520, 2011. 1011.6277, URL http://dx.doi.org/10.1111/j.1365-2966.2010.18071.x.

Mendes de Oliveira, C. et al., "The Southern Photometric Local Universe Survey (S-PLUS): improved SEDs, morphologies, and redshifts with 12 optical filters", MNRAS, vol. 489, no. 1, pp. 241–267, 2019. 1907.01567, URL http://dx.doi.org/10.1093/mnras/stz1985.

Misgeld, I., Mieske, S. and Hilker, M., "The early-type dwarf galaxy population of the Hydra I cluster", A&A, vol. 486, no. 3, pp. 697–709, 2008. 0806.0621, URL http://dx.doi.org/10.1051/0004-6361:200810014.

Misgeld, I. et al., "A large population of ultra-compact dwarf galaxies in the Hydra I cluster", A&A, vol. 531, A4, 2011. 1103.5463, URL http://dx.doi.org/10.1051/0004-6361/201116728.

Mo, H., van den Bosch, F. C. and White, S., *Galaxy Formation and Evolution* (2010).

Morrissey, P. et al., "The Calibration and Data Products of GALEX", ApJS, vol. 173, no. 2, pp. 682–697, 2007. 0706.0755, URL http://dx.doi.org/10.1086/520512.

Nakazawa, K., Makishima, K., Fukazawa, Y. and Tamura, T., "ASCA Observations of a Nearby Cluster in Antlia", PASJ, vol. 52, pp. 623–630, 2000. URL http://dx.doi.org/10.1093/pasj/52.4.623.

Nakazono, L. et al., "On the discovery of stars, quasars, and galaxies in the Southern Hemisphere with S-PLUS DR2", MNRAS, vol. 507, no. 4, pp. 5847–5868, 2021. 2106.11986, URL http://dx.doi.org/10.1093/mnras/stab1835.

Nantais, J. B. et al., "Evidence for strong evolution in galaxy environmental quenching efficiency between z = 1.6 and z = 0.9", MNRAS, vol. 465, no. 1, pp. L104–L108, 2017. 1610.08058, URL http://dx.doi.org/10.1093/mnrasl/slw224.

Paine, J., Darling, J. and Truebenbach, A., "The Gaia-WISE Extragalactic Astrometric Catalog", ApJS, vol. 236, no. 2, 37, 2018. 1804.02064, URL http://dx.doi.org/10.3847/1538-4365/aabe2d.

Peacock, J. A. et al., "Studying Large-scale Structure with the 2dF Galaxy Redshift Survey", in: *A New Era in Cosmology*, edited by N. Metcalfe and T. Shanks, *Astronomical Society of the Pacific Conference Series*, vol. 283, p. 19 (2002). astro-ph/0204239.

Pedersen, K., Yoshii, Y. and Sommer-Larsen, J., "A New Measurement of the Baryonic Fraction Using the Sparse NGC 3258 Group of Galaxies", ApJ, vol. 485, no. 1, pp. L17–L20, 1997. astro-ph/9705217, URL http://dx.doi.org/10.1086/310802.

Piffaretti, R., Arnaud, M., Pratt, G. W., Pointecouteau, E. and Melin, J. B., "The MCXC: a meta-catalogue of x-ray detected clusters of galaxies", A&A, vol. 534, A109, 2011. 1007.1916, URL http://dx.doi.org/10.1051/0004-6361/201015377.

Planck Collaboration et al., "Planck 2018 results. I. Overview and the cosmological legacy of Planck", A&A, vol. 641, A1, 2020a. 1807.06205, URL http://dx.doi.org/10.1051/0004-6361/201833880.

Planck Collaboration et al., "Planck 2018 results. VI. Cosmological parameters", A&A, vol. 641, A6, 2020b. 1807.06209, URL http://dx.doi.org/10.1051/0004-6361/201833910.

Predehl, P. et al., "The eROSITA X-ray telescope on SRG", A&A, vol. 647, A1, 2021. 2010.03477, URL http://dx.doi.org/10.1051/0004-6361/202039313.

Radburn-Smith, D. J., Lucey, J. R., Woudt, P. A., Kraan-Korteweg, R. C. and Watson, U. o. D. S. R. D. D. L. A. o. P. U. o. D. S. R. D. D. L. A. o. A. U. o. C. T. R. . S. A. A. o. A. U. o. C. T. R. . S. A. A.-A. O. C. N. . A., F. G. Affiliations: AA(Department of Physics, "Structures in the Great Attractor region.", MNRAS, vol. 369, no. 3, pp. 1131–1142, 2006. astro-ph/0603692, URL http://dx.doi.org/10.1111/j.1365-2966.2006.10347.x.

Sankhyayan, S. et al., "Identification of Superclusters and Their Properties in the Sloan Digital Sky Survey Using the WHL Cluster Catalog", ApJ, vol. 958, no. 1, 62, 2023a. 2309.06251, URL http://dx.doi.org/10.3847/1538-4357/acfaeb.

Sankhyayan, S. et al., "Identification of Superclusters and Their Properties in the Sloan Digital Sky Survey Using the WHL Cluster Catalog", ApJ, vol. 958, no. 1, 62, 2023b. 2309.06251, URL http://dx.doi.org/10.3847/1538-4357/acfaeb.

Santiago-Bautista, I., Caretta, C. A., Bravo-Alfaro, H., Pointecouteau, E. and Andernach, H., "Identification of filamentary structures in the environment of superclusters of galaxies in the Local Universe", A&A, vol. 637, A31, 2020. 2002.03446, URL http://dx.doi.org/10.1051/0004-6361/201936397.

Schechter, P., "An analytic expression for the luminosity function for galaxies.", ApJ, vol. 203, pp. 297–306, 1976. URL http://dx.doi.org/10.1086/154079.

Schlegel, D. J., Finkbeiner, D. P. and Davis, M., "Maps of Dust Infrared Emission for Use in Estimation of Reddening and Cosmic Microwave Background Radiation Foregrounds", ApJ, vol. 500, no. 2, pp. 525–553, 1998. astro-ph/9710327, URL http://dx.doi.org/10.1086/305772.

Schneider, P., *Extragalactic Astronomy and Cosmology* (2006).

Shane, C. and Wirtanen, C., "", *Publications of the Lick Observatory*, vol. 22, 1967.

Shectman, S. A. et al., "The Las Campanas Redshift Survey", ApJ, vol. 470, p. 172, 1996. astro-ph/9604167, URL http://dx.doi.org/10.1086/177858.

Shull, J. M., Smith, B. D. and Danforth, C. W., "The Baryon Census in a Multiphase Intergalactic Medium: 30% of the Baryons May Still be Missing", ApJ, vol. 759, no. 1, 23, 2012. 1112.2706, URL http://dx.doi.org/10.1088/0004-637X/759/1/23.

Skrutskie, M. F. et al., "The Two Micron All Sky Survey (2MASS)", AJ, vol. 131, no. 2, pp. 1163–1183, 2006. URL http://dx.doi.org/10.1086/498708.

Smith, R. J. et al., "NOAO Fundamental Plane Survey. I. Survey Design, Redshifts, and Velocity Dispersion Data", AJ, vol. 128, no. 4, pp. 1558–1569, 2004. URL http://dx.doi.org/10.1086/423915.

Souchay, J. et al., "LQAC-5: The fifth release of the Large Quasar Astrometric Catalogue. A compilation of 592 809 objects with 398 697 Gaia counterparts", A&A, vol. 624, A145, 2019. URL http://dx.doi.org/10.1051/0004-6361/201834955.

Springel, V. et al., "Simulations of the formation, evolution and clustering of galaxies and quasars", Nature, vol. 435, no. 7042, pp. 629–636, 2005. astro-ph/0504097, URL http://dx.doi.org/10.1038/nature03597.

Tanimura, H., Aghanim, N., Douspis, M., Beelen, A. and Bonjean, V., "Detection of intercluster gas in superclusters using the thermal Sunyaev-Zel'dovich effect", A&A, vol. 625, A67, 2019. 1805.04555, URL http://dx.doi.org/10.1051/0004-6361/201833413.

The Dark Energy Survey Collaboration, "The Dark Energy Survey", *arXiv e-prints*, astro-ph/0510346, 2005. astro-ph/0510346, URL http://dx.doi.org/10.48550/arXiv.astro-ph/0510346.

The EAGLE team, "The EAGLE simulations of galaxy formation: Public release of particle data", *arXiv e-prints*, arXiv:1706.09899, 2017. 1706.09899, URL http://dx.doi.org/10.48550/arXiv.1706.09899.

Trentham, N., Tully, R. B. and Mahdavi, A., "Dwarf galaxies in the dynamically evolved NGC 1407 Group", MNRAS, vol. 369, no. 3, pp. 1375–1391, 2006. astro-ph/0603792, URL http://dx.doi.org/10.1111/j.1365-2966.2006.10378.x.

Tully, R. B., Courtois, H., Hoffman, Y. and Pomarède, D., "The Laniakea supercluster of galaxies", Nature, vol. 513, no. 7516, pp. 71–73, 2014. 1409.0880, URL http://dx.doi.org/10.1038/nature13674.

van de Weygaert, R. and Bond, J. R., "Clusters and the Theory of the Cosmic Web", in: *A Pan-Chromatic View of Clusters of Galaxies and the Large-Scale Structure*, edited by M. Plionis, O. López-Cruz and D. Hughes, vol. 740, p. 335 (2008). URL http://dx.doi.org/10.1007/978-1-4020-6941-3_10.

Vasterberg, A. R., Jorsater, S. and Lindblad, P. O., "An optical study of the cD galaxy NGC 3311 and the giant elliptical galaxy NGC 3309 in the cluster Hydra I.", A&A, vol. 247, p. 335, 1991.

Ventimiglia, G., Arnaboldi, M. and Gerhard, O., "The unmixed kinematics and origins of diffuse stellar light in the core of the Hydra I cluster (Abell 1060)", A&A, vol. 528, A24, 2011. 1101.3786, URL http://dx.doi.org/10.1051/0004-6361/201015982.

Ventimiglia, G., Gerhard, O., Arnaboldi, M. and Coccato, L., "The dynamically hot stellar halo around NGC 3311: a small cluster-dominated central galaxy", A&A, vol. 520, L9, 2010. 1009.3281, URL http://dx.doi.org/10.1051/0004-6361/201015485.

Vogelsberger, M. et al., "Introducing the Illustris Project: simulating the coevolution of dark and visible matter in the Universe", MNRAS, vol. 444, no. 2, pp. 1518–1547, 2014a. 1405.2921, URL http://dx.doi.org/10.1093/mnras/stu1536.

Vogelsberger, M. et al., "Properties of galaxies reproduced by a hydrodynamic simulation", Nature, vol. 509, no. 7499, pp. 177–182, 2014b. 1405.1418, URL http://dx.doi.org/10.1038/nature13316.

White, S. D. M., Frenk, C. S., Davis, M. and Efstathiou, G., "Clusters, Filaments, and Voids in a Universe Dominated by Cold Dark Matter", ApJ, vol. 313, p. 505, 1987. URL http://dx.doi.org/10.1086/164990.

Wong, K.-W. et al., "Suzaku X-ray Observations of the Nearest Non-Cool Core Cluster, Antlia: Dynamically Young but with Remarkably Relaxed Outskirts", ApJ, vol. 829, no. 1, 49, 2016. 1602.06950, URL http://dx.doi.org/10.3847/0004-637X/829/1/49.

York, D. G. et al., "The Sloan Digital Sky Survey: Technical Summary", AJ, vol. 120, no. 3, pp. 1579–1587, 2000. astro-ph/0006396, URL http://dx.doi.org/10.1086/301513.

Zhang, Y., de Souza, R. S. and Chen, Y.-C., "SCONCE: A cosmic web finder for spherical and conic geometries", *arXiv e-prints*, arXiv:2207.07001, 2022. 2207.07001.

A Appendix

In the Appendix, we present the queries used to download data from S-PLUS DR4 and from the Gaia DR3 extragalactic database in the region of Hydra Supercluster (sections A.1 and A.2 respectively), as well as the results of the membership method applied to the Abell S0639, in section A.3.

A.1 | S-PLUS DR4 Query

The query applied to download data from S-PLUS DR4 is presented in listing 1.

```
SELECT
det.ID, det.RA, det.DEC, sgq.PROB_GAL, sgq.CLASS, pz.odds, pz.zml,
g.g_petro, r.r_petro

FROM
idr4_dual.idr4_detection_image AS det
JOIN idr4_vacs.idr4_star_galaxy_quasar AS sgq ON (det.ID = sgq.ID)
JOIN idr4_vacs.idr4_photoz AS pz ON (det.ID = pz.ID)
JOIN idr4_dual.idr4_dual_g     AS g     ON (det.ID = g.ID)
JOIN idr4_dual.idr4_dual_r     AS r     ON (det.ID = r.ID)

WHERE
(det.Field = '{value.field}')
AND (g.g_petro < 30)
AND (r.r_petro < 30)
```

Listing 1: Query applied to download data from S-PLUS DR4 in the region of Hydra Supercluster. The download was automatized to download data for every field defined as the variable "value.field".

A.2 | Gaia Extragalactic Database Query

The query applied to download data from Gaia DR3 Extragalactic Database is presented in listing 2.

```
SELECT gc.source_id, a.ra, a.dec

FROM gaiadr3.galaxy_candidates AS gc
JOIN gaiadr3.gaia_source AS a ON (a.source_id = gc.source_id)

WHERE
a.ra > 140.0 AND a.ra < 185.0 AND
a.dec > (-50.0)AND a.dec < (-15.0)
```

Listing 2: Query applied to download data from Gaia DR3 Extragalactic Database in the region of Hydra Supercluster. The query was run on Gaia Archive (https://gea.esac.esa.int/archive/).

A.3 | Membership of Abell S0639

The probabilistic membership method can be applied to any cluster within S-PLUS footprint, not only Hydra and Antlia. To illustrate this, here we describe the galaxy-cluster membership of Abell S0639 (or simply AS0639), a cluster located a little "behind" Hydra Supercluster, at $z \sim 0.021100$ (Garilli et al., 1993).

In figure A.1 we have the sky distribution of galaxies in the $5R_{200}$ (we adopted $R_{200} = 0.5°$) region of AS0639, with galaxies colored according to their clustercentric distantes (left), and the distribution of spectroscopic and photometric redshifts (right).

AS0639 is less populated than Hydra and Antlia, and we obtained a total of 75 members by applying a cut of $P(g \in C|\mathcal{P}(z)) > 0.80$. We estimate a completeness of 88% and a purity of 63%, both comparable to the results obtained for Hydra and Antlia (see figures A.2a and A.2).

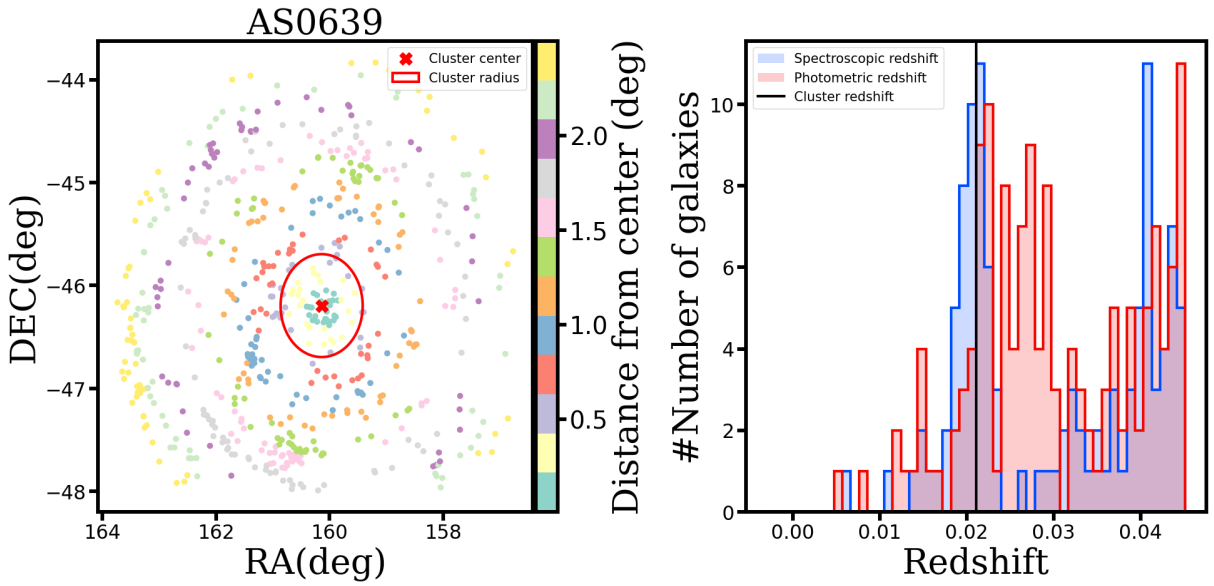

Figure A.1: Left: sky distribution of galaxies in the $5R_{200}$ region of Abell S0639 Cluster. The galaxies are colored according to their clustercentric distances. The cluster center and cluster radius are indicated in red. Right: spectroscopic (blue) and photometric (red) redshifts distribution of galaxies in the $5R_{200}$ region of Abell S0639 Cluster. The vertical black line indicates the Cluster redshift.

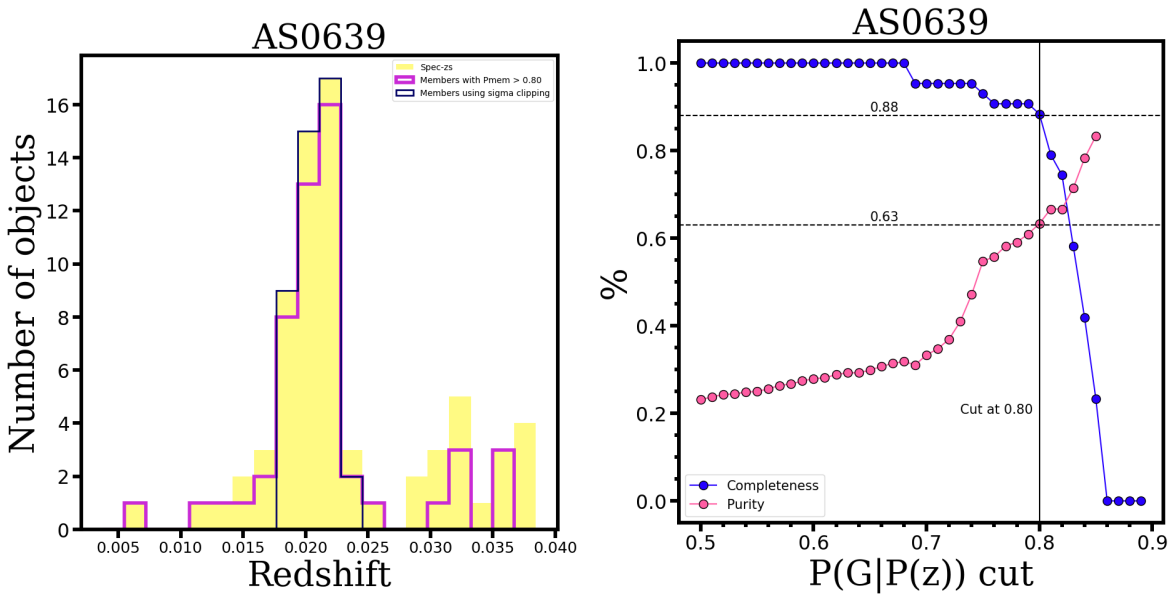

(a) *(b)*

Figure A.2: Result of the membership method on Abell S0639 Cluster. (a) Histograms of spectroscopic redshifts of galaxies inside $5R_{200}$ of the cluster (yellow), galaxies selected as members of the cluster using the probabilistic membership method with a cut of $P(g \in C|\mathcal{P}(z)) = 0.80$ (dark blue), and cluster members selected using 3-sigma clipping over spectroscopic redshifts (pink). (b) Purity (pink) and completeness (blue) of the membership method as a function of $P(g \in C|\mathcal{P}(z))$ cut.